# Spin accumulation and transport studied in double magnetic tunnel junctions


Rowan Caradoc Temple

School of Physics and Astronomy

University of Leeds

Submitted in accordance with the requirements for the degree of

*Doctor of Philosophy*

December 2014

## Intellectual Property Statement

The candidate confirms that the work submitted is his/her own, except where work which has formed part of jointly authored publications has been included. The contribution of the candidate and the other authors to this work has been explicitly indicated below. The candidate confirms that appropriate credit has been given within the thesis where reference has been made to the work of others.



Work from the following jointly authored publication is presented in chapter five of this thesis:
R. C. Temple and C. H. Marrows. Single-electron spin interplay for characterization of magnetic double tunnel junctions. *Phys. Rev. B* **88**, 184415 (2013). **Work attributable to candidate:** Theory development, calculations and preparation of manuscript. **Work attributable to others:** Professor Chris Marrows discussed results and edited the manuscript.

# Acknowledgements

Firstly I am very grateful to my advisor Prof. Chris Marrows. Throughout my PhD he has been supportive, organised and encouraging, and has shown great patience allowing me to follow ideas through. I also thank the other academics in the group, Prof. Bryan Hickey, Dr. Oscar Céspedes, Dr. Gavin Burnell and Dr. Thomas Moore for their assistance, ideas and many critical insights. Thank you to Prof. Steve Evans for the use of the STM.

There are a huge number of people who have given me invaluable help and time in the labs, thanks to all and especially Dr. Mannan Ali, Dr. Andrei Mihai, Mr. Laurynas Pukenas, Dr. Mike Ward and Dr. Kari Dempsey. Thanks go also to all of the technical staff in the electronics and mechanical workshop, they have been always ready and willing to assist. I am very grateful to John Turton for his help and expertise and to the late Philip Cale for continuously filling helium for me at the last minute.

The Condensed Matter group has been a pleasure to work with. Thanks to everyone for the good times, whether in the pub, on top of Snowdon, or doing the lunchtime crossword. I am grateful to Dr. May Wheeler for her friendship and for organising important 4 o'clock meetings, to my long standing office mates Dong and Priya for putting up with me and to my squash buddies Soph, Joe, Aleš and Nick for keeping me fit and pushing me to the max.

To my wonderful family for their support and encouragement, particularly to my father who started my science and philosophy education from a young age. Finally, to Mrs. Victoria Temple (ray!), for her constant patience and kindness, especially when I lacked arms.

# Abstract

Magnetic CoFe nanoparticles have been produced by gas-aggregation and incorporated into sputtered MgO tunnel junction structures. Scanning tunnelling microscopy (STM) has been developed as a technique for examining spin accumulation and transport in these nanoscale junctions.

The particles were initially characterised for their magnetic properties; x-ray magnetic circular dichroism on 11-14 nm diameter clusters was performed. The orbital-to-spin moment ratio was found to be enhanced over the bulk value and to decrease with increasing average diameter, which complements previous studies on smaller particles. The size dependence of the combined data is found not to follow predicted trends based on reduced orbital moment quenching in the outer shell. In particular for these large particles, the quenching is far more rapid than expected. Magnetometry studies on random arrays of nanoparticles at percolation show interesting effects attributed to complex magnetic dipolar interactions. This includes very broad range anisotropy and large blocking temperatures.

For transport measurements, cryogenic STM is used to address individual islands and forms the top electrode of a double magnetic tunnel junction. Single electron charging effects are observed in these confined structures and the charging energy correlates to the size of the particle. New theory was developed to simulate these structures, giving an analytical solution to the current numerical orthodox theory. These solutions showed that TMR measurements, a current major barrier to studying nanospintronics using STM, were unnecessary. We are able characterise the tunnel junction parameters, including spin polarisation and accumulation, in a single I-V sweep of high information density. The spin polarisations of the opposing electrodes are found to be aligned anti-parallel despite a parallel magnetisation axis. Finally the spin lifetime on the island was calculated and found to exceed 1 μs, longer than measured in previous studies.

# Contents

# Abbreviations

| | |
|---|---|
| AC | Alternating current |
| AFM | Atomic force microscopy |
| BCC | Body centered cubic |
| CIP | Current in-plane |
| CM | Condesed matter |
| CPP | Current perpendicular-to-plane |
| DC | Direct current |
| DFT | Density functional theory |
| DMTJ | Double magnetic tunnel junction |
| DOS | Density of states |
| EBL | e-beam lithography |
| FC | Field cooled |
| FCC | Face centered cubic |
| FM | Ferromagnet |
| FW | Field warmed |
| GMR | Giant magnetoresistance |
| HOPG | Highly oriented pyrolytic graphite |
| HV | High vacuum |
| IP | In-plane |
| MC | Magneto-crystalline |
| MOKE | Magneto optical Kerr effect |
| MRAM | Magnetic random access memory |
| MTJ | Magnetic tunnel junction |
| NM | Normal metal |
| NP | Nanoparticle |
| OOP | Out-of-plane |
| PID | Porportional, integral, differential |
| RF | Radio frequency |
| SP | Super paramagnetic |
| SPM | Scanning probe microscopy |
| STM | Scanning tunnelling microscopy |
| STS | Scanning tunnelling spectroscopy |
| TEM | Transmission electron microscopy |
| TMR | Tunnelling magnetoresistance |
| UHV | Ultra high vacuum |
| VSM | Vibrating sample magnetometry |
| VT | Variable temperature |
| WKB | Wentzel-Kramers-Brillouin |
| XAS | X-ray absorption spectroscopy |
| XMCD | X-ray magnetic circular dichroism |
| XRR | X-ray reflectivity |
| ZFC | Zero field cooled |

# Chapter 1

Introduction

Employing nearly a quarter of the international physics community [1; 2], condensed matter research is a vibrant and active discipline, investigating the complex and often unpredictable properties of solid state materials. Much of this research takes place at the borderline between industrial applications and novel physics; a prime example of this is the field of spintronics. The work in this thesis is concerned with spintronics - the manipulation of the spin and charge of electrons - but is attempting to bring it down to a technologically relevant nanoscale. At this level very small quantities of spin accumulation must be considered and transport is constricted to the flow of a single electron at a time.

The work revolves around magnetic nanoparticles (NPs) in the 4-14 nm diameter range. This size range is too large for the particles to be considered quantum dots at the temperatures used in this study. They are, however, at the cross-over point between classical and quantum dominated physics. This produces effects that are surprisingly different from either regime. While there has been a lot of effort to understand transport through these devices theoretically [3–5], experimentally they have been difficult to work with due to problems with accessing the nanoscales needed for measurements [6; 7]. Very few methods exist to study individual nanoparticles and there are still many questions to be answered. One of the major efforts of this work was to conduct transport studies through particles individually addressed by scanning tunnelling microscopy (STM). STM turns out to have a lot of advantages for this type of study but faces significant difficulty with certain relevant measurements, particularly tunnel magnetoresistance (TMR). Theoretical advances that are presented here go some way towards mitigating this problem.

This work is in an active area of research which is collectively often referred to as nanospintronics. It is born out of work in single electron transistors (SETs) combined with classic spintronics. To give some context to the project I will now give some history of these two disciplines and the beginnings of nanospintronics. I will end the introduction with a more specific guide to the work presented in this thesis.

## 1.1 Spintronics

Spintronics began with the introduction in 1988 of the giant magnetoresistive (GMR) effect [8; 9]. It has since generated a huge area of active research. Albert Fert and Peter Grünberg were awarded the 2007 Nobel prize in physics for their part in the discovery.

As opposed to the charge manipulation of conventional electronics, spintronic devices attempt to manipulate both the charge and the spin degrees of freedom. Spintronic devices are now heavily employed in the data storage and magnetic sensing industry [10].

The GMR effect was first observed in high quality thin film multilayer stacks composed of alternating ferromagnetic (FM) and non-magnetic (NM) layers [9]. The FM layers act like a valve: when the FM moments are aligned the electrical resistance of the film is low, when they are anti-parallel the resistance is high. This extra resistance is caused by spin dependent scattering effects at the interfaces [11] (and references therein). By controlling the relevant layer alignment through an externally applied field, this can act as a sensor, converting external magnetic field into an electronic switch. For 10 years this was the standard technology used in hard drive read heads to detect memory bit states. By the end of the cycle, GMR had allowed an increase in areal data density of 1000 fold over previous inductive technologies [10].

More recent applications have been geared towards trying to realise magnetic random access memory (MRAM), permanent state random access memory based on spin devices such as spin valves or magnetic tunnel junctions [12]. MRAM is now commercially available though not yet widely adopted [13]. New fascinating physics is constantly emerging from spintronic systems, with modern studies looking at spin transfer torque [14; 15], spin Hall effect [16–18], spin orbit torques [19–22], spin caloritronics [23] and topological materials [24–27] to name a few [28; 29].

### 1.1.1 The magnetic tunnel junction

In the end the success of the GMR device was limited by the small signal ratio between its on and off state (otherwise known as its magnetoresistance (MR) ratio). The device that replaced GMR in commercial hard drives in 2005 is the magnetic tunnel junction (MTJ) [10]. This is a sandwich stack similar to the GMR device in structure, however the non-magnetic spacer layer of the GMR is replaced by an insulating tunnel barrier. By directing the current perpendicular to the plane of the film through the tunnel barrier, MR ratios upwards of 600% have been achieved.

Julliére reported the first MTJ structure in 1975 [30], though this work went relatively unnoticed for some years after its initial publication. The MTJ was an Fe/Ge-oxide/Co stack which showed a tunnelling MR (TMR) ratio at 4.2 K of 15%. Julliere

also developed theory that linked the TMR ratio to polarizations of electron spins in the electrodes; in this theory the tunnelling current is proportional to the junction joint density of states. Work on MTJs gained significance when in 1995 Moodera et al. and Miyazaki et al. [31; 32] found room temperature TMR ratios of 10-20% in MTJs using alumina $AlO_x$ tunnel barriers. These TMR ratios, comparable to the best GMR devices, were achieved by careful control of growth conditions to form amorphous, defect and pinhole free barriers. Eventually alumina based tunnel junctions reached a peak TMR ratio of ∼80% [33; 34].

In 2001 two theoretical publications were released [35; 36], using wavefunction symmetry arguments, they predicted that epitaxial Fe/MgO/Fe junctions would show TMR ratios greater than 1000%. This goes beyond Julliere's theory in that it introduces spin dependent elements into the tunnelling matrix. Because tunnelling current exponentially drops with barrier thickness, the tunnelling rate for one spin species can be orders of magnitude greater than the other. The structure is difficult to realise because it requires good crystalline matching between the electrodes and the insulator in order to ensure a coherent tunnelling process. The effect was first demonstrated by Yuasa et al. using molecular beam epitaxy (MBE) and by Parkin et al. using the commercially viable sputtering process [37; 38]. They both showed a TMR ratios of more than 200% at room temperature. It was later found that MgO grew better on amorphous CoFeB surfaces [39]; using these materials room temperature TMR ratios of up to 600% [40] and beyond have been demonstrated. These are more than enough for practical applications in memory read-out [41]. In all of these studies post-growth annealing is essential to get the correct crystalline orientation and the high TMR ratios. Temperatures in the range 200-400°C have been found to be optimal [42]. The design of the tunnel junction stacks grown in this thesis comes directly from these studies.

## 1.2 Single electron physics

This field concerns itself with the control of individual electrons on nanometre sized conducting islands. This section will introduce the single electron transistor device and highlight some of the nearly five decades of research done into non-magnetic devices. Magnetic devices will be covered in the next section and will be the major subject of this thesis; this section will show the potential for what could be achieved with magnetic materials.

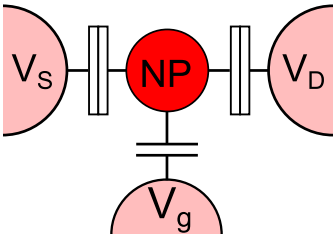


**Figure 1.1:** The basic set-up of a single electron transistor (SET). Source (S) and drain (D) leads are coupled to the nanoparticle through thin tunnel barriers. The backgate is capacitively coupled.

The basic unit for single electron experiments is the single electron transistor (SET), a circuit diagram of this device is shown Fig. 1.1. In the centre a nanoparticle or 'island' is linked to source (S) and drain (D) external electrodes by thin tunnel barriers and a further gate potential by a fully insulated layer. Conduction of current through the source and drain electrodes is governed by the classical charging energy $E_{\mathrm{C}} = e^2/2C$ of the island. Here C is the capacitance between island and leads. Finite SD bias $V_{\mathrm{SD}} > E_{\mathrm{C}}/e$ is required to charge the island with a single electron, this is known as Coulomb blockade (CB), below this voltage no current will flow. For greater applied bias, the current is governed by the charge state of the island and will increase stepwise as electrons are added, this is known as the Coulomb staircase. A gate potential will offset the charging state, giving further control over the conduction. CB and the Coulomb staircase are the hallmarks of single electron physics. The main physical criterion for their manifestation is that the thermal energy $k_{\mathrm{B}}T$, be much less than the charging energy $E_C$. This criterion is satisfied at room temperature for particles less than a few nanometres in diameter, although it depends on the exact geometry of the setup.

The manipulation of single electrons in solid state devices has its origins in studies of granular tunnelling barriers pre 1980 [43–47]. These results were somewhat ignored until developments in nano-patterning technology allowed controllable devices with individual islands and multiple gates to be created. Fulton and Dolan [48; 49] created the first true SET using multi-angled deposition through undercut resist, it showed the expected Coulomb staircase with Coulomb blockade modified by a gate potential. The theory, known as the orthodox model, used to describe these devices was also developed at this time with major contributions by Likharev [50] and Averin [51]. Motivation

for further experiments remained high, it was thought that by building transistors specifically to work with individual electrons, logic could be done at the smallest scale, negating some of the problems faced with scaling down Si based CMOS technology [52]. SETs continued to decrease in size and operate at higher temperatures [53–56], eventually reaching room temperature operation [57–59]. For an excellent review of this period see Likharev (1999) [52].

It was recognised early on that scanning tunnelling microscopy (STM) would also be useful tool for single electron devices, acting as a drain electrode above a nanoparticle connected to a base electrode below. Initial measurements were often made by simply scanning self-assembled particles on an oxide surface [60–70], the results mostly confirmed the simple theoretical predictions made for these devices. Using STM it was much easier to create smaller devices and room temperature SETs were developed early on. A limitation of the STM was that it was difficult to combine it with a third gate electrode. One group was able to overcome this by combining STM with e-beam lithography (EBL) [71] to create a small probe/gate combination tip.

It gradually became evident that there were significant physical limits to using these devices in logic circuits [52; 72; 73], mostly due to their high sensitivity to environmental charges causing high bit error rates. In the new millennium the pace of development in SETs has slowed but more niche applications have been developed. SETs produce very abrupt signals and they are highly sensitive to local charge. This can make them useful as measurement standards and thus have been used for charge [74; 75], current [76] and spatial displacement [77] metrology. New materials have been used including carbon nanotubes [78], and smaller islands have naturally lead on to the study and spectroscopy of quantum dots, which are small enough that their kinetic energy levels are discretised [79]. The conducting requirement of the island is not very stringent and both doped semiconductors [80; 81] and superconducting islands [82; 83] show CB effects. Superconducting islands with energy gap $\Delta$ were used to interesting effect, showing odd and even electrons adding with energy $2V_0 \pm \Delta/e$ [82]. Novel thermodynamic applications as electronic refrigerators have been suggested [84]. Finally, further development of spintronics has focussed interest onto magnetic SET devices, research now classified as nanospintronics.

## 1.3 Nanospintronics

One obvious extension to single electron physics, was to study the effects of building SETs out of magnetic electrodes and islands. This tied in well with spintronics studies into magnetic tunnel junctions: much of the research into barrier quality and magnetic materials could be applied directly to the new field. The combination of these disciplines became known as nanospintronics.

Research into nanospintronics began in earnest in the 1990's as single-electron physics matured and spintronics became industrially relevant. Groups began to study the effect of discontinuous layers inserted into GMR stacks: Fujimori et al. [85] reported MR in thick Co-Al-O granular material. Schelp [86] and Dieny [87] and co-workers grew MTJs with discontinuous Co layer inserts, known as double magnetic tunnel junctions (DMTJs). DMTJs in general consist of two tunnel barriers in series with a discontinuous or single particle central electrode. Two out of the three electrodes will be a ferromagnetic material, in any combination, the third maybe ferromagnetic or normal metal. Both the Schelp and Dieny groups showed MR and tunnelling like transport, however the single electron characteristic of the junctions was all but washed out due to averaging over a large distribution of particles.

The first spin dependent SET type devices with a single island were developed by the Ootuka group from the university of Tokyo [88–90]. They measured Ni/$NiO_x$/Co(island)/$NiO_x$/Ni structures defined by double-angle deposition through a silicon nitride membrane mask. The MR was enhanced within the Coulomb blockade region ($T < 20$ mK, $V \lesssim 100$ μeV) by a factor of 10, achieving a maximum of 40%. This was attributed to the second order tunnelling process known as cotunnelling, which dominates transport within the CB region. Cotunnelling processes generate very small currents, but depend on the square of the tunnelling conductance, so are expected to be more sensitive to spin dependence than first order processes. Cotunnelling was put on sound theoretical footing by Iwabuchi et al. and Takahashi et al. [91; 92]. Research into cotunnelling enhancement of MR has continued into recent times [93–96].

The devices of the Ootuka group were also the first to exhibit another effect known as the magneto-Coulomb interaction. These experiments show Coulomb oscillations vs. applied magnetic field [89; 90]. In a standard SET with a small bias applied between source and drain electrodes, scanning the gate voltage leads to Coulomb oscillations as the island charging energy levels are adjusted. With a magnetic field applied, the

Zeeman effect will shift the electrochemical potential by $\Delta\mu = -\frac{1}{2}Pg\mu_B B$ where $P$ is the spin polarisation at the Fermi energy, $g$ the electron g-factor and $B$ the applied field. This is effectively the same operation as the gate voltage, and the comparison of this with the charging energy can yield the spin polarisation of the material. These experiments were done in magnetic fields up to 8 tesla.

This thesis will primarily be concerned with spin accumulation in nanoparticles, though many other experimental paths have been investigated, for a review see [7] or [97]. These include Kondo physics [98–100], the generation of electromotive forces [101] and spin suppression of superconductivity [102].

### 1.3.1 Single particle DMTJs

Despite the extensive developments in the theory of DMTJs (covered in more detail in chapter 5) and the growing body of experimental work, very few groups have achieved CB measurements on a DMTJ including a single isolated metal nanoparticle. A major aim of this PhD was to investigate a single particle DMTJ using scanning tunnelling microscopy.

Isolated particle setups are difficult to manufacture: growing and contacting to nanoparticles with less than 10 nm diameter is stretching the resolution of most nanofabrication methods to the limit. There are big advantages to working with single particle systems however: they are physically simpler than multigrain systems, and can be modelled and analysed more accurately. Despite the experimental difficulties a few groups have characterised individual particle systems.

In Cornell University a team headed by Ralph uses reactive ion etching (RIE) to create point contacts above self assembled nano-islands. The RIE process uses a $CHF_3/O_2$ gas mix to etch a bowl shaped point contact into a 50 nm thick $Si_3N_4$ membrane. By slightly overtuning the etch, a small 5-10 nm hole is left in the bottom. A metal electrode is grown into the point contact, while the bottom of the membrane is coated with nanoparticles. The nanoparticles are created by standard self assembly methods. A thin ($< 1$ nm) layer of metal is deposited onto an oxide such as $AlO_x$, the surface energy mismatch means the metal agglomerates into particles on the surface, 2-4 nm in diameter. If the conditions are right a single particle is left in the point contact [53; 103; 104]. Using this method the group measured the Coulomb staircase on ferromagnetic nanoparticles [104; 105]. Detailed spectroscopy of these excited levels

under applied magnetic field have yielded information about the spin wave excitations, spin filtering and spin orbit effects in these particles [106–108].

A team at Tohoku University have spent several years working on single electron transport. Their samples are generally made with self assembled nanoparticles inside double tunnel junctions, they rely on the roughness of the barrier to have the transport through one or a few particles. Yakushiji et al. have investigated spin accumulation in Co particles and shown spin lifetimes $10^6$ times longer than bulk Co [109]. They attributed this to discrete energy levels in the particle causing reduced spin flip scattering. Other studies have looked further at CB effects, cotunnelling and spin accumulation in Fe or Co particles with various barrier and electrode materials [6; 110–112].

At the Université de Paris-Sud, Bernand-Mantel et al. have used individual gold nanoparticles contacted by Co electrodes to investigate the anisotropic magneto Coulomb (AMC) effect [113]. They show that AMC and spin accumulation can be comparable in size difficult to distinguish [114]. To contact to a single particle they use a cantilever to make a nano-indentation into resist above a particle. The indentation process is monitored in real time by tunnelling current [115]. The AMC effect continues to be investigated for potential logic or memory applications [116; 117].

Other groups have had some success with shadow masking combined with multi-angled deposition. Masks can be bridges patterned using EBL [33; 90; 118–120], undercut resist [54] or patterned strips [121; 122]. All have shown single electron effects, though the results tend to be ill defined or inconsistent. More recently Liu et al. have used cutting edge EBL and ion milling fabrication to make a 40 nm diameter nanopillar with a continuous CoFe layer inserted into a tunnel junction [123]. This shows clear TMR oscillations with a period of 2 mV. This technique has potential for future detailed experiments.

There have been surprisingly few studies using STM on magnetic particles. It is a very flexible technique for addressing single particles with a variable tunnel barrier size, and there have been a large range of studies on non-magnetic particles [60–70; 124; 125]. There have, however, been a small number of experiments on magnetic particles. Mitani, Takanashi et al. have used STM to investigate granular films of Co particles [126–128]. They compared these to non-magnetic particles and showed some evidence of spin accumulation. Graf et al. (2002) measured CB on Co particles at room temperature [129], showing CB effects but no spin accumulation. Finally Wulfhekel et

al. (2005) [130] measured self assembled Fe islands on 1.5ML MgO barriers. They investigated the effect of the Fe band structure on the CB gap width.

## 1.4 Thesis overview

We have seen there is significant room for STM based work in the field of nanospintronics. The main aim for this PhD was to investigate tightly controlled DMTJs using STM, and along the way the formation and magnetic properties of the nanoparticles were studied.

This thesis is divided into three fairly distinct lines of investigation covered in chapters 4-6.

Chapter 4 is concerned with characterisation of the magnetic properties of the nanoparticles. The gas aggregation source is an ideal tool for investigating magnetism in size controlled, high purity NPs. XMCD data shows that the orbital to spin ratio of the particles is correlated with the size, though it does not correspond to a simple surface/bulk model. Complementary SQUID-VSM and TEM studies combine to give information on the particle anisotropy and shape. Crowded particles yield unexpected interaction trends.

Chapter 5 covers theory we have developed to model the spin accumulation effects seen in transport studies. An analytical solution to an existing model is calculated. The solution shows CB staircase I-V profiles can give information on several barrier properties, including spin polarisation. The model shows that magnetic fields are unnecassary for spin accumulation studies, a significant difficulty to overcome in STM measurements.

Finally chapter 6 will describe the results obtained from STM experiments. Building up from the single barrier to double barrier to full DMTJ studies, the full system is experimentally examined. For the DMTJ measurements CB staircase is observed and Coulomb step widths are correlated with particle size as expected. The steps show negative differential and fit to a CB model with spin accumulation and variable barrier modifications.

Preceding the results, chapter 2 will give background information on some of the necessary existing theory for understanding these systems. Chapter 3 will cover the detailed experiment techniques, focussing where appropriate on equipment development necessary for these investigations.

# Chapter 2

Theory

Here we will go through some of the principal theoretical physics underpinning the experiments in this thesis. Analysis of the main experiment, spectroscopy on nanoparticles using STM, requires a good understanding of the solutions for quantum tunnelling and single electron physics. The studies of the magnetic properties of the nanoparticles rely on superparamagnetism, understanding how several different measurements can combine to form a complete picture. I will also cover some of the theory behind the x-ray magnetic circular dichroism experiments.

## 2.1 Tunnelling

One of the principle findings of quantum mechanics was that particles should be represented by wave packets $\Psi(\mathbf{r}, t)$ and, in an undisturbed system, evolve as a continuous function of time. This evolution is governed by the differential equation of Schrödinger [131]. The 1D form of this can be written

$$\left(-\frac{\hbar^2}{2m}\boldsymbol{\nabla}^2 + U(x,t)\right)\Psi(x,t) = i\hbar\frac{\partial}{\partial t}\Psi(x,t) \tag{2.1}$$

with $m$ the mass of the particle and $U(x,t)$ its potential energy. This is not dissimilar to the classical diffusion equation and particles/wave packets exhibit some familiar properties, including diffraction, barrier penetration and evanescence. This is the origin of quantum tunnelling. Quantum tunnelling theory was first developed in the 1920s by Fowler and Nordheim. It was initially applied to solving the problem of electric field emission of electrons from cold metals [132]. Later in the 1950s, new experimental techniques allowed Esaki [133], Giaever [134] to advance the field. They were able to study controllable solid state tunnel barriers and use them for tunnelling spectroscopy, a key technique for investigating QM states in condensed matter. They were awarded the Nobel prize in physics for their work along with Josephson [135] for theoretical advances. Tunnelling spectroscopy was taken further in the development of the STM, the invention of which generated another tunnelling Nobel prize for its inventors Binnig and Rohrer [136]. This added a microscopy element to the technique, allowing real space images of samples down to a sub-Å resolution. The tunnelling barriers important in this thesis will be the STM-sample barrier, which is simply a vacuum barrier based on work function potential, and the MgO solid state barrier which is more complicated.

### 2.1.1 WKB approximation

In practice, solving Schrödinger's equation analytically for anything other than a constant $U(x)$, is rarely possible. Even square potential barriers will obtain a linear distortion under an applied bias. If $U(x)$ varies slowly with $x$ however, a useful approximate solution that can be employed is known as the WKB or Wentzel-Kramers-Brillouin approximation. Following the success of treating electrons in a constant potential as a plane wave $\Psi(x) = \exp(ik_x x)$, the wave function is approximated to a similar form as $\exp(i\Phi(x))$ where $\Phi(x)$ is an arbitrary function of $x$ that we expand in powers of $\hbar$. This will be a good approximation in a potential that varies slowly compared with the electron wavelength. The expansion can be written [137]

$$\hbar\Phi(x) = \Phi_0(x) + \hbar\Phi_1(x) + \frac{\hbar^2}{2}\Phi_2(x) + \dots \tag{2.2}$$

Substituting 2.2 into the Schrödinger equation 2.1 and solving in successive powers of $\hbar$ yields solutions of $\Phi(x)$ of which we take the first two terms as significant. The wavefunction then becomes

$$\Psi(x) \approx \frac{C_+ \exp\left(\int \mathrm{d}x \sqrt{\frac{2m}{\hbar^2}\left(U(x)-E\right)}\right) + C_- \exp\left(-\int \mathrm{d}x \sqrt{\frac{2m}{\hbar^2}\left(U(x)-E\right)}\right)}{\sqrt[4]{\frac{2m}{\hbar^2}\left(U(x)-E\right)}}. \tag{2.3}$$

with constants $C_+$ and $C_-$ to be determined. This function describes exponential decay in the energetically forbidden barrier region ($U(x) - E > 0$) and a wave elsewhere. Finally, after some necessary analytical work to deal with the abrupt changes at the barrier turning points, we obtain the transmission probability for the barrier as

$$T(E) \sim \exp\left(-2\int_{x_1}^{x_2} \sqrt{\frac{2m(U(x)-E)}{\hbar^2}}\,\mathrm{d}x\right), \tag{2.4}$$

where $x_1$ and $x_2$ are the positions either edge of the barrier. Taking the simplest case of a constant $U(x)$ and $E = 0$, we see that the WKB approximation predicts an expontential decay of probability: $T \propto \exp(-2\kappa\Delta x)$, with inverse decay length $\kappa = (2mU/\hbar^2)^{1/2}$. $\kappa$ is proportional to the square root of barrier height and $\Delta x = x_2 - x_1$ the barrier width. This is a classic result in tunnelling theory.

### 2.1.2 Simmons model

Starting from the 1D WKB approximation to a single tunnelling event, Simmons [138; 139] developed the model to predict the current through a planar solid state tunnel

junction for a given applied bias. This model is still commonly used in experiments to fit I-V curves and extract barrier parameters like height and width.

The calculation starts with current density passing through the junction from the left as

$$J_L = e \int_0^\infty v_x n(v_x) T(E_x)\, \mathrm{d}v_x \tag{2.5}$$

where $v_x$ is the electron velocity and $n(v_x)$ is the electron density of states (DOS) of the left junction. Calculating the right flowing current in a similar manner and balancing the two rates gives a total output current. Assuming an isotropic DOS and a barrier of uniform height $\bar{\varphi} = (1/\Delta x)\int_{x_1}^{x_2} \varphi(x)\, \mathrm{d}x$, the total current density $J$ can be written

$$J \approx J_0 \left[ \bar{\varphi} \exp(-2\kappa\Delta x) - (\bar{\varphi} + eV) \exp\Big( -2\frac{(\bar{\varphi} + eV)^{1/2}}{\bar{\varphi}^{1/2}} \kappa\Delta x \Big) \right] \tag{2.6}$$

where

$$J_0 = \frac{e}{4\pi^2\hbar(\Delta x)^2} \quad \text{and} \quad \kappa = (2m\bar{\varphi}/\hbar^2)^{1/2}.$$

Eq. 2.6 has two terms describing the left and right going currents. In the low voltage regime ($V \ll \bar{\varphi}$) this general expression for the current can be approximated as

$$J = \frac{e^2(2m\bar{\varphi})^{1/2}}{4\pi^2\hbar^2\Delta x} V \exp(-2\kappa\Delta x). \tag{2.7}$$

The current is approximately linear with applied bias in this regime. Unsurprisingly given its origins, we retain the $\Delta x\bar{\varphi}^{1/2}$ exponential dependence seen in the WKB approximation. Eq 2.6 does not take into to account image potential induced in the system. The image potential has the effect of rounding the edges of the potential barrier and reducing the effective height, these changes are shown as dashed line in Fig. 2.1 (b).

### 2.1.3 BDR

Simmons model deals quite well with symmetric junctions but cannot fit systems with an asymmetric bias dependence [141]. Figure 2.1 demonstrates this concept. We start from two disconnected materials with work functions $\varphi_1$ and $\varphi_2$ in (a). As they are brought into tunnelling range the materials will equilibrate to a trapezoidal shaped tunnel barrier, with height difference $\Delta\varphi = \varphi_2 - \varphi_1$. The BDR or Brinkman-Dynes-Rowell model deals with this issue, at the expense of losing the analytical solution of

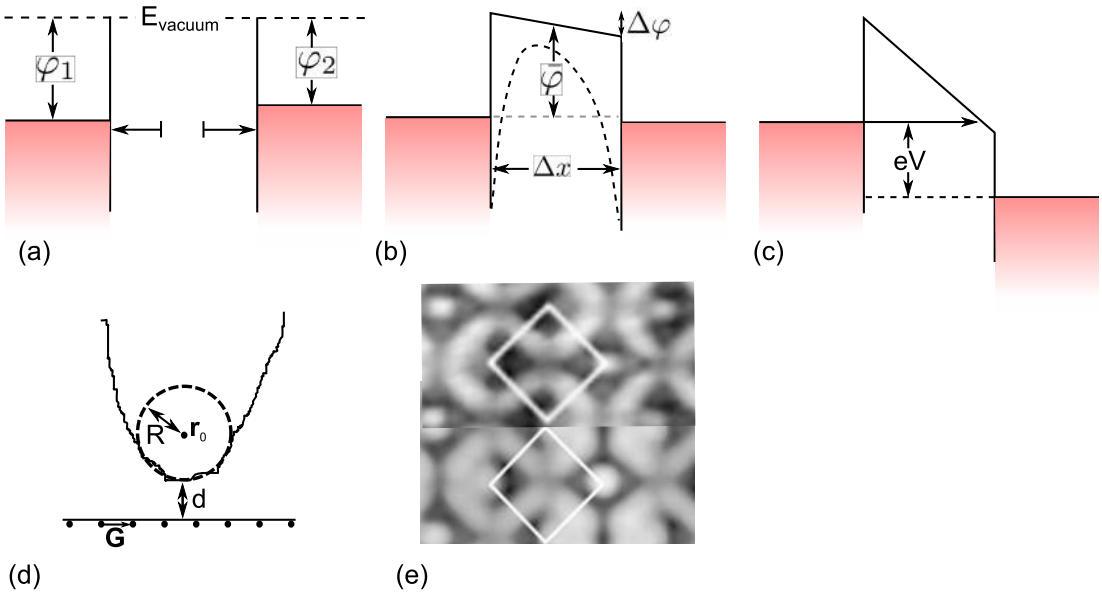


**Figure 2.1:** Diagrams illustrating tunnelling in solids. (a) and (b) show electrodes with asymetric workfunctions equilibrating in contact to form a trapezoidal tunnel barrier. At high applied bias eventually a triangular barrier shape is generated shown in (c). For tunnelling in an STM type geometry the Bardeen approach is employed, the model is given in (d). In (e) this model is used to simulate an STM image of Pd oxide, the real image is above and the simulation compared below, image taken from [140]

Simmons [142]. Starting from WKB and following similar methods, the BDR solution is expanded in powers of $V$ and typically quoted to the cubic term:

$$J(V) = J(0)\left(V - \frac{\sqrt{2m}e}{24\hbar}\frac{\Delta x \Delta\varphi}{\bar{\varphi}^{3/2}}V^2 + \frac{2me^2}{24\hbar^2}\frac{\Delta x^2}{\bar{\varphi}}V^3\right) \tag{2.8}$$

where the zero bias conductance is

$$J(0) = 7.9 \times 10^9 \left(\frac{\varphi^{1/2}}{\Delta x}\right) \exp(-2\kappa\Delta x)\ \Omega^{-1}\mathrm{m}^{-2}.$$

BDR includes the effects of image forces and has been used for reliable fitting up to ~0.5 V [143]. Inaccuracies in the fitting parameters can be introduced by an inevitable distribution of barrier widths in a real junction.

### 2.1.4 Fowler Nordheim tunnelling

The Simmons model also covers the high voltage regime where $eV > \bar{\varphi}$. In this region the barrier is a triangular potential and its effective width changes as a function of applied bias. This situation is shown in Fig. 2.1 (c). Field induced electron emission from cold metals, first studied by Fowler and Nordheim in the 1920s [132; 144], is a classic example of this type of barrier. In this region equation 2.6 reduces to

$$J \approx \frac{2.2e}{16\pi^2\hbar\bar{\varphi}\Delta x^2}(eV)^2 \exp\left[0.68\left(\frac{2m}{\hbar^2}\right)^{1/2}\frac{\Delta x\bar{\varphi}^{3/2}}{eV}\right]. \tag{2.9}$$

In this case the current depends exponentially on both barrier width and applied bias. This will be an useful model in this thesis because of the large applied bias used.

### 2.1.5 Bardeen tunnelling

While the Simmons and BDR models have been successful for fitting planar tunnel junctions they struggle to work with the inherently more 3D system of an STM [145; 146]. The basic picture of this is shown in Fig 2.1 (d). The end of the tip is typically modelled as a sphere of radius $R$ a distance $d$ above the surface of interest. It is no longer appropriate to start with plane wavefronts on the barrier so instead we model the wave function in the tip to have spherical symmetry.

As proposed by Bardeen (1961) [147] the current is determined from first order time dependent perturbation theory. Starting with Fermi's golden rule, we write

$$I = \frac{2\pi e}{\hbar}\sum_{\mathrm{LR}} f(E_\mathrm{L})[1 - f(E_\mathrm{R} + eV)]\,|M_\mathrm{LR}|^2\,\delta(E_\mathrm{L} - E_\mathrm{R}) \tag{2.10}$$

where $f(E)$ is the Fermi function and $M_{\mathrm{LR}} = \langle \Psi_{\mathrm{L}} | H' | \Psi_{\mathrm{R}} \rangle$ is the perturbing matrix element linking the left $L$ and right $R$ electrode's states. This can be solved according to Bardeen as

$$M_{\mathrm{LR}} = -\frac{\hbar^2}{2m} \int \mathrm{d}\mathbf{S} \cdot (\Psi_{\mathrm{L}}^* \boldsymbol{\nabla} \Psi_{\mathrm{R}} - \Psi_{\mathrm{R}} \boldsymbol{\nabla} \Psi_{\mathrm{R}}^*) \tag{2.11}$$

where the integral is over a surface in space between the two electrodes. Tersoff and Hamann (1983) [148] applied this technique to the STM geometry, putting planar and spherical wavefunctions in to $\Psi_{\mathrm{L}}$ and $\Psi_{\mathrm{R}}$ respectively. These are written

$$\begin{aligned} \Psi_{\mathrm{L}} =& \Omega_{\mathrm{L}}^{-1/2} \mathrm{e}^{-\kappa z} \sum_{\mathrm{G}} a_{\mathrm{G}} \exp\left[-(\kappa^2 + \left|\mathbf{k}_{\parallel} + \mathbf{G}\right|^2)^{1/2} z\right] \exp\left[i(\mathbf{k}_{\parallel} + \mathbf{G}) \cdot \mathbf{x}\right] \\ \Psi_{\mathrm{R}} =& \Omega_{\mathrm{R}}^{-1/2} c_{\mathrm{R}} \mathrm{e}^{-\kappa(\Delta x - z)} \frac{\mathrm{e}^{-\kappa|\mathbf{r}-\mathbf{r_0}|}}{\kappa|\mathbf{r}-\mathbf{r_0}|} \kappa R \mathrm{e}^{\kappa R} \end{aligned} \tag{2.12}$$

where $\Omega_{\mathrm{L,R}}$ is the sample and tip volume respectively, $\mathbf{G}$ are the 2D reciprocal lattice vectors at the sample surface, $\mathbf{k}_{\parallel}$ is the surface wavevector, $\mathbf{r}_0$ points to the centre of the tip sphere and $R$ is the tip radius. Using these forms of the wavefunctions to calculate $M_{\mathrm{LR}}$ and putting it all into eq. 2.10 we have for small applied biases

$$I = 32\pi^3 e^2 \hbar^{-1} \bar{\varphi}^2 R^2 \kappa^{-4} e^{\kappa R} D_{\mathrm{L}}(\mathbf{r}_0, E) D_{\mathrm{R}}(E_{\mathrm{F}}) V \mathrm{e}^{-2\kappa z} \tag{2.13}$$

where $D_{\mathrm{L}}, D_{\mathrm{R}}$ are the densities of states for sample and tip respectively. Like the Simmons result this is ohmic for small voltages. Importantly it contains information about the lateral resolution of the STM, predicting a resolution for Au(110)-2×1 of $\leq 5$ Å, later experimentally confirmed [149]. Tersoff-Hamman is used for simulating STM images [150], an example fit of a real STM image of a PdO surface pattern is compared in Fig. 2.1 (e) [140]. Both Simmons and Tersoff-Hamman give similar results for z dependence, finding an inverse decay length of $2\kappa$ [151]. The more important approximations made in the Bardeen approach, are that the coupling is weak so that first order perturbation theory applies, e-e interaction is ignored and that tip and sample are at electrochemical equilibrium.

### 2.1.6 Tunnelling in single electron systems

In Coulomb blockade we will see later there is a free energy change $\Delta U$ associated with tunnelling that must be taken into account. To deal with this we again start with Fermi's golden rule eq. 2.10, but modify it to account for the energy change

$$\Gamma(\Delta U) = \frac{2\pi}{\hbar} |M_{\mathrm{LR}}|^2 \sum_{LR} f(E_L)(1 - f(E_R)) \delta(E_L - E_R - \Delta U). \tag{2.14}$$

Here we may use the occupation function at the Fermi level on both sides, there is little change in the Fermi level on tunnelling. We use the densities of states to change the sum over momentum states into integrals over energy. We also approximate that in the small range of energies available, the density of states and tunnelling matrix are constant with respect to energy. This allows

$$\Gamma(\Delta U) = \frac{2\pi}{\hbar} |M_{\mathrm{LR}}|^2 D_L(E_F) D_R(E_F) \int_{E_c}^{\infty} f(E)(1 - f(E - \Delta U)) \, \mathrm{d}E \tag{2.15}$$

Solving the integral with standard methods yields finally

$$\Gamma(\Delta U) = \frac{-\Delta U}{e^2 R[1 - \exp(\Delta U / k_B T)]} \tag{2.16}$$

with $R = \hbar(2\pi e^2 |M_{\mathrm{LR}}|^2 D_{\mathrm{L}}(E_F) D_{\mathrm{R}}(E_F))^{-1}$ as an effective tunnelling resistance.

## 2.2 Magnetic tunnel junctions

All MTJs comprise three important layers: a bottom and top electrode of a material with a permanent magnetic moment and an insulating barrier between the two - typically an oxide such as MgO or $\mathrm{AlO_x}$. This barrier must be thin enough that significant tunnelling current may pass through; a suitable width is generally less than 3 nm. When a potential difference is applied across the junction, a current will traverse the barrier. If the magnetizations of the electrodes are parallel, the resistance ($R_{\mathrm{P}}$) is lower than the resistance if they are antiparallel ($R_{\mathrm{AP}}$). The percentage difference is the tunnelling magnetoresistance (TMR) of the junction and is given by [152]:

$$\mathrm{TMR} = \frac{R_{\mathrm{AP}} - R_{\mathrm{P}}}{R_{\mathrm{P}}} \times 100 \tag{2.17}$$

The resistance difference occurs when the electrons tunnel across the barrier while retaining their spin state. Due to exchange splitting in a ferromagnet, the density of states on either side of the barrier will be different for the two different spins. If the magnets are aligned parallel, the probability of the majority spins tunnelling is high, with large densities of states available for them to tunnel into. If the magnets are aligned antiparallel, the probability of either spin tunnelling is low, because the majority spin on one side is the minority spin on the other side. This leads to the characteristic magnetoresistance signal shown in Fig. 2.2.

Julliere [30] developed a simple model to calculate the TMR based on this two channel idea. In the parallel arrangement the conductance is proportional to $aa' +$

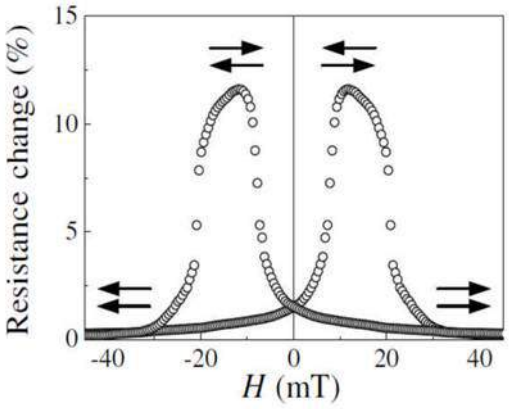


**Figure 2.2:** An example of an early measurement of TMR. Figure adapted from [32]

$(1-a)(1-a')$. $a$ and $a'$ are the fractions of tunnelling electrons, in the left and right electrodes respectively, whose spin is parallel to the magnetisation. In the antiparallel alignment the conductance should go as $a(1-a')+a'(1-a)$. Arranging this gives a final TMR as the Julliere equation:

$$\text{TMR} = \frac{2P_1P_2}{1-P_1P_2}, \tag{2.18}$$

where $P_1$ and $P_2$ are the spin polarisations for the left and right electrodes respectively[1].

Tunnelling in solid state junctions can be considerably more complicated than the simple picture presented above. Crystallinity, interfaces, barrier defects, disorder and band structure all come into play. Partly due to the possibilities for using MTJs in industry, a lot of work has gone into perfecting the production of MTJs and developing fuller theory to explain their properties. For a high quality review of MTJs up to 2003 see that by Tsymbal [153].

In particular epitaxial (001) Fe/MgO/Fe MTJs are found to have TMR values far exceeding those predicted by the Julliere model. Prior to measurement this effect was predicted through tight binding calculations by Mathon and Umerski [36] and through first principals DFT theory by Butler et al. [35]. It was shown that the system Bloch state with $\Delta_1$ symmetry (*spd* hybridised state) coupled most effectively from the Fe into the MgO. Majority states with $\Delta_1$ symmetry therefore coupled very

[1] $P$ is the usual symbol for the spin polarisation of a material $(D_\uparrow - D_\downarrow)/(D_\uparrow + D_\downarrow)$. Unfortunately it is also used in the orthodox single electron theory to describe the spin resistance ratio across a tunnel barrier $R_\uparrow/R_\downarrow$. In general the latter of these is used throughout this thesis unless otherwise stated.

effectively across the barrier, while minority states with $\Delta_5$ symmetry had a resistance that would be orders of magnitude higher. This gave predictions of TMR in excess of 1000%. Experiments are now approaching this value [40]. For a review of theoretical and experimental advances using these materials see Nagahama and Moodera (2006) [154].

## 2.3 Electron transport in nanoparticles

In solid state physics, electron-electron (e-e) interactions in metals can generally neglected, or be treated as a perturbation energy. This seemingly unlikely case is possible due to electrons filling coherent states up to the Fermi energy. These states already take into account the periodic potential of the lattice. This allows electrons around the Fermi energy to be treated as quasi particles which will scatter off only impurities or interruptions in the periodic lattice potential. In single electron physics, electrons are confined to a small conductor so their interactions must be taken into account. Taking e-e interactions into account is usually extremely challenging and is rarely fully solved. In single electron physics however, it is simply a case of calculating the classical Coulomb charging energy of the island, given its capacitance to the surrounding electrodes.

In section 1.2 we introduced the single electron transistor, the simplest device that can show all of the single electron effects, Coulomb blockade, Coulomb staircase and Coulomb oscillations. The theory developed to explain this system by Likharev, Averin and Nazarov and others [50; 51] is known as the 'orthodox theory' [155; 156]. Since some of the major results of this thesis are a development of this model centred on attempting a deeper understanding of its consequences, I will cover the relevant aspects in some detail. The devices experimentally investigated in this thesis do not have a controllable gate potential, so we simplify the SET to the double tunnel junction model shown in Fig. 2.3 (a).

### 2.3.1 Orthodox theory of Coulomb blockade

The model is given according to Fig. 2.3 (a). The system comprises two electrodes linked by tunnel barriers to a central island. The left and right tunnel barriers are each effectively a resistance $R_i$ and a capacitance $C_i$ in parallel ($i = 1, 2$), they surround

the island containing $N$ excess electrons. Potential $V$ is applied to the right electrode so that positive applied bias causes electrons to flow left to right (1 to 2). The rate of electrons tunnelling onto (off) the island are given by $\Gamma^+$ ($\Gamma^-$). As derived in the section 2.1.6 these rates are given by

$$\Gamma(\Delta U_i^{\pm}) = \frac{1}{e^2 R_i} \frac{-\Delta U_i^{\pm}}{\left(1 - \exp(\Delta U_i^{\pm}/k_B T)\right)} \tag{2.19}$$

with $\Delta U_i^{\pm}$ the change in the system free energy due to the tunnelling process. This function for $\Gamma$ is plotted in Fig. 2.3 (b), it asymptotes to 0 for $\Delta U \gg k_B T$ and to $-\Delta U_i^{\pm}/(e^2 R_i)$ for $-\Delta U \gg k_B T$.

The energy change $\Delta U_i^{\pm}$ is given by the difference in free energy from before and after the tunnelling process. The relevant free energy is the stored electrostatic energy in the barrier electric fields, minus the work done (w.d.) by the voltage source to match the island charge. This is given by

$$U = \frac{q_1^2}{2C_1} + \frac{q_2^2}{2C_2} - \text{w.d.} \tag{2.20}$$

where $C = C_1 + C_2$ and w.d. to charge a single electron from the left is $eVC_2/C$ and similar for right. By restricting the sum of the charges on the island to be integral $q_2 - q_1 = Ne$, we can find the free energy changes as

$$\begin{aligned} \Delta U_1^{\pm} &= \frac{e^2}{C}\left(\frac{1}{2} \pm \left(-\frac{C_2 V}{e} + N - Q_0\right)\right) \\ \Delta U_2^{\pm} &= \frac{e^2}{C}\left(\frac{1}{2} \pm \left(\frac{C_1 V}{e} + N - Q_0\right)\right), \end{aligned} \tag{2.21}$$

where $Q_0$ allows for some fixed static charge present in the environment close to the cluster. This static charge is often found in SETs based on dielectric tunnel barriers, and is caused by charge defects in the barrier [61]. $Q_0$ induces an offset to the Coulomb staircase and an adjustment of the Coulomb blockade shape, these effects are shown on the grey set of curves in Fig 2.3 (c).

These mathematical expressions for free energy changes can be simply visualised in a similar fashion to quantum dot diagrams, as pictured in Fig. 2.3 (d). This allows quick determination of favourable tunnelling conditions. The potential changes are not to be confused with the dense kinetic energy states present in any conductor however. The Fermi energy effectively sits at the potential level of the island and the density of

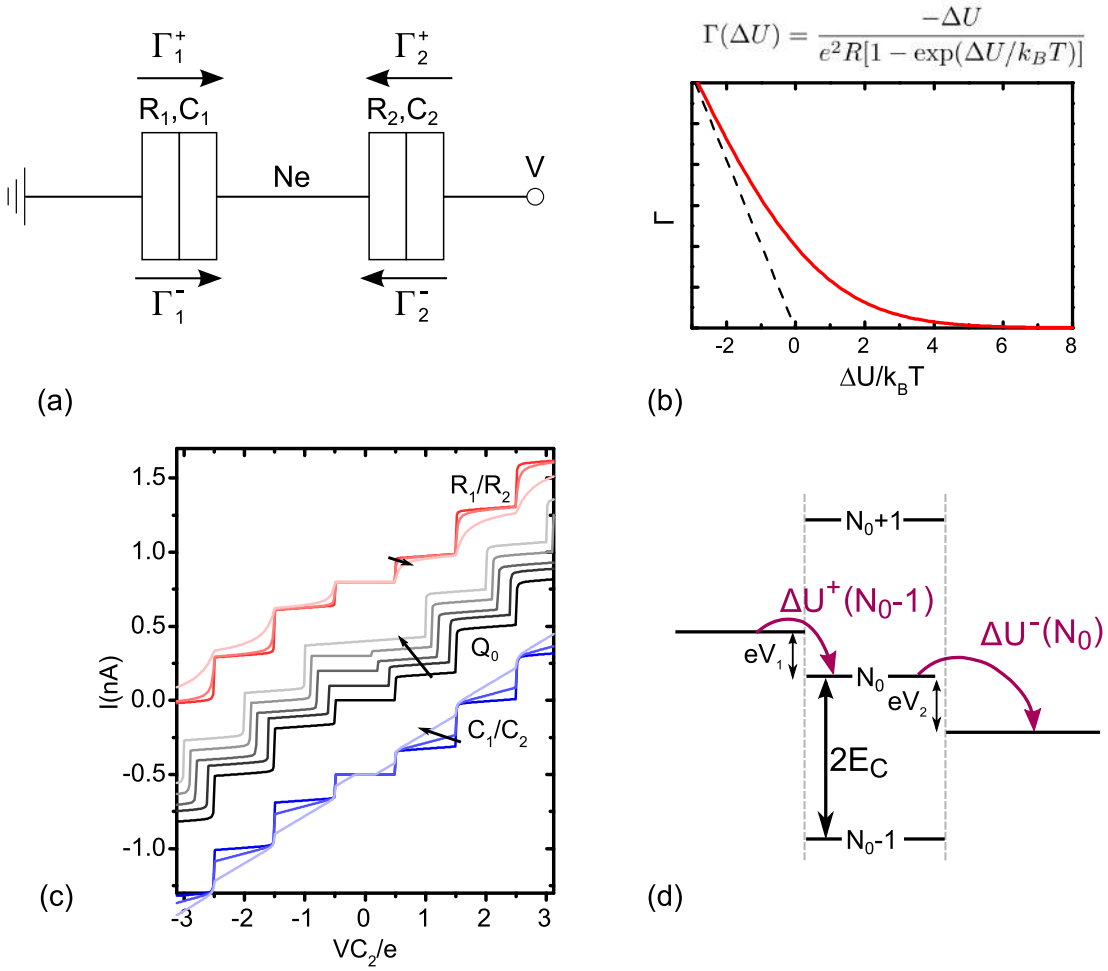


**Figure 2.3:** The orthodox model of the Coulomb blockade. The model circuit diagram is shown in (a). (b) the tunnelling rate $\Gamma$ as a function of the tunnelling free energy, this asymptotes at large values of $\Delta U$, shown as a dashed line. (c) numerical simulations using the model, the result of tuning the barrier parameters. The black arrows indicate the direction of the labelled variable increasing. Curves are offset vertically from (0,0) for clarity. The parameters for the basic staircase in each case are $T = 0$, $Q_0 = 0$, $C_1 = 0.1$ aF, $C_2 = 1$ aF, $R_1 = 1$ M$\Omega$, $R_2 = 1$ G$\Omega$. The $C_1/C_2$ ratios are 0.1, 0.5 and 3, the $Q_0$ values are 0 to 0.5 in increments of 0.1 and the $R_1/R_2$ ratios are $10^{-3}$, $10^{-2}$ and $10^{-1}$. (d) an energy diagram representation used to determine whether whether transitions on to and off the island will be favoured in a given situation.

states is simply translated up and down, with little modification when electrons tunnel in and out.

To calculate the current, we need to make the assumption that the electron wave function is well located on the island, and does not spread out onto the electrodes. This allows us to treat the problem in a Fock-space approach, with island states having exactly $N$ excess electrons (i.e. $|N - \langle N \rangle|^2 \ll 1$ with $\langle N \rangle$ the expectation value of $N$). This assumption will hold if the resistance to the leads is sufficiently great $R > h/e^2 = R_Q$. [2]

In the case $N$ is a good quantum number, we may incoherently sum the rate contribution from each state $N$, weighted by $\sigma(N)$ the probability of the island being in that state.

$$I(V) = e \sum_{N=-\infty}^{\infty} \sigma(N)(\Gamma_2^-(N) - \Gamma_2^+(N)) \tag{2.22}$$

The classical requirement for rate equilibrium in the steady state allows us to calculate the $\sigma(N)$ using a master equation

$$\sigma(N)(\Gamma_1^+(N) + \Gamma_2^+(N)) = \sigma(N+1)(\Gamma_1^-(N+1) + \Gamma_2^-(N+1)), \tag{2.23}$$

with the normalisation condition

$$\sum_{N=-\infty}^{\infty} \sigma(N) = 1. \tag{2.24}$$

Solving these equations numerically and fitting to experimental CB data often gives an excellent fit to the various features [54; 61; 122]. I numerically solve these equations and show some simulations of the various parameter families in Fig. 2.3 (c). The clearest CB staircase are given when the competing requirements $R_1 \gg R_2$ and $C_1 \gg C_2$ are realised. The details for solving the equations will be given in more detail in chapter 5.

One final important assumption that we made in this theory was that the electron kinetic energy states are continuous at the Fermi energy $E_F(N)$, so that $E_F(N+1) -$

[2] A qualitative argument for this inequality can be made by comparing the time $t$ which the electron resides on the island to $\Delta t$ the quantum uncertainty in this time. For the island to be a well defined state $N$, we require $t \gg \Delta t$. From the uncertainty principle we also have $\Delta t > h/\Delta E$. At low bias the current is approximately the turnstile value $I = e/t$ and the energy uncertainty is at least less than the applied bias $\Delta E < eV$. Combining these gives us the desired inequality $R = V/I \gg h/e^2$. A full quantum treatment of the system yields the same result [51]

$E_F(N) \ll E_c$. For metals with free electron carrier concentration $n$:

$$E_F = \frac{\hbar^2}{2m^*}(3\pi^2 n)^{2/3}. \tag{2.25}$$

Putting in typical numbers for an Al particle of 3 nm diameter (small for work in this thesis) the change in $E_F$ on adding one electron is approximately 1 meV, well below the thermal energy range considered in these experiments. This may not be the case when considering semiconducting particles.

## 2.4 Magnetism of nanoparticles

### 2.4.1 Anisotropy

The internal energy of a bulk ferromagnet (FM) is anisotropically dependent on the direction of the magnetisation. In FM nanoparticles there are generally three major contributors to the magnetic anisotropy: the crystal structure of the material, the surface magnetism and the shape of the sample.

**Magnetocrystalline (MC) anisotropy** causes alignment in certain crystallographic directions, it has a microscopic origin based on the spin-orbit coupling, though it is still not fully understood [157]. The anisotropy is proportional to the sample volume and its density is generally given as $K$ in units of $\mathrm{Jm}^{-3}$. Common examples are the uniaxial hexagonal system (bulk Co) or the cubic anisotropy in cubic crystals (bcc Fe, fcc Ni). In the magnetic media industry a particular interest is shown in very high ($> 1\ \mathrm{MJm}^{-3}$) uniaxial anisotropy systems such as tetragonal FePt or hexagonal Co [158].

**Surface anisotropy** is important for low dimensional magnets and is caused by the breaking of the crystal symmetry at the surface. Reconstructed surfaces have been found to enhance the total anisotropy of nanoparticles [159]. Surface contributions to nanoparticle anisotropy are proportional to $(\text{surface area})/(\text{volume}) = 6/d$ for $d$ the diameter of a spherical particle. Surface effects can in general be isolated from bulk effects by size dependent studies [160; 161].

**Shape anisotropy** is seen in non-spherical particles and is due to long range dipole forces generating a demagnetizing field. Mathematically the shape anisotropy in a

uniform magnetised ellipsoid can be written

$$E_{\text{shape}} = \frac{1}{2}\mu_0 V(N_x M_x^2 + N_y M_y^2 + N_z M_z^2) \tag{2.26}$$

where $N_i$ are the demagnetisation components. Oblate spheroids will have an easy plane sitting in the $x$-$y$ plane, prolate spheroids have a easy direction along the $z$-axis.

Nanoparticles with a diameter smaller than the domain wall width $\sqrt{A/K}$, will be single domain. Kittel [162] has roughly calculated the critical diameter of 20 nm for a typical ferromagnetic nanoparticle below which it will be single domain, though this is strongly dependent on shape and material and can vary by orders of magnitude. All particles in this thesis are considered single domain.

With $\theta$ the angle between magnetisation and the easy axis as shown in Fig. 2.4 (a), uniaxial anisotropy can be represented in general as series of even powers of $\sin(\theta)$:

$$E_{\text{uni}} = K_1 V \sin^2(\theta) + K_2 V \sin^4(\theta) + \ldots \tag{2.27}$$

Happily in most FM materials $K_2$ and higher order terms are negligible and can be ignored, considerably simplifying calculations. In the next section on superparamagnetism a uniaxial anisotropy with negligible $K_2$ will be used.

### 2.4.2 Superparamagnetism

Nanoparticles exhibit rich magnetic behaviour. Above a critical blocking temperature $T_B$ they will go into a superparamagnetic (SP) state. Superparamagnetism is analogous to the paramagnetic state, but with nanoparticles forming large 'super' moments. Standard SP measurement protocols are used in this thesis to characterise the particle ensemble magnetic properties, anisotropy, size distribution and dipolar interaction. In these experiments it is often possible to corroborate evidence using different measurement protocols on the same sample [163].

To understand this property we consider nanoparticles with uniaxial anisotropy and a single domain as described in the previous section. The energy diagram for this system is shown in Fig. 2.4. In order to flip, the particle must overcome an energy barrier $\Delta E = KV$. In fact the average rate at which it flips is given by an Arrhenious law

$$\tau_N^{-1} = \tau_0^{-1} \exp\left(-\frac{KV}{k_B T}\right), \tag{2.28}$$

where $\tau_0^{-1}$ is the so called attempt frequency and is generally found to be of the order 1-10 GHz [164]. Above the blocking temperature $T_B$ the magnetization direction will flip faster than the characteristic timescale of the measurement $\tau_m$. In this case ($\tau_m > \tau_N$), the cluster will appear to be a paramagnet with a large susceptibility, it will follow the Langevin function $L(x) = \coth(x) - 1/x$ where $x = \mu_0 H M_s V_c / k_B T$ and $M_s V_c$ is the moment $m$ of the cluster [165; 166]. In practise there will usually be a distribution of particle sizes measured, so that this Langevin must be fitted using a probability distribution of particle sizes $\rho(V_c)dV_c$. The magnetisation is given by

$$M(H) = \int_0^\infty \rho(V_c) M_s L(x) dV_c \tag{2.29}$$

As the particle gets larger the blocking temperature will tend to increase because the magnetocrystalline anisotropy is proportional to volume.

The full energy landscape for an individual particle is described by

$$E = \Delta E \sin^2(\theta) - \mu_0 \mathbf{m} \cdot \mathbf{H} \tag{2.30}$$

Below the blocking temperature the particle is described approximately by the zero temperature Stoner-Wohlfarth model [167]. Minimising the energy as a function of magnetic field yields the hysteresis loops shown in Fig 2.4 (b). A field applied parallel to the easy axis yields a square loop with a coercive field $H_\mathrm{k} = 2K/M_s$ (also known as anisotropy field). Stoner and Wohlfarth also calculated the hysteresis loop for an assembly of randomly oriented clusters and a found that the coercivity is reduced to $0.48 H_\mathrm{k}$.

Upon warming the energy barrier is easier to cross and this coercivity decreases. A simple calculation shows the barrier height goes as $\Delta E \approx KV - \mu_0 M_s V_c H$. Using this in combination with eq 2.28 a coercive field dependence of [168]

$$H_c = 2KV[1 - (T/T_B)^{1/2}]/m. \tag{2.31}$$

Due to the exponential sensitivities however, this formula is usually used as an approximate fit [169; 170].

### Measurement protocols

Superparamagnetic paricles in this thesis are characterised by SQUID-VSM. This sensitive technique allows various measurement protocols.

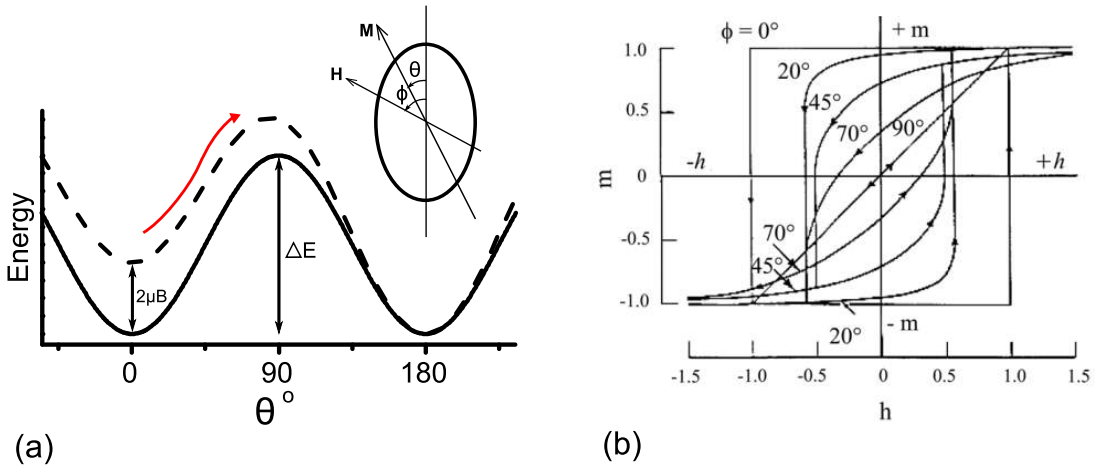


**Figure 2.4:** (a) The potential energy stored in a single domain uniaxial magnetic nanoparticle as a function of magnetization direction. An applied magnetic field adds a linear modification to the distribution shown by the dashed line. (b) predicted hysteresis loops as a function of applied field angle $\phi$, figure adapted from [167]

- *Zero field cooling and field cooling (ZFC-FC):* The sample is warmed to above $T_B$ then cooled under zero applied magnetic field to well below the blocking temperature. A small probe field is applied and the moment is measured during warming. The particles align with the applied field only when they reach their blocking temperature. The FC part is simply measuring while cooling the sample in that same field, the particles will cool into an aligned state so the magnetisation will deviate from the ZFC. This protocol gives information on blocking temperature and size distribution.

- *Hysteresis vs temperature:* Simply measuring a full hysteresis loop at different temperatures gives the change in coercivity as a function of temperature. This can give information on cluster anisotropy and blocking temperature. Above $T_B$ there is no hysteresis and the zero field susceptibility gives the average particle moment.

- *AC-susceptibility:* In this technique a small magnetic field is oscillated at varying frequencies and the magnetic response is determined. The ac-susceptibility $\chi$ is broken into an in-phase $\chi'$ and out-of-phase $\chi''$ components. Looking at the $\chi'$ vs temperature gives a peak responsiveness at the blocking temperature. By varying

the frequency and measuring the blocking temperature the attempt frequency $\tau_0^{-1}$ can be determined [171]. $\chi''$ gives information on the energy dissipation in the system due to irreversible processes. This can be caused by interactions between clusters, conformational changes or other irreversible mechanisms.

## 2.5 X-ray Spectroscopy

Part of the characterisation of the magnetic nanoparticles undertaken in this thesis has been through soft x-ray absorption spectroscopy undertaken at the Brookhaven National laboratory NSLS synchrotron source. There is a lot of complexity to photon interaction with matter and this section will cover very briefly some relevant aspects. For a comprehensive text see Stöhr and Siegmann (2006) [157].

### 2.5.1 X-ray absorption spectroscopy (XAS)

XAS essentially involves a photon impinging onto a material, being absorbed and in that process exciting a core electron. Fig. 2.5 (a) shows this process, the core electron leaves a hole indicated by an empty circle. Electrons drop to fill the core gap and in that process release secondary Auger electrons (in the soft x-ray regime Auger processes dominate over fluorescence). The experiments in this thesis were measured in the electron yield geometry, so that the signal was detected simply by counting the number of electrons leaving the sample using a picoammeter. These released electrons must necessarily come from the surface of the metal since the escape depth $\lambda_e$ of electrons from Co and Fe is approximately 2 nm [172]. Each core absorption process sets off a cascade of Auger electrons and several are released from the surface for each captured photon. Importantly the total yield is proportional to the x-ray absorption cross-section for the x-ray-electron interaction, hence this method determines the absorption cross-section of the material for a given input energy photon.

Materials exhibit an absorption resonance when the incoming photon is the same energy as an energy transition in the atom. In the soft x-ray regime the L edges of Co and Fe are probed, this equates to the atomic $2p \rightarrow 3d$ transition. In fact the resonance is split into two parts due to spin-orbit splitting of the $p$ electrons, these are the $L_3$ peak from $2p_{3/2} \rightarrow 3d$ and the $L_2$ from $2p_{1/2} \rightarrow 3d$. These resonances are also relatively broad, the core $p$ electrons are in a well defined atomic-like state, while the $d$ electrons

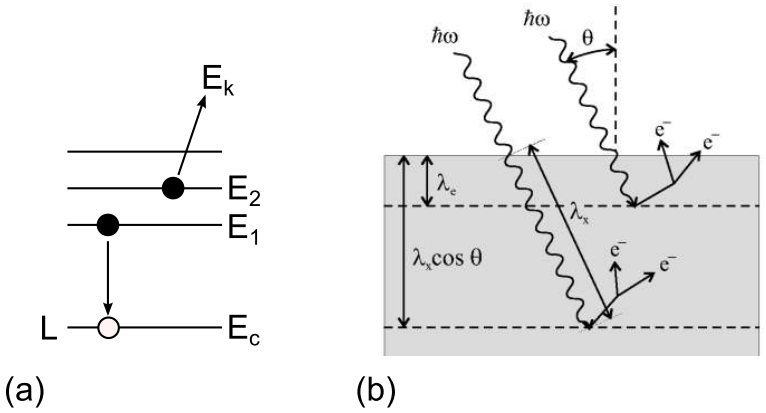


**Figure 2.5:** (a) atomic energy level diagram of the Auger process. The empty circle shows the gap left at the core L state that is filled by electrons dropping from above. (b) Electron cascade process caused by impinging photons. The photon penetration depth $\lambda_x$ and electron escape distance $\lambda_e$ are indicated. Figure adapted from [172].

are better described as a band structure with a broader width. An example XAS of Fe is shown in Fig. 2.6. The underlying (non-resonant) step-like feature is drawn as a dashed line, this is known to be in a 2/3 to 1/3 ratio for $L_3$, $L_2$ respectively [173]. Additional peaks or shoulders in the XAS spectrum give information on the chemical environment of the atoms. In a clean unoxidised metal the peaks are featureless. In transition metal oxides the $3d$ states are strongly correlated, which leads to clear fine structure. The multiplet splitting depends on the orbital quenching due to ligand field symmetry, and exchange and spin-orbit interactions. The total integrated intensity of the XAS spectrum for the L edge after subtracting the atomic step background is proportional to the number of holes $N_h$ in the $d$ band

$$I = CN_h \tag{2.32}$$

with $C$ a constant dependent only on the $p$ orbital characteristic.

### 2.5.2 X-ray magnetic circular dichroism (XMCD)

XMCD is based on the XAS method but specifically uses circularly polarised photons. Photons of opposite helicity interact with different electron orbital and spin moments, revealing some of the magnetic properties of the sample. Theoretical analysis has produced sum rules which allow a quantitative determination of the individual orbital

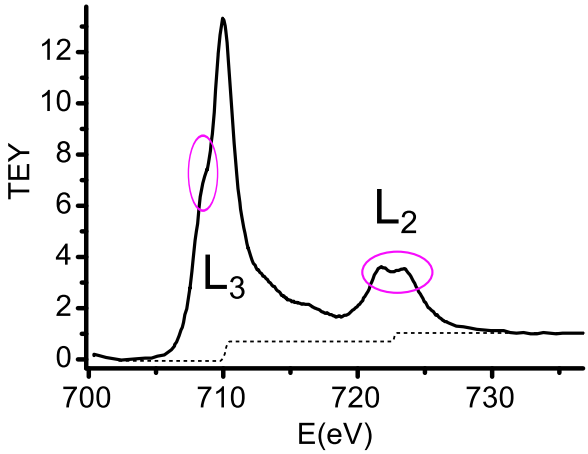


**Figure 2.6:** An XAS spectrum at the Fe L edge of partially oxidised CoFe nanoparticles. Fine structure from Fe-O chemical bonds is highlighted.

and spin moments in sample. This makes XMCD a powerful technique, element specific, chemically sensitive, quantitative and able to separate orbital and spin moment contributions.

A photon with a circular polarization has an angular momentum along or against the direction of the beam $\mathbf{L}_{\text{ph}}$. When interacting with the atom this angular momentum is transferred to the photoemission electron. Due to the spin-orbit mixing this angular momentum has a spin and an orbital component. If the sample is magnetised the $d$ band will be spin split; the difference in available valence states will act as a detector selecting for the majority state. This process is shown in Fig. 2.7 (a). The XMCD intensity is given as the difference between the absorption intensity for left $I^+$ and right $I^-$ polarised photons $I_{XMCD} = I^- - I^+$, an example spectrum is shown in Fig. 2.7 (b). The spin detection process relies on the magnet quantisation axis $\mathbf{m}$, aligning with the photon angular moment. It is also proportionally affected by the degree of beam polarisation $P_{circ}$, the XMCD signal is therefore scaled by a factor $P_{circ}\mathbf{L}_{\text{ph}} \cdot \mathbf{m}$. The incoming beam must have a direction component aligned with the magnetisation.

By adding up all the different allowed $p \rightarrow d$ transitions Carra et al. [175] developed a simple sum rule to calculate the average spin moment per atom based on the XMCD spectrum

$$m_s/\mu_B = (-A + 2B)/C \tag{2.33}$$

where $A$ and $B$ are the integrated areas under the $L_3$ and $L_2$ difference peaks re-

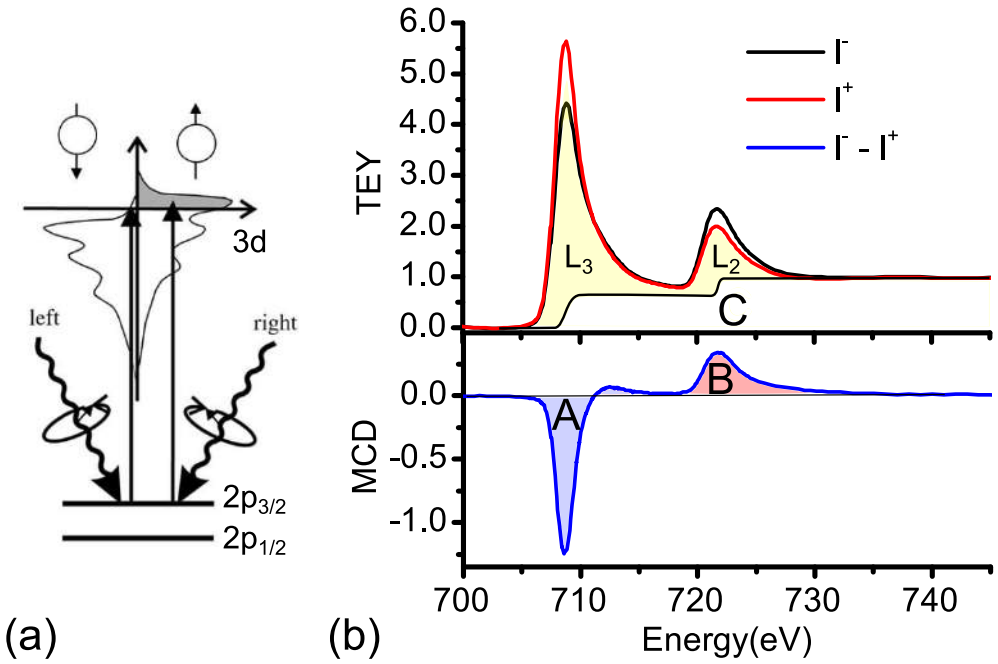


**Figure 2.7:** The XMCD at the Fe L edge. (a) is a representation of the energy levels involved (diagram adapted from [174]). (b) an example XMCD spectrum. The top panel shows the total electron yield signal as a function of beam energy, the bottom panel shows the difference plot. The integral areas A, B and C used for the sum rules are labelled.

spectively. C is an integral over the intensity signal after subtracting the non-resonant background signal (background subtraction shown in Fig. 2.7 (b)). By instead doing the sum of the $L_3$ and $L_2$ edges we cancel any spin component and only the orbital moment remains [176]:

$$m_l/\mu_B = -2(A+B)/3. \tag{2.34}$$

These sum rules have been demonstrated to give moments within a few percent of those found using gyromagnetic ratio measurements [173].

# Chapter 3

Methods

## 3.1 Introduction

This chapter will describe the various experimental techniques used in this thesis. The samples were fabricated in-house using magnetron sputtering and a gas-aggregation nanoparticle source. Characterisation can be broadly categorised into structural characterisation (AFM, TEM), magnetometry (XMCD, SQUID-VSM) and current perpendicular-to-plane (CPP) transport measurements (STM), though these techniques are all complementary to some extent. Upgrades to apparatus, particularly probe improvements for STM, will be detailed here.

## 3.2 Sample fabrication

The samples used in this project were thin film metallic/insulator stacks sputtered onto thermally oxidised Si wafer substrates. Metallic nanoparticles were then deposited onto the films within the same vacuum chamber using a gas aggregation nanoparticle source. The individual samples grown for each project will be described in more detail later.

### 3.2.1 High vacuum system

Sputtering requires a high vacuum environment to prevent interstitial impurities and chemical reaction during growth. The samples were grown in Leeds in a custom designed Kurt J. Lesker sputter system locally referred to as 'SLIM'. SLIM contains several pumping mechanisms. It is first roughed by a scroll pump to 5 Pa. After this the pumping is switched to a cryopump which condenses gas molecules onto a 10 K cold stage, cooled by a closed cycle $^4$He refrigerator. During operation a liquid nitrogen cooled Meissner trap in the chamber is used to reduce the water partial pressure by the same mechanism. Pressures are detected from vacuum to atmosphere by an Ionivac ITR90 combination wide range gauge, working gas pressures are given more accurately by an MKS Baratron capacitance gauge and individual gaseous partial pressures below $10^{-2}$ Pa are detected by a KJL accuquad quadrupole residual gas analyser. All pumps and motors on SLIM are computer controlled and can be automated through a recipe system. SLIM is run on a 24 hr pump-vent cycle allowing fast change around of target materials and substrates. The base pressure averages around $8\times10^{-6}$ Pa, typical molecular partial pressures at this point are listed in table 3.1.

| Molecule | Partial pressure (Pa) |
|---|---|
| $H_2$ | $3 \times 10^{-6}$ |
| $H_2O$ | $6 \times 10^{-6}$ |
| $N_2$ | $2 \times 10^{-6}$ |
| $O_2$ | $1 \times 10^{-7}$ |
| $CO_2$ | $3 \times 10^{-6}$ |

**Table 3.1:** Residual partial base pressures

### 3.2.2 Sputter deposition

Magnetron sputtering is a technique used to deposit tightly controlled, high purity, thin films onto surfaces. It was first introduced by Penning [177] in 1936 and is now widely employed in industry due to its speed, scalability and reliability [178]. The process of sputtering involves the bombardment of a high purity target by energetic ions. Energetic collisions cause the target to eject atoms and ions of the desired species, which then go on to coat any surface in the vicinity. To provide the ions which bombard the target, a small pressure of working gas is introduced into the growth chamber. The working gas must be chemically inert so that it does not react with the growing film, in our case Ar is used. When a negative electric potential is applied to the target an Ar plasma will form, providing a continuous source of $Ar^+$ ions which accelerate and collide with the target. The plasma is maintained by secondary electrons, which are ejected from the target during collisions and go onto ionise further Ar atoms. The plasma is confined via the electric field and a static magnetic field generated by opposing permanent magnets in the magnetron.

A diagram of the sputtering facility SLIM is shown in Fig. 3.1 (a). It is configured with ten target/magnet magnetron assemblies also known as sputtering guns (only two of which are shown for clarity). Four guns are specialised for magnetic targets, five for non-ferromagnetic materials and one source is used exclusively for rf sputtering. Up to two dc sources can be lit at one time and each gun has its own pneumatically controlled shutter, computer controlled for timed growths. A secondary rotatable plate shutter protects the samples and contains a magnetic array that produces a 15 mT growth field at the sample.

The design of the magnetron is shown in Fig. 3.1 (b). Central and ring permanent

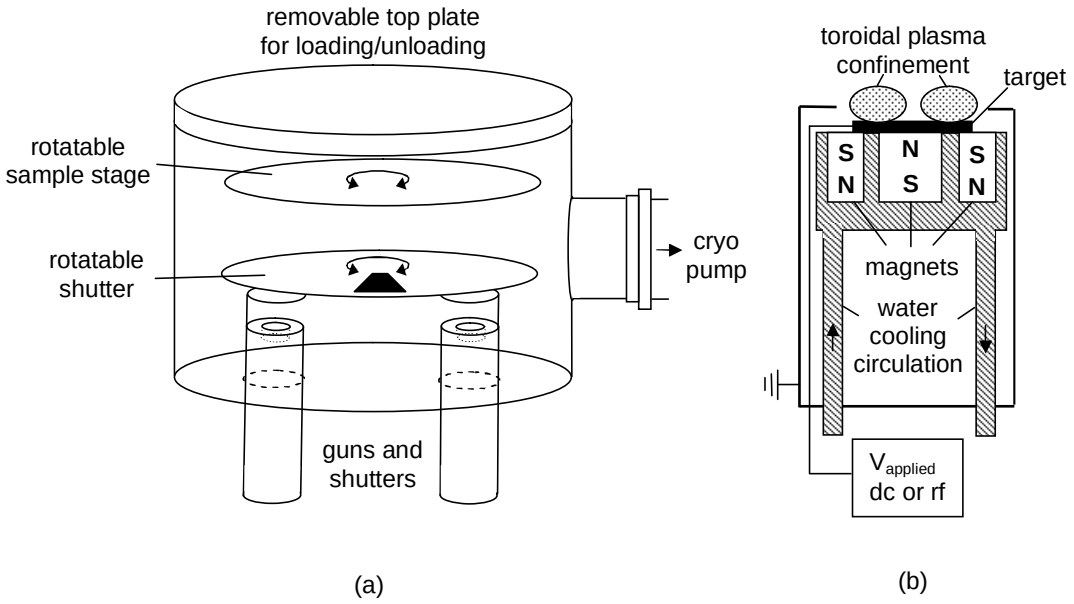


**Figure 3.1:** (a) A schematic diagram of the sputtering system. A rotatable shutter allows multiple guns to be lit at once while just sputtering one material at a time. (b) shows a cross-section of one of the magnetron sputtering sources

magnets produce a magnetic field which confines the Ar plasma to a toroidal space above the target. An earthed shield around the assembly is separated from the 2 inch diameter target by approximately 0.5 mm. dc bias is applied to conducting targets to generate the plasma. The assembly is water cooled to dissipate heat produced by the sputtering process. The substrate to target distance is approximately 70 mm.

For insulating materials, such as the MgO used in this study, a dc bias would cause charge to build up on the surface of target, preventing a sustained plasma forming. To counter this a 13.56 MHz rf bias is applied. Charge built up on the surface is rejected during the positive half of the cycle and sputtering continues in the negative half. The particular frequency chosen causes electrons to circle in the plasma efficiently ionising further Ar atoms. In rf sputtering the plasma is not well contained near to the target due to the oscillating bias, growth rates are typically of the order 10 times slower than in dc sputtering at an equivalent power [179].

### 3.2.3 Tunnel junction deposition

**Substrate** Substrates were cut to size from a 4 inch Si (100) wafer. Si is chosen as a reasonably robust and cheap substrate. The wafer is 0.3 mm thick and cut by hand with a diamond tipped scribe. A 100 nm surface layer of oxidised Si ensures the substrate is more resistive than the electrode material, preventing current shunting. The substrate roughness was checked with AFM as less than 0.5 Å rms.

**Conducting electrode layers** The metallic underlayers are grown using dc sputtering. Typical deposition conditions are: base pressure $< 9 \times 10^{-6}$ Pa, Ar working gas pressure of 0.27 Pa (atom mean free path ∼10 mm), power controlled sputtering 25-50 W, deposition rates 1-4 Ås$^{-1}$. Sample wheel rotation speeds meant an approximate 20-30 s delay between layers. All growths were done at room temperature.

**Tunnel barrier** The MgO tunnel barrier was grown by rf sputtering, controlled by a Hüttinger power source. Prior to deposition the source was pre-sputtered for 45 min at 150 W, the barrier growth was done at 75 W and a working gas pressure of 1 Pa. Growth rates for MgO were around 0.1 Ås$^{-1}$ meaning a 5-10 Å barrier growth time of 50-100 s. A thin Mg layer (25 W dc, 0.5 s sputter time, nominal thickness 5 Å) is grown below the MgO to absorb excess oxygen and improve the barrier interface. This method is in keeping with previous studies at Leeds and other institutions into epitaxial MgO tunnel barrier growth [180].

### 3.2.4 Nanoparticle fabrication

There are few methods available to produce the pure, disperse nanoparticles necessary for this type of study. Some of these were discussed in section 1.3.1, they include surface self-assembly, e-beam lithography processing combined with shadow masking and co-sputtering with an insulating material to produce a granular matrix. There are limitations attached to each of these techniques, self-assembly can produce only a limited size range of densely packed particles, it also has constraints on materials that balance the surface mobility and surface energy tensions. EBL produces much larger particles and does not make 3D structures well. Co-sputtering produces a particle matrix without a well defined single particle current path. In Leeds we are lucky to have a gas-aggregation nanoparticle source integrated with our sputterer, this counteracts

many of the problems with other single particle techniques. In gas aggregation, the particles are pre-formed in-vacuum prior to deposition. This allows natural crystalline particle shapes to form and maintains purity of the particles. It also allows for downstream selection of size and deposition density.

### Cluster growth by gas aggregation

The gas aggregation technique for producing clusters was initially developed at the University of Leicester CM group [181]. The process starts with a standard dc sputtering source, a self perpetuating Ar plasma is created next to a target of high purity material to be grown. The metal vapour sputtered from the target passes up through the chamber of the gas aggregation source. The chamber is kept at a relatively high pressure of 80 Pa and cooled through water cooling pipes surrounding the sides. The pressure and temperature are such that the metal vapour saturates the atmosphere and nucleates to form nanoparticles. The gas is Ar with a small addition of He (approximately 2.5% by volume), it acts as both a working gas for the sputtering process and to create the correct conditions for particle nucleation.

The thermodynamics of particle formation in the chamber have been studied in detail by Quesnel et al. [182]. This is based on classical nucleation theory [183], which finds that saturation occurs when the chemical potential gain of particle formation exceeds the energy cost of forming the particle surface. The high pressure of the working gas in the chamber works as a thermal exchange, creating a decreasing temperature profile away from the sputter target. Metal vapour thermalisation occurs with a few mm of the target surface; particle formation occurs in a region further up the chamber where temperature is low enough for formation but high enough to accumulate collisions. The particle size distribution produced depends on the thermodynamic conditions, we are therefore able to alter it by changing the gas pressure, chamber length or growth power.

In Leeds we use a commercially available Oxford Applied Research gas aggregation nanoparticle source, this is pictured in Fig. 3.2 integrated into the SLIM sputtering system. A diagram of the device is shown in Fig. 3.3. The magnetron is at the bottom, with a manually adjustable chamber length from 300-450 mm. The aggregation chamber is pumped by a dedicated Pfeiffer turbo pump, necessary to protect the main chamber from the high pressures used for nanoparticle formation. A 10 mm aperture allows fully formed nanoparticles to pass through into the main sputtering chamber.

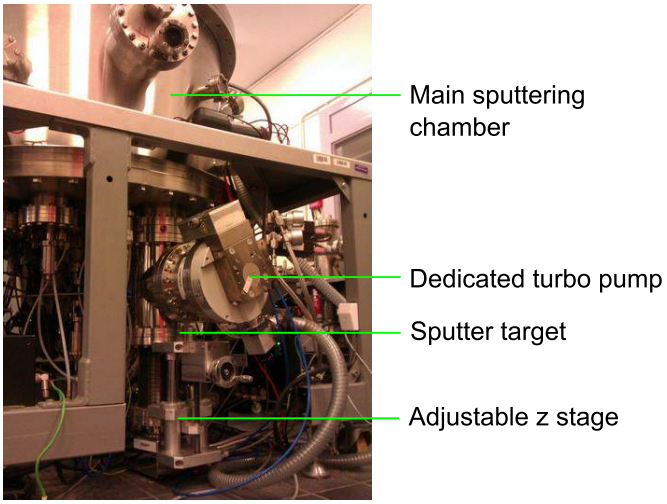


**Figure 3.2:** Photo of the gas aggregation source connected below SLIM. Major parts are labelled.

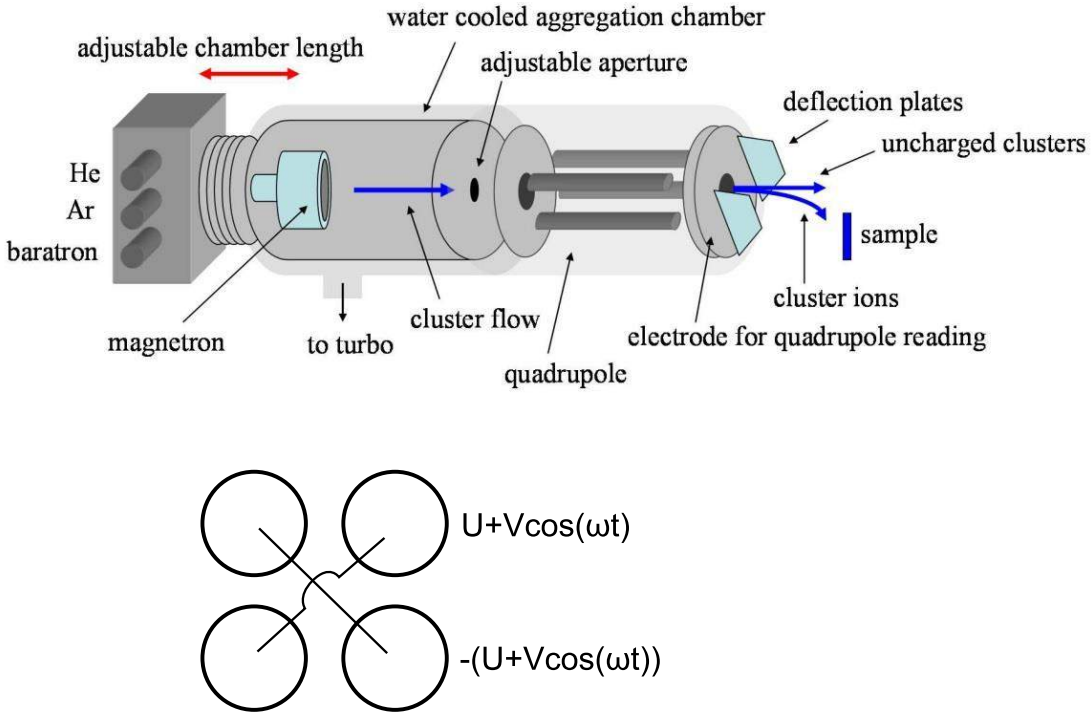


**Figure 3.3:** Diagram showing the operation of the gas aggregation source. Figure adapted from [184].

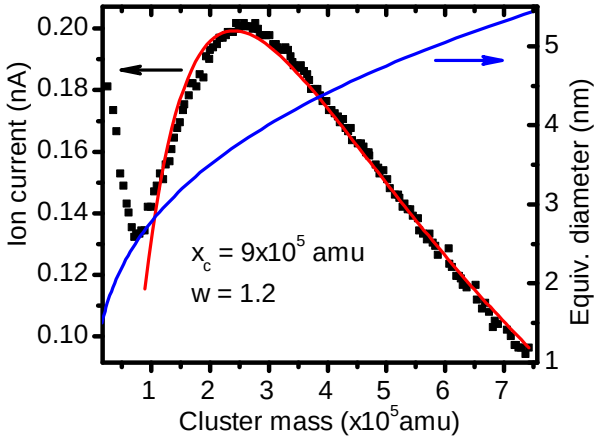


**Figure 3.4:** Black squares show a quadrupole particle mass scan for $Co_{30}Fe_{70}$ nanoparticles. The blue line shows a conversion factor between mass and equivalent radius assuming a spherical particle. The red line fit to the scan is a log-normal distribution.

### Particle beam control and deposition

Nanoparticles are size selected, post-formation, by an electric quadrupole field. The quadrupole selector consists of four parallel steel rods 22 cm long, aligned along the path of the NP beam. An ac voltage of variable frequency $f$ with a dc offset is applied to the rods $U + Vcos(2\pi ft)$. This is applied in anti-phase in opposing rod pairs as shown in the bottom of Fig. 3.3. This field is designed such that only charged particles within a certain range of masses will have a stable trajectory through the quadrupole rods. The motion is governed by the Mathieu equations, these have stable solutions for a cluster mass (amu) of $M = 7 \times 10^7 V/f^2 d^2$ and for a resolution of masses surrounding this of $\Delta M/M = 7.9(0.17 - U/V)$ ($d$ the diameter of the rods) [181; 185]. An electrically isolated plate at the end of the quadrupole collects a portion of the particles and measures the flux at this point as a current.

After the quadrupole a dc electric field is applied by $x$ and $y$ oriented deflection plates (see diagram). These guide the charged selected particles onto the sample. The sample is purposefully offset from the quadrupole axis to eliminate the neutral particle beam which has not been size selected. To detect the charged particles at the sample position, a home built Cu electrode fitted into a standard sample holder can be rotated into position. The electrode current is fed out to a Keithley picoammeter. $x$ and $y$ voltages are scanned between -100 and 100 V to detect the maximum flux point.

Because the particles are formed in thermodynamic equilibrium they have low kinetic energies ($< 0.1$ eV). Calculations show at this energy they gently deposit onto the sample surface with no damage to surface or particle [186], we will later confirm this with cross-sectional TEM. The density of particles on the surface is determined simply by the time the substrate is exposed to the particle beam. The flux rate is variable depending on the conditions but of the order 1 particle $\mu m^{-2}s^{-1}$, it is fine tuned before growth by the electrode current.

By varying $V$ the quadrupole allows a scan over all of the masses produced by the nanoparticle source. An example scan on $Co_{30}Fe_{70}$ nanoparticles is shown in Fig. 3.4 plotting detected current vs. particle mass, also plotted is the conversion from mass to particle diameter assuming a spherical shape. The resolution is set at 20%. As is common with this type of growth method, the mass probability fits to a log-normal distribution [187]. This has the formula

$$P(x) = \frac{1}{\sqrt{2\pi}wx} \exp\left(-\frac{[\ln(x/x_c)]^2}{2w^2}\right), \tag{3.1}$$

with a width represented by $w$ and peak centre $x_c$. The fit to the example scan is shown in red with parameters listed on the plot. Below approximately $1 \times 10^5$ amu a small secondary peak is seen. This is caused by high kinetic energy particles coming through at low applied voltages. This region is avoided when selecting a mass window because of the indefinite size. $w$ and $x_c$ are varied by controlling the deposition parameters (power, gas pressure, chamber length). Depending on the material $x_c$ is generally between 4-8 nm equivalent diameter.

Typical growth conditions for particles were 80 Pa aggregation chamber pressure, 4 Pa main chamber pressure, 50:1 Ar:He ratio, 20 W power controlled target sputtering (300 V), ≈4 min growth time for a particle density of a few hundred $\mu m^{-2}$. The particle sizes were checked after growth using atomic force microscopy (AFM), an example scan is shown in Fig. 3.5. In general the non-magnetic particles were accurately size selected. Magnetic particles were much more difficult to grow, the target magnetic field affects the plasma formation and ignition is difficult, this limits possible variation on the growth conditions. Size selection was also more difficult for the magnetic particles, the quadrupole selector is less accurate with magnetic material. Magnetic nanoparticles were always checked for size and density after growth using AFM.

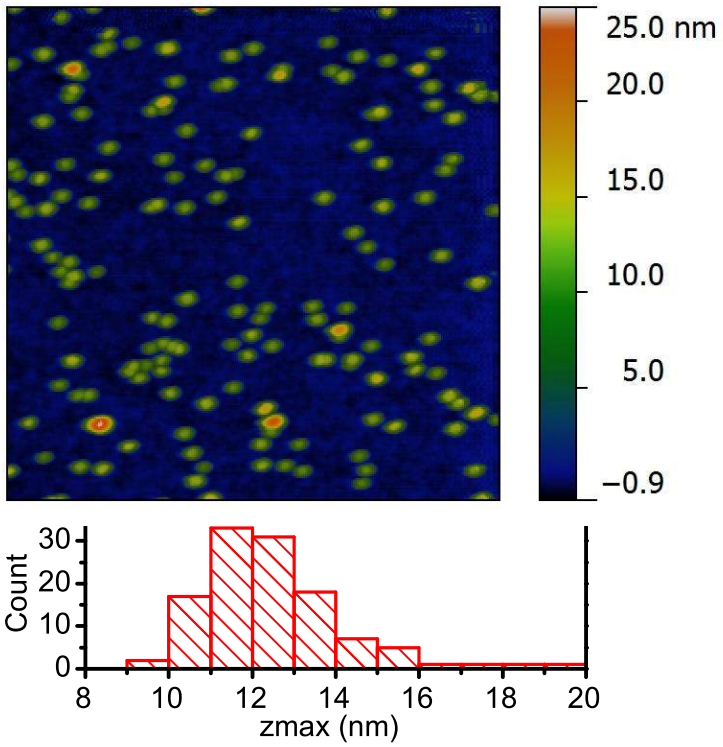


**Figure 3.5:** AFM $1 \times 1$ μm image of $Co_{30}Fe_{70}$ nanoparticles, used for calibration. The histogram below is of height of the nanoparticles. This gives the distribution of diameters centred about 12 nm.

## 3.3 Growth characterisation

### 3.3.1 X-ray reflectivity

X-ray reflectivity (XRR) was used to calibrate sputtered film thicknesses. A source of collimated x-rays is shone onto a film in the reflection or specular geometry. Interference between top and bottom film interface reflections produces a pattern known as Kiessig fringes. The angular separation of the fringes determines the thickness of the film. For small angles the angle $\theta_n$ of the $n^{\text{th}}$ fringe peak is given by

$$n\lambda = 2t(\theta_n^2 - \theta_c^2)^{1/2} \tag{3.2}$$

where $\lambda$ is the x-ray wavelength, $t$ is the film thickness and $\theta_c$ is the angle for total internal reflection [188]. For optimum fringe density and accurate thickness determination an approximately 350 Å thick film is grown directly onto a substrate, an example reflectivity pattern from an MgO film is shown in Fig. 3.6. For films with poor electron density contrast with the substrate, a thin layer of a heavy metal such as Tungsten at the interface adds the required contrast while introducing little error into the film thickness. Film roughness can be determined from full reflectivity fitting to the Parrat formalism [189]. The system used in Leeds is a Bruker D8 discover, the x-ray beam is produced from a Cu anode and then collimated via slits and passed through a monochromator tuned to the Cu K$\alpha$ 1.54 Å wavelength. The filtered beam passes finally to a scintillator detector and data logger.

### 3.3.2 Transmission electron microscopy

In transmission electron microscopy (TEM), a high energy (100-200 keV) electron beam is used to image materials in atomic level detail. TEM is an invaluable tool for condensed matter physics, used for studying sample composition, interface quality and epitaxial crystal alignment to name a few [190]. The basic geometry of the TEM is shown in Fig. 3.7. Much like the optical microscope it consists of a series of lenses and apertures used to focus and magnify the electron beam through the sample and onto an image plane. In order to be transparent to electrons the samples need to be $\lesssim$ 100 nm thick. The lenses used are not glass but electromagnets of various designs. The lens focal length is easily adjustable through the electromagnet currents.

At the top, the electron beam is produced from a field emission gun. The beam is then focussed with a system of lenses known as the condenser, to form a collimated

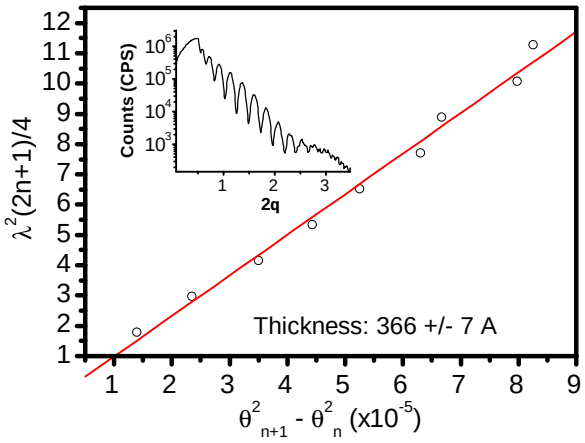


**Figure 3.6:** Example x-ray reflectivity scan on an MgO sample. MgO is dusted top and bottom with 5 Å of Ta to enhance surface reflections. Keissig peak fit shows a film thickness of $366 \pm 7$ Å

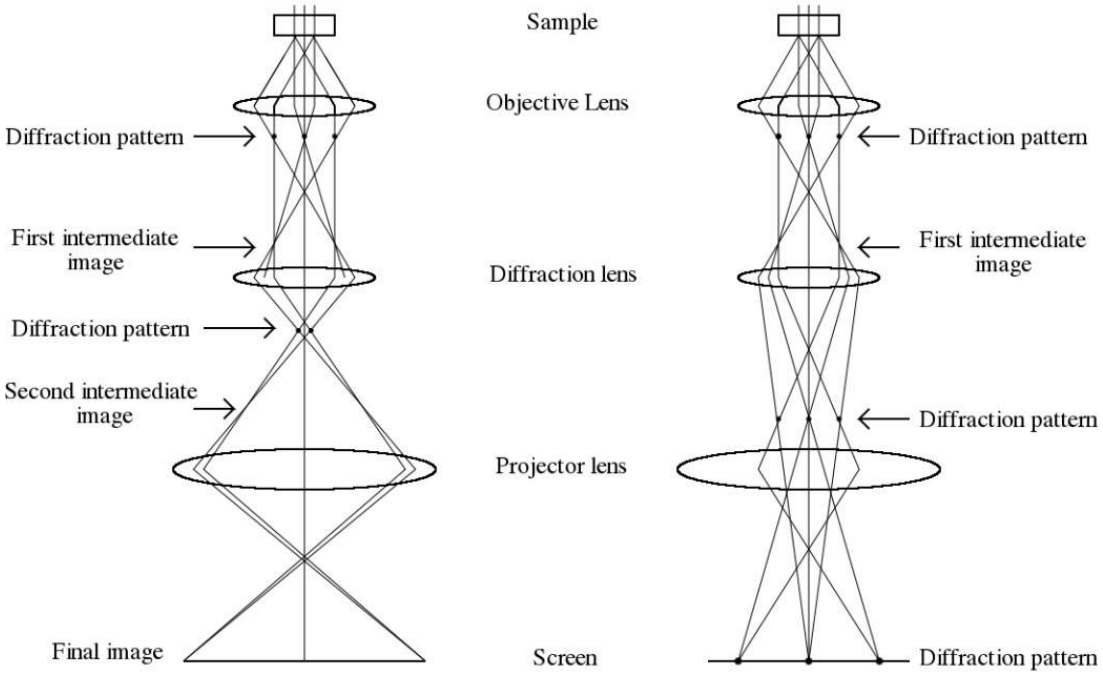


**Figure 3.7:** Ray diagrams for two TEM setups. Left the lenses are set such that the image plane is given, right the diffraction pattern is collected. Diagram adapted from [190]

.

beam illuminating the sample. Some electrons pass straight through while others are scattered by the sample atoms. The transmitted and scattered electrons are all collected by the objective lens and passed through a diffraction and projection lens to form a final image. The image is collected by a fluorescence screen or CCD camera. By adjusting the lens strength, the final image can be either real space or a diffraction pattern.

The resolution of an ideal microscope is limited to roughly the wavelength of the radiation. 100 keV electrons have a de Broglie wavelength $\lambda \approx 0.01$ Å, far smaller than an atom. The resolution of the TEM microscope used was approximately 1 Å however, it is ultimately limited by the aberrations caused by imperfect lenses.

The high resolution planar TEM images and data for this thesis were taken using a FEI Tecnai system operating at 200 keV with the assistance of Dr. Michael Ward. For TEM the samples are required to be just a few nm thick to allow transmission; films and nanoparticles were grown on to commercially produced holey carbon membranes, 30 nm thick. The carbon is amorphous so does not interfere with diffraction effects.

For the cross-sectional TEM images the films/nanoparticles were grown onto a standard Si substrate. This then underwent a standard cross-sectioning procedure undertaken by Mr. Mathew Mclaren, this is illustrated in Fig. 3.8. The sample is first cut up and glued back-to-back using an organic resin and hardening agent. The stack is bored with a disk punch to form a cylinder, with the interface of interest down the axis. A thin slice of this is taken and a dimple grinder is used to thin the middle of the sample to approximately 10 μm thick. The final thinning to form a small hole in the middle is undertaken by precision ion milling. The smooth edges of the hole are thin enough to be suitable for TEM studies. Example in-plane and cross-sectional TEM images are shown in Fig. 3.9 (a) and (b) respectively.

## 3.4 Magnetometry

### 3.4.1 XAS and XMCD

The physical basis for the XAS and XMCD experiments are detailed in section 2.5. The experiments were carried out on the U4B beamline at the NSLS source, Brookhaven National Laboratory (synchrotron now decommissioned). The x-rays are generated from a bending magnet source with an energy range 20-1200 eV. All measurements were done in the total electron yield geometry, the pA drain current from the sample

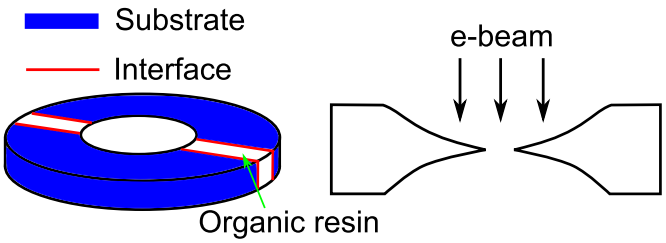


**Figure 3.8:** Diagram illustrating the cross-sectioning process for TEM. Substrates are cut to form a substrate/interface sandwich, glued with a resin and hardening agent. A dimple grinder and ion miller is then used to bore a small central hole. The edges of the hole are thin enough that TEM can be used to look at the interface, see cross-section of disk on the right.

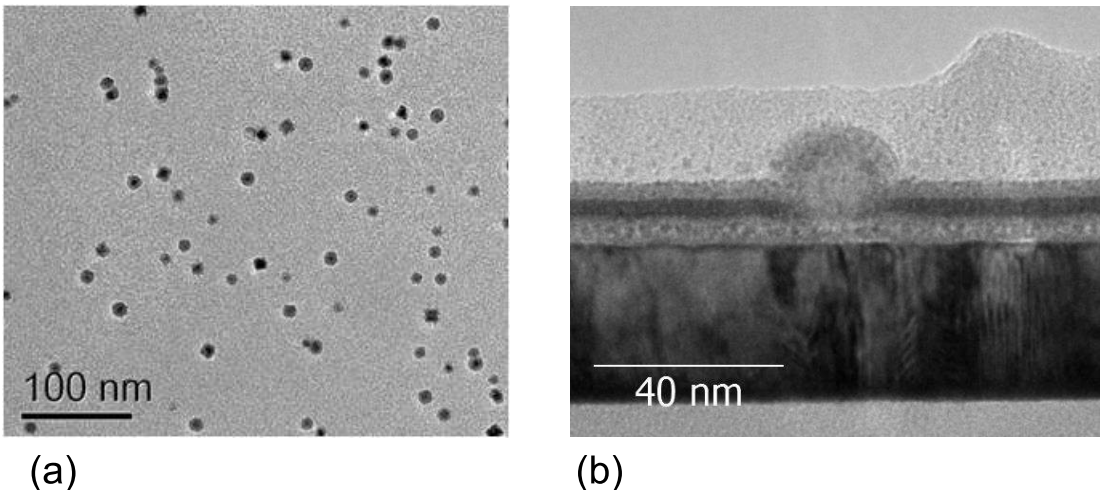


**Figure 3.9:** TEM images of nanoparticles in relief (a) and cross-section (b).

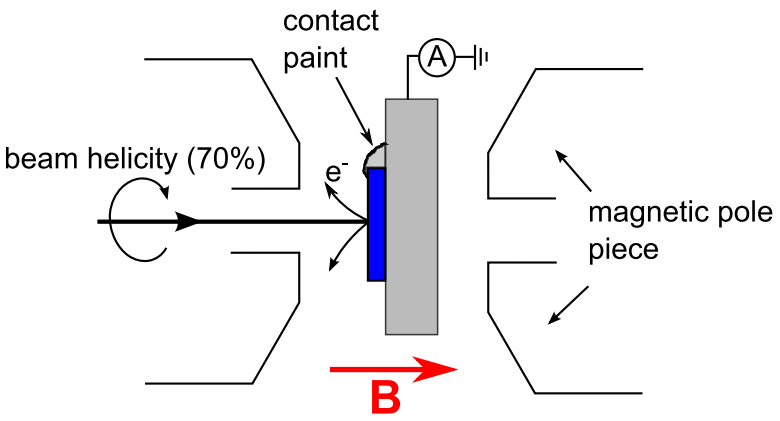


**Figure 3.10:** Geometry used for XMCD measurements at U4B. Sample is perpendicular to the beam and electrically connected through the sample stick to a current-to-voltage amplifier. Electromagnetic pole pieces front and back of the sample have a central hole bored to allow beam through.

is measured via a current to voltage amplifier. Current is drained from the sample via a small daub of silver paste out of the beam area. The incoming beam energy is scanned via a monochromator and resulting electron emission intensity plotted. The TEY signal is continuously normalised to a Au grid beam monitor to account for beam intensity variation. A known magnetite reference sample is continuously scanned with portion of the beam intensity, allowing later adjustment for systematic monochromator errors. The beam width at the sample is approximately 1 mm.

For the XAS measurement linearly polarised light is used, with an energy resolution of better than 0.1 eV at the Fe $L_3$ edge. For the XMCD measurements 70% circularly polarised radiation was used. The sample was perpendicular to the beam in the geometry shown in Fig. 3.10, electromagnetic pole pieces front and back have a hole bored through them to allow beam through. At each energy the sample magnetisation was set anti-parallel/parallel with the beam direction using a field of $\pm 0.5$ T, TEY signal measured in both directions.

### 3.4.2 SQUID Vibrating Sample Magnetometer (VSM)

The SQUID VSM is an extremely sensitive instrument, able to measure the total magnetic moment of a sample down to $1 \times 10^{-11}$ $Am^2$. Commonly the instrument allows investigation of the sample magnetism over a range of temperatures and applied fields.

The VSM principle was first developed by Foner 1955 [191]. The sample to be measured is placed within a counter-wound wire coil and vibrated along the axis sinusoidally. The motion causes the small magnetic field from the sample moment to generate an emf in the wire coils. The emf can be measured and is proportional to the sample moment, it is not affected by external time-independent fields. Extremely high levels of noise reduction are achieved by using a lock-in amplifier tuned to the frequency of the sample vibration. The lock-in accepts signal only within a very narrow frequency band around the motion, eliminating noise sources at all other frequencies.

The SQUID VSM uses a superconducting quantum interference device (SQUID) to measure the generated signal even more accurately. A diagram of the operation is shown in Fig. 3.11. A SQUID uses the properties of superconductors to measure magnetic flux down to accuracies greater than a single magnetic flux quantum. The current generated in the VSM coils is inductively coupled to the SQUID which acts as an extremely high gain and low noise current to voltage converter. At Leeds we used a Quantum Design MPMS SQUID VSM system, this has a standard temperature range of 2-400 K and can apply fields up to $\pm 4$ T, it also has an oven mode which extends the temperature range from 400 up to 900 K. The samples were $3 \times 3$ mm substrates, which are mounted on low susceptibility quartz rods and lowered into a $^4$He cryostat. The sample space sits in a bath of liquid He, surrounded by an insulating jacket of liquid nitrogen at 77 K. A roughing pump is used to pull He through a vent into the sample space at a controlled rate, this is combined with a resistive heater to control the sample temperature to within 30 mK. Pumped $^4$He is recycled at Leeds through an onsite liquefier. The applied magnetic field is created by a He cooled superconducting magnet. For lock-in the sample is vibrated at 13 Hz with an amplitude of $\approx 5$ mm. Amplitude and averaging time combine to affect the sensitivity of the measurement, these parameters were adjusted as needed. The sample total moment was calibrated with a $3 \times 3$ mm NiFe fim of known thickness and density.

## 3.5 Scanning probe microscopy

Scanning probe microscopy (SPM) is a group of very powerful techniques for obtaining real space high resolution images of surfaces. In general a sharp probe is raster scanned very close to a surface. Sensitive feedback of the surface physical properties is achieved through force, tunnelling current or other interaction mechanism. SPM

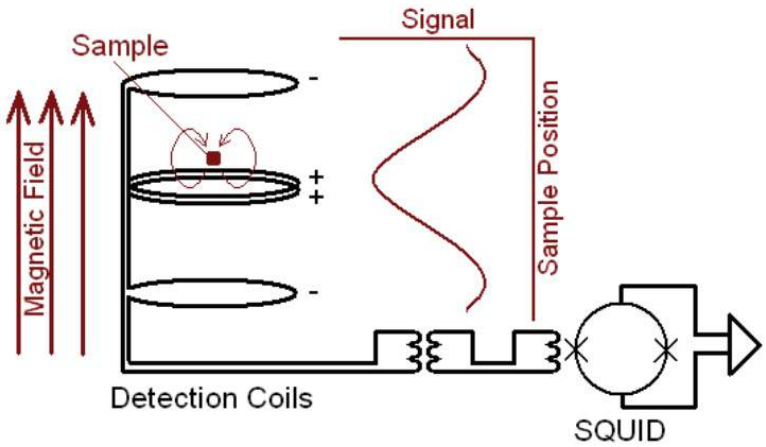


**Figure 3.11:** Simplified diagram showing the operation of the SQUID VSM. The signal generated in the coils is inductively coupled to a SQUID device designed as a highly sensitive current to voltage converter. Diagram adapted from [192].

requires atomically precise positioning, piezo actuators allow this control. The quality of measurement is generally determined by the limiting factors of environmental noise and the quality of the probes [193].

### 3.5.1 Atomic force microscopy (AFM)

In AFM the feedback mechanism is simply the interaction force between the surface and the tip. Close to the surface this is an attractive van der Waals force, this slowly increases towards the surface and is followed by a sharp Coulomb repulsion. AFM was first attempted in the 1980s using STM to detect cantilever deflection [194]. There have since been huge developments in accuracy, reliability and ease of use. High quality images can now be obtained in minutes in atmospheric conditions or even in liquids, it is used as a standard tool in many disciplines of science [195; 196]. There are many different types of AFM, all designed to measure particular physical properties or deal with particular types of materials. In this research we use 'tapping mode' AFM, a common mode with a reduced contact with surface and therefore less chance of surface damage. The AFM is used for calibrating particle sizes and densities, also for examining film roughness and morphology.

The basic geometry of the tapping mode AFM measurement is shown in Fig. 3.12. The scanning probe is a sharp tip attached to a perpendicular cantilever. This cantilever

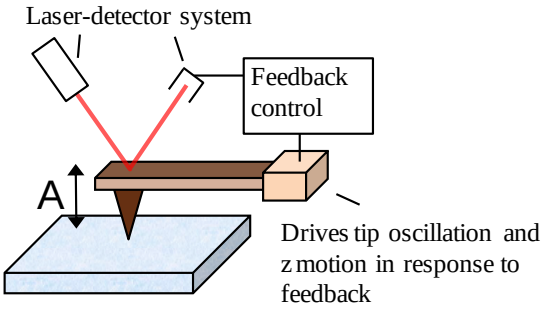


**Figure 3.12:** Diagram showing the major components of the AFM system.

undergoes forced oscillations close to its resonance frequency, driven by a piezo actuator at its base. The interaction with the surface is detected sensitively through alterations to the amplitude of vibrations. The additional, height dependent, attractive force on the tip will change the effective resonance frequency and introduce damping effects, both of which modify the cantilever rms amplitude [197]. To detect tip deflections a laser reflected off the tip end is detected in a four quadrant photodiode. Differences between the segment signals are used to detect the relative cantilever deflection.

The deflection signal is immediately fed back to a computer which continuously adjusts the tip height to maintain a constant distance from the surface, i.e. a constant RMS amplitude. A key parameter to control for a quality image is the sensitivity of the feedback loop, particularly for nanoparticle samples with abrupt large height changes. The loop is managed by a proportional integral derivative (PID) gain controller. PID measures as an error $e(t)$, the difference between the current and the desired RMS amplitude, and adjusts tip height at a rate according to:

$$u(t) = c_p e(t) + c_i \int_0^t e(\tau)d\tau + c_d \frac{\mathrm{d}}{\mathrm{d}t} e(t) \tag{3.3}$$

where $c_p$, $c_i$ and $c_d$ are constants set by the user to control the feedback rate. $c_i$ tends to be the most responsive of these constants and was set at a relatively high value for these samples.

AFM scans between 0-10 µm were done in atmospheric conditions on a Bruker multimode 8 with electronics controlled by Nanoscope 5 technology. The tips were silicon Bruker TESP probes or similar: resonant frequency ≈ 300 kHz and force constant 42 $\mathrm{Nm}^{-1}$, nominal tip radius 8 nm.

### 3.5.2 Scanning tunnelling microscopy (STM)

In STM, a conducting probe interacts with a surface via a tunnelling current. This was the original SPM technique developed by Binnig and Rohrer in the early 1980s, work for which they were shortly awarded the Nobel prize [136; 198]. Due to the exponential sensitivity of the tunnelling current, the STM remains one of highest resolution SPM techniques, atomic resolution is regularly achieved on conducting surfaces. Laterally 0.1 Å and vertically 0.01 Å resolution is possible [193].

The tunnelling process was explained in detail in section 2.1. The resulting current profile was found as (2.13)

$$I(V) \propto D_{\mathrm{T}}(\mathbf{r}_0, E) D_{\mathrm{S}}(E_{\mathrm{F}}) V \mathrm{e}^{-2\kappa z}. \tag{3.4}$$

This shows the tunnelling current as proportional to the tip and sample density of states, $D_{\mathrm{T}}$ and $D_{\mathrm{S}}$ respectively. The current decays exponentially with tip surface-distance z on a length scale $\kappa \propto \bar{\varphi}^{1/2}$ with $\bar{\varphi}$ the average barrier height. An STM image is inherently more complicated than an AFM image to interpret, an image convolutes both the topology of a sample and the surface electron density, simulation and theory is often needed to extract quantitative information.

An Omicron variable temperature STM (VTSTM) was used for STM measurements. This is an ion pumped UHV system with a base pressure $\approx 10^{-9}$ Pa. Using a liquid $^4$He circulation system, sample temperature can be controlled to a base temperature of 20 K. A diagram of the measurement set-up is shown in Fig. 3.13. The sample is clamped into a molybdenum sample holder which rests on a grounded contact finger. A brass thermal contact plate is clamped to the sample plate in situ to stabilise the sample temperature. Flexible Cu braiding provides thermal conduction from the cooling circulation to the brass plate. During scanning the sample is grounded and bias voltage applied through the tip.

The tip is a snipped or etched wire pointing up to the sample, it is mechanically clamped into standard 3 pin holder. The tip position is controlled on a coarse scale with a 3-axes linear piezo motor and with a single tube piezo for fine approach and scanning. Positive voltage is applied to the tip, gap voltages range from ±0-10 V. Current signal is amplified with preamplifier, signals in the pA to nA range are measured. Tip feedback is managed by a proportional integral (PI) gain system, the software allows user control over the sensitivity with a single parameter (selectable from 0-100%).

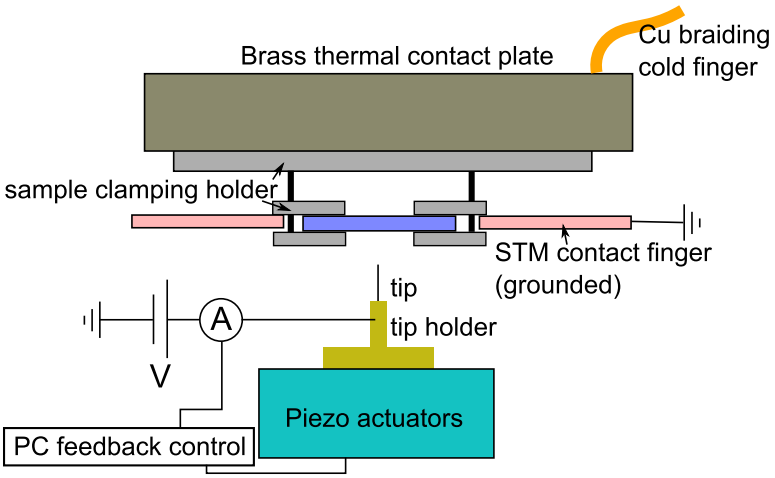


**Figure 3.13:** Diagram of the tip-sample assembly within the VTSTM vacuum chamber.

Several systems are used for vibration and electrical noise reduction. The entire sample-tip assembly is mounted on free floating soft springs with a resonance frequency approximately 2 Hz, this stage is eddy current damped. The STM vacuum chamber and pump are all mounted on an air cushioned optical table, only flexible connections are allowed between table and ground. All electrical connections in the room, and the chamber body, are earthed through a single ground point to prevent grounding circuits.

**Sample transfer** STM is a surface science technique requiring high quality surfaces. To protect the exposed oxide and nanoparticles from oxidation and other atmospheric contamination, the samples were transferred between sputterer and STM using a small portable vacuum chamber. This is pictured in Fig. 3.14. The portable 'vacuum suitcase' has a small dedicated ion pump run by two 12 V dc batteries, it maintains a vacuum of $\sim 1 \times 10^{-6}$ Pa throughout travel and transfer. Connection is through a CF standard flange with Cu gasket, pumping is done via the fast entry lock turbo pump on the STM.

**Scanning tunneling spectroscopy (STS)** I-V STS measurements were done with the feedback loop off and the tip nominally stationary (unless otherwise stated). Each point required 50 µs stablisation time and 160 µs for data aquisition. The average time for a single spectra then was $\approx 60$ ms.


**Figure 3.14:** Photos showing the operation of the vacuum suitcase. (a) transfer out of SLIM. (b) transfer through the fast entry port of the STM.

### 3.5.3 Probe developments

In any SPM experiment, the feedback mechanism is a convolution of the sample properties and the probe itself. It is therefore very important to choose the correct tip material and shape. In STM there is the topographical convolution of the tip shape with the surface features and there is also the electronic convolution, the tunnelling is proportional to the joint density of states. The STM tip then should be chemically stable, have a small reliable end shape and a relatively featureless density of states about the Fermi energy. There are two main classes of tip preparation used: mechanical cutting of an inert metal or chemical etching of an appropriate material. Cutting is easier and can produce sharp tips, however the end shape is unreliable in nature, the tip quality is generally inconsistent and unsuitable for spectroscopy. Investigations at the beginning of the project showed that cut tips often produced image artefacts, the convolution of the shape with the relatively large nanoparticles is severe. We therefore decided to develop the more difficult chemical etching method which produces much more reliable, and quantifiable, tip shapes.

#### Mechanical cutting

Tips were cut from $Pt_{80}Ir_{20}$ 0.25 mm wire using standard wire cutters. The cut was made at a steep angle to the wire and with a concurrent pulling motion, this is a very standard method of tip production [199]. PtIr is chemically inert so that the wire is simply cut in air, clamped into the tip holder and loaded into the STM vacuum

chamber. The tips were quality controlled by scanning terraces on freshly cleaved HOPG (highly oriented pyrolytic graphite), this is a standard control material in STM that is relatively easy to scan for atomic scale detail [193]. Cutting produced atomically sharp tips approximately ∼20% of the time.

Fig. 3.15(a) shows examples of two different tips cut and then imaged with scanning electron microscopy (SEM), clearly the shape of the end of the tip can be seen to vary hugely from tip to tip. The sensitivity of the tunnelling means that 90% of the current goes to the first 1 Å of the tip material, so for flat surfaces like HOPG the unreliable shape is not usually a problem. For relatively large nanoparticles ideally the last few nm of the tip would be smooth. A rough tip also means that it is difficult to measure a single particle in spectroscopy scans, the capacitive effects of nearby clusters reduces as $1/R$ and can be quite long range.

### Chemical etching

Etching of tungsten probes was done in a two stage process. First a sharp tip was produced *ex situ* using a chemical etching process, this forms an oxide layer which must be removed once in vacuum. In the STM chamber the oxide layer was removed by electron bombardment and field emission. An SEM image of a W tip produced in this way is shown in Fig. 3.15(b), the end is smooth and conical with a radius generally around 30 nm. Tungsten is chosen as a well characterised common tip material. The DOS is relatively smooth about the Fermi energy [200; 201].

Chemical etching was done using standard production method for tungsten tips [199; 202]. Briefly 0.25 mm diameter tungsten wire is cut to length and then dipped 2 mm into 4 M NaOH solution. Using a stainless steel ring as a second electrode, an electrochemical cell is formed with etching taking place preferentially at the liquid surface. After approximately 5 mins etching, the wire at the surface will be too thin to support the length below it and will stretch and drop leaving a sharp point to use as a tip. The voltage is immediately cut off at this point to prevent further etching of the tip. This process had already been established at Leeds during the doctorates of Dr. C. Allen and Dr A. Walton [203] and required no further development.

For the second stage a new adjustable sample holder was installed through a port into the STM. The new sample stage is electrically isolated from the chamber and connected to an electronic feedthrough capable of supplying a voltage to the tip. A

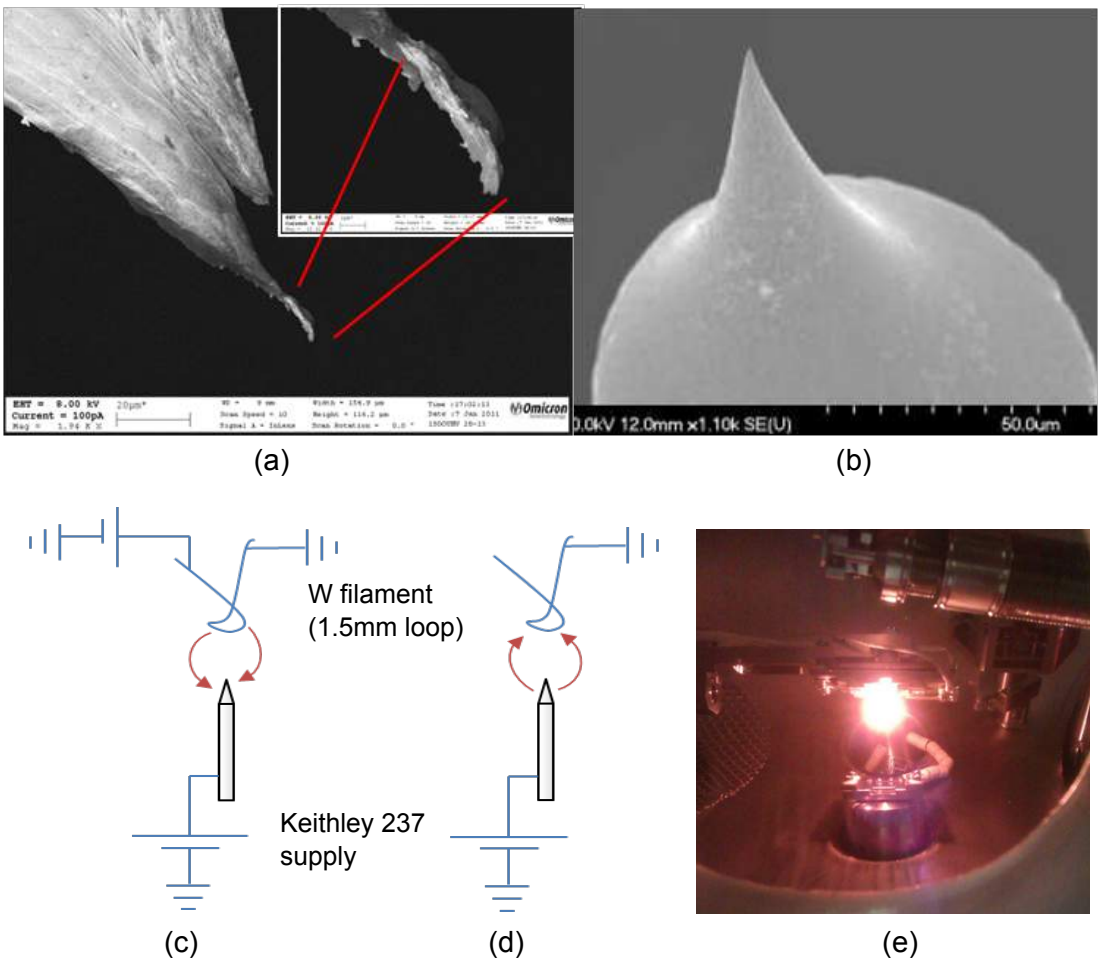


**Figure 3.15:** (a) and (b) show an SEM comparison between a PtIr tip and W tip. (c) is a diagram showing the electron bombardment stage of tip treatment and (d) a diagram showing the field emission stage. (e) shows the completed tip tool in situ, the bright glow comes from the heated W filament.

looped tungsten filament of diameter ≈1 mm is placed close to the tip, see Fig. 3.15(c). A current of approximately 4 A is forced to flow through the filament causing it to heat up and thermionically emit electrons, at the same time +100 V is applied to the tip causing it to attract the emitted electrons which bombard the tip and etch away the oxide layer. To characterise the tip the filament is grounded and the tip voltage is scanned between 0 and -1 kV (while limiting the current to 1 μA), a diagram of this is shown in Fig. 3.15(d). The current-voltage curve produced by the electron field emission is characteristic of the tip shape and can be used to find a tip radius. Tip radii of 10-40 nm were considered acceptable for use.

A picture of the tip tool inside the STM is shown in Fig. 3.15(e) the filament is removable, wire bonded to a standard Omicron sample plate and the voltage across it is controlled by the inbuilt Omicron sample heating power supply. The tip holder is designed to accommodate standard omicron sample plates and moves back and forth on a $z$ manipulator to allow room in the chamber. It is isolated electrically by ceramic beads and connected to a Keithley 237 power supply capable of supplying up to ±1.1 kV and measuring currents down to 100 pA. The Keithley 237 is controlled via a GPIB connection by a computer; a program with a graphical user interface has been designed and implemented for this purpose.

# Chapter 4

Ensemble magnetic properties of CoFe nanoparticles

## 4.1 Introduction

This chapter describes an investigation into the ensemble magnetic properties of $Co_{30}Fe_{70}$ nanoparticles. As discussed in chapter 2, nanoscale ferromagnets display a rich array of magnetic behaviour not seen in bulk material, the basic physics behind these phenomena are well explained but there are still open questions, particularly regarding densely packed interacting particles. One of the methods that has been most successful to investigate these properties in recent years, has been to use a gas aggregation nanoparticle source, or similar, to deposit clean, size-controlled nanoparticles in a known concentration [187]. As this is what we used for deposition anyway this put us in a good position to conduct these studies.

Here we will mainly focus on a set of samples grown with relatively high density of clusters per unit area. These were characterised first using X-ray magnetic circular dichroism (XMCD) at the National Synchrotron Light Source (NSLS) at Brookhaven National Laboratory, and then underwent further investigation in Leeds using magnetometry (SQUID-VSM) and atomic force microscopy (AFM). In part, the high cluster density (several 1000 $\mu m^{-2}$) was necessary in order to generate enough signal for the XMCD. In fact, as we will see, studying clusters at percolation ended up producing interesting effects related to nanoparticle magnetic dipole interaction forces. XMCD is element specific and can separate out orbital and spin angular momentum contributions to magnetism. We show the orbital component in nanoparticles is enhanced over the quenched bulk value and further, that it is correlated with the size of the particle.

## 4.2 Samples

The samples were grown on a thermally oxidised silicon wafer. In each sample, the stack grown was substrate/Ta(4 nm)/MgO(1.1 nm)/$Co_{30}Fe_{70}$ NPs/Al(3.7 nm). This stack was chosen to be similar to the samples to be measured with STM, as described later in chapter 6. In particular, the MgO layer next to the particles will later be used as a tunnel barrier and for now it was important to see if it would affect the magnetic or chemical properties of the particles. The Al layer is a necessary cap for these samples which are removed from vacuum for transport: the surface atoms absorb atmospheric oxygen forming $AlO_x$ but this process passivates at a depth of about 2 nm [204], well clear of the nanoparticles (NPs). Due to its low atomic number Al also has a low

photon absorption in the VUV range, (an electron sampling depth of approximately 8 nm [205]) thus the XAS signal is not attenuated significantly by the capping layer.

The NPs were grown by gas-aggregation technique as described in chapter 3. Various sizes and densities were deposited according to the quadrupole mass filter settings and deposition times. However, in practise these size selections were not reliable for magnetic particles at this time. In the end the size distributions are taken from the more direct magnetometry and AFM characterisation post-growth. These data are presented below. In this study the samples grown were labelled according to the date grown and the sample within that run e.g. 1_010812. Since we do not know the expected properties of the sample until direct characterisation, we will use sample codes as effective indices until that point.

## 4.3 XAS characterisation

After growth and capping in vacuum, the samples were removed and taken to the NSLS facility for further characterisation. On the beamline the samples were mounted perpendicularly to the beam and electrically connected to the drain current pico-ammeter using silver paint. They were measured exclusively in total electron yield (TEY) mode as described in the methods chapter.

The first scans were used for x-ray absorption spectroscopy (XAS), these are quick scans of the monochromator using unpolarised photons and with no magnetic field applied to the sample. Fig. 4.1 (a) shows the signal obtained at the Fe L edge for sample 2_010812. The peaks are smooth with little visible fine structure, this indicates the clusters have been fully protected by the Al cap and have not oxidised. Fe-O bonds would cause secondary peak structure, an example XAS scan on an oxidised sample is shown in Fig. 2.6. This also means the MgO layer below has not intermixed with the clusters. The samples measured in this study all had the same Al cap and all showed the same lack of fine structure in their XAS spectra.

Fig. 4.1 (b) shows a scan of a sample at the Co edge. This has a considerably lower signal-to-noise ratio. The small signal is partly due to the 3:7 ratio of Co to Fe in the sample but also because this technique is generally less sensitive to the Co edge than the Fe edge [206]. The XAS spectrum shows no fine structure within the limits of the measurement however, again demonstrating the effectiveness of the cap. The signal is too low to be useful for the much less sensitive XMCD measurements, requiring too

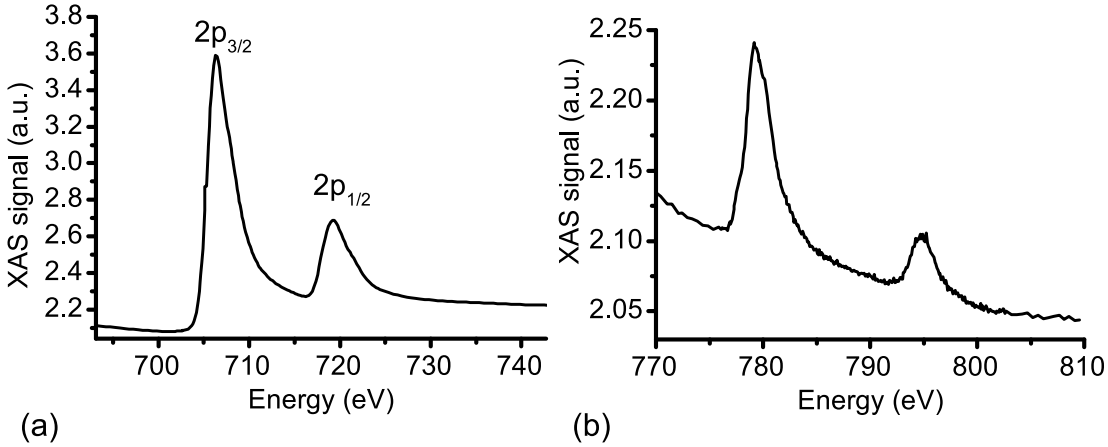


**Figure 4.1:** (a) XAS spectrum at the Fe edge from sample 2_010812 (in TEY mode). The peaks are smooth with no fine structure, this indicates that the iron is in a chemically pure unoxidised state (see text). (b) an example Co XAS spectrum, the signal is significantly noisier than at the Fe edge, though again no fine structure is visible.

long of a count time to obtain enough signal. XMCD measurements were all done at the Fe edge for these samples.

## 4.4 Size dependence of spin and orbital moments using XMCD

### 4.4.1 XMCD analysis

The samples were next measured for x-ray magnetic circular dichroism (XMCD) effects. In this geometry, the polarisation of the beam was fixed at 70% left circularly polarised, and the sample magnetisation was aligned parallel to the beam using a 0.5 T field generated with an electromagnet (this is close to the saturation field, see SQUID data later). At each monochromator setting, the TEY signal was measured with the sample magnetisation saturated along and against the beam. An example XMCD spectrum taken from sample 2_010812 is shown in Fig. 4.2, the top graph shows the intensity TEY signal. The signal is good: clear differences can be seen at the $L_3$ and $L_2$ edges and the polarised measurements switch in the opposite directions ($I^+$ is greater at the $L_3$ edge by convention).

The TEY data shown in Fig. 4.2 has been normalised to the post-edge background

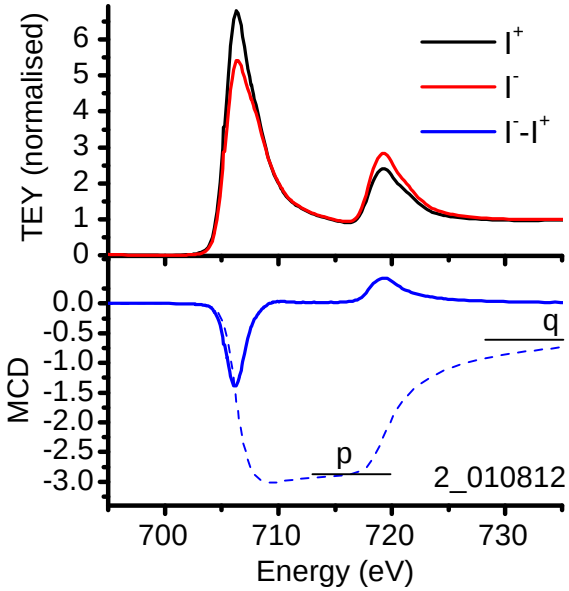


**Figure 4.2:** Showing a sample intensity and difference XMCD spectrum from sample 2_010812. The large MCD signal from the densely packed clusters enables an accurate determination of the $m_{orb}/m_{spin}$ ratio. $p$ and $q$ as used in the sum rules are labelled on the integrated MCD data (dashed line). As with XAS data, a linear background is subtracted and then normalised to the post-edge signal.

signal, which is necessary in order to apply the sum rules. First a linear background is subtracted to bring the pre-edge background to zero, then the total signal is multiplied by a factor to bring the post-edge background signal to 1. The difference (MCD) signal is shown in the lower panel, this is smooth and low noise after approximately 45 min of count time. Previous measurements had shown that this density of nanoparticles was required in order to obtain a signal good enough to apply the sum rules within a reasonable count time. The dashed line shows the integration of the MCD signal with $p$ and $q$ marked as used in the sum rules. For error analysis purposes, the error in $p$ was taken as the variation in the integration signal over the $\sim 3$ eV around the end of the $L_3$ edge. The error in $q$ was taken as the noise in the final background signal (the end background has been cropped out of the graph but did level to below the noise threshold by 750 eV).

The most accurate information that can be obtained from XMCD spectra is generally the ratio of the orbit to spin moment per atom ($m_l/m_s = r_{ls}$) for the element

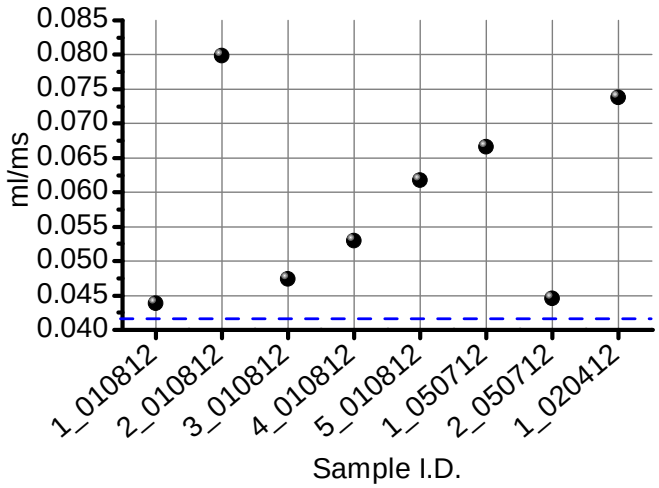


**Figure 4.3:** $m_l/m_s$ values determined for each sample. The blue dashed line marks the bulk value for iron.

in question. Recalling the sum rule equations (2.33) and (2.34) in chapter 2 both $m_l$ and $m_s$ contain a factor $1/C$ where $C = \langle I_{L_3+L_2} \rangle / N_h$ i.e it is the integration over the intensity TEY signal (after the non-resonant background signal is subtracted) divided by the number of hole states in the 3d band. $C$ tends to be the least accurately determined quantity because of the generally unknown $N_h$, it is cancelled out in $r_{ls}$. In the $p$ and $q$ notation we can write

$$r_{ls} = m_l/m_s = \frac{2q}{3(3p - 2q)}. \tag{4.1}$$

The spin to orbit moment ratio is shown for each of the samples in Fig. 4.3. A blue dashed line at the bottom indicates the well established $r_{ls}$ ratio for bulk Fe of 0.042 [173]. These measured ratios are enhanced over the bulk value, though not close to the single atom limit, indicated by Hund's rules to be close to 1 [207]. There is no correlation between the nominal size of each sample, as set by the quadrupole during growth, and the level of enhancement in $r_{ls}$. Unfortunately at this time (and in general with magnetic targets), the quadrupole was quite inaccurate in producing a well defined size of clusters (this is discussed further in the experimental techniques chapter). It was desirable therefore to get an accurate measurement of the size from an alternative physical measurement, each sample was therefore later scanned using AFM.

### 4.4.2 Size determination by AFM

Atomic force microscopy (AFM) used in tapping mode (low tip-sample interaction) was done on each of the samples. The tips used were nanosensors PPP-NCLRs, Al coated Si with a nominal tip radius <10 nm. The scans were taken on the same place on the sample as the beam placement for the x-ray spectroscopy data (the x-ray beam was approx 500 μm width). A 1.5 μm image taken on sample 1_050712 is shown in Fig. 4.4 (a) with a zoomed portion shown in (b). The clusters are densely packed, 970 are countable giving a cluster density of 130 $\mu m^{-2}$. In fact as we will see later using magnetometry measurements the clusters are far denser than this, measuring a few 1000 $\mu m^{-1}$, not all of the particles are visible.

On first glance it is not trivial to determine the size of the particles. Scanning probe microscopy in general does not give accurate lateral sizes of objects due to the convolution of the object with the tip shape. Since the particles are relatively large this convolution can be correspondingly large, the average radius of particle in this image is 21 nm, far larger than the expected 5-7 nm from TEM images of similarly deposited NPs. The ideal way to use the AFM image is to have isolated clusters and to measure their maximum height relative to the substrate level, this avoids convolution effects. Isolated NPs grown uncapped in the same run under similar conditions showed diameters between 10 and 15 nm. For these densely packed samples no clear substrate minima exist so we can only measure the cluster areas, this gives us a relative NP size between samples within the limitations discussed below.

To do detailed statistics on the image it is first necessary to create a binary mask that demarks the areas of visible particles. To process the images, the open source software Gwyddion [208] was employed. Gwyddion contains a 'watershed' algorithm that finds local minima in the image, analogously to the process of dropping water and noting the location of puddles formed. Five parameters including droplet size and puddle threshold are used to determine the final binary mask. Fig. 4.4 (c) shows the same image as (b) with the binary mask overlaid in red. Visual inspection shows that the algorithm marks the majority of clusters accurately. It does have two fault types: the first can be seen at point (1) where noise levels swamp a small particle, this particle then breaks up into several small particles each a few nm in diameter. The second fault type can be seen at (2) where the definition between two particles is low and human judgement would rely on shape (which the algorithm disregards). The first fault type

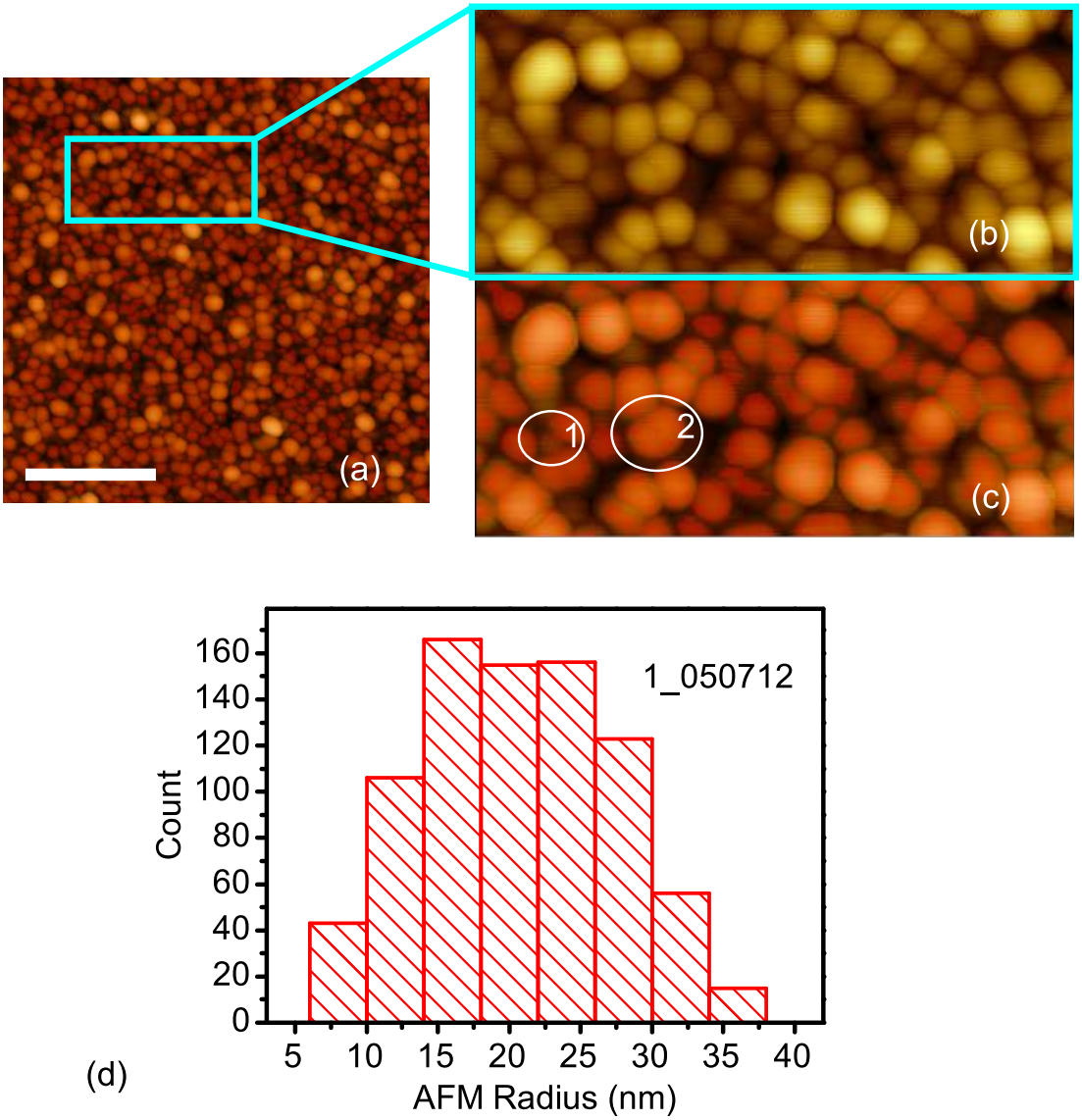


**Figure 4.4:** AFM data for sample 1_050712. (a) shows the large scan taken over 1.5 µm with the scale bar marking 500 nm. The indicated section of the image is cropped and zoomed for detail in (b). The nanoparticles are densely packed and larger than the expected nominal size. They can be masked with reasonable accuracy using the watershed algorithm, shown in red in (c). Two fault types are highlighted. A histogram plot of the NP effective radii is plotted in (d).

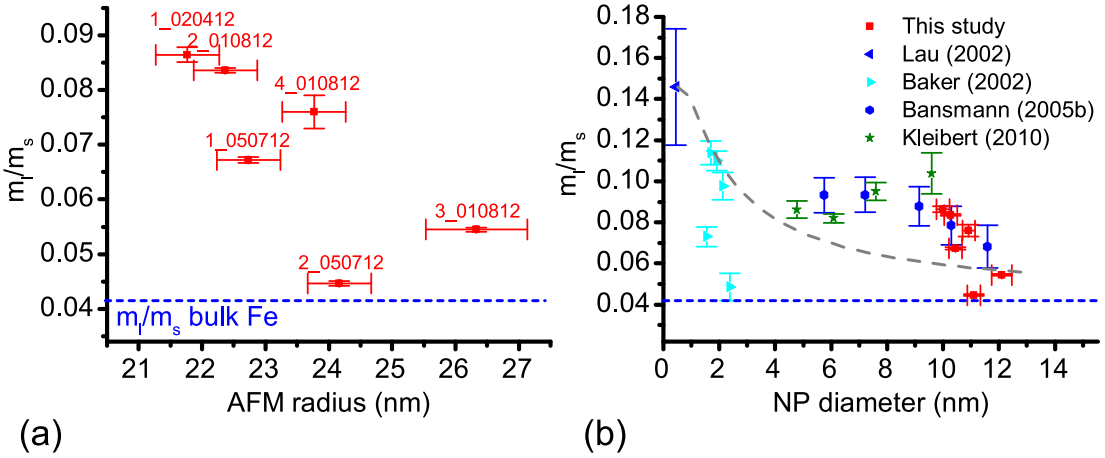


**Figure 4.5:** (a) $m_l/m_s$ ratio plotted against particle radius as found by AFM. the negative correlation is expected. The bulk Fe $m_l/m_s$ ratio is shown as a blue dashed line [173; 209]. In (b) the data is combined with data from previous studies [210–213]. The diameter for my particles has been scaled, see text for details. A grey dashed line is a fit to the two species model described.

leads to an inflated count rate of particles below 5 nm radius, these small particles are simply rejected. The second fault type cannot be easily taken into account, but occurs in less than 1% of NPs so should not affect our statistics greatly.

The size of the clusters is represented by an effective radius $r^*$ which is given in terms of the measured area of the particles $A$ as $\sqrt{A/\pi}$. The histogram of particle sizes for the image shown is plotted in Fig. 4.4 (d), this has the aforementioned cut off at $r^* = 5$ nm. This process was done for all of the samples. For each sample the same AFM tip was used and the same five parameters from the watershed algorithm. In Fig. 4.5 (a) the mean $r^*$ for each sample is plotted against the measured $r_{ls} = m_l/m_s$, there is a negative correlation (Pearson's $r = -0.83$) between the quantities. Despite the broad size distribution within an image, the standard error in the mean for the radii is small enough to differentiate the samples. Some of the samples have been left out from the plot, it was only possible to measure a certain number of samples with one tip before it was damaged, this was the maximum number achieved. The radius error bars are calculated as the standard error in the mean for the size distributions measured.

This AFM analysis presents a few questions. We cannot necessarily see all of the clusters, perhaps the density of clusters per unit area would affect the measured size? Also the measured size distribution of the particles is surprisingly wide, a standard

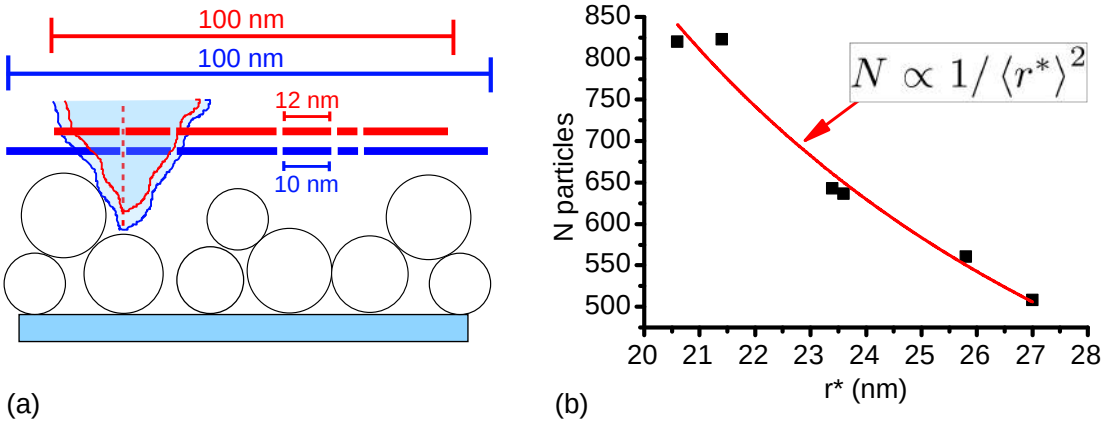


**Figure 4.6:** (a) diagrammatically represents the scaling model described in the text. (b) plots the average cluster radius as a function of the number of particles seen in the image, demonstrating the expected $N \propto 1/\langle r^* \rangle^2$ relationship.

deviation in the diameter of ≈16 nm. This does not seem consistent with simply a scaling factor due to tip convolution.

We can make an argument based on scaling that satisfies both of these observations. This is presented in a cross-section diagram of the AFM measurement Fig. 4.6 (a). The diagram represents scanning over two different samples. In the blue scale sample the average nanoparticle radius is 10 nm, in the red scale sample the average nanoparticle size is 20% bigger at 12 nm. The pattern of deposited particles obviously would not be identical between samples, but on average should produce the same results. The tip is kept the same between samples by scaling as drawn. Scanning the represented tip over the particles generates the dashed pattern shown in blue and red. Each dash shows the lateral size of the particle below that is measured. You can see that emergent particles appear far bigger than those below, completely distorting the real particle size distribution. This accounts for the wide distribution of particle sizes observed. The *average* measured size of the particles, however, has simply scaled by 20%. Thus we should not trust the measured size distribution, but we may rely on the scaling of the average size.

We have one important check on this argument. Looking again at Fig. 4.6 (a), a 100×100 nm image should contain 20% × 20% more clusters if the clusters are 20% smaller, i.e. we should have number of particles in image $N$ scale with average particle radius $\langle r^* \rangle$ as $N \propto 1/\langle r^* \rangle^2$. This is plotted for the measured samples in Fig. 4.6 (b)

and shows good agreement.

### 4.4.3 Enhanced orbital moments

We have determined the relative average size of the nanoparticles using AFM and found it negatively correlated to the $r_{ls}$ ratio in Fig. 4.5 (a). This correlation has been seen several times in the last decade or so by various groups [210–213]. The qualitative explanation generally given, is that atoms on the surface of the particle with reduced coordination number have more atomic-like enhanced orbital moments, while those in the centre retain the bulk-like quenched orbital moment. The spin moment is not found to be significantly different to bulk. This theory was developed more fully by Guirado-López et al. (2003) [214] using band structure calculations. They identified three key mechanisms for the orbital moment enhancement at the edge:

- The reduction of the local coordination number causes an increase in the local spin polarisation which enhances $m_l$ by means of the spin-orbit (SO) interaction.
- The Coulomb interaction favours the occupation of high $m$ states.
- Degeneracies in the single-particle spectrum allow enhanced SO mixing, increasing $m_l$ even when $m_s$ is saturated.

If this is the case, then it suggests our data should follow a two species mechanism. Atoms in the centre of the nanoparticle should have the quenched bulk $m_l/m_s$ ratio of $r_{ls}^{bulk} = 0.042$. Those within a small distance $d$ of the particle surface should have an averaged enhanced orbital moment $r_{ls}^{surf}$. For a spherical cluster of diameter $D$, the signal measured in this model would be

$$m_l/m_s = r_{ls}^{bulk}\left(1-\frac{2d}{D}\right)^3 + r_{ls}^{surf}\left[1-\left(1-\frac{2d}{D}\right)^3\right]. \tag{4.2}$$

In the large particle limit ($D \gg d$)this reduces to

$$m_l/m_s = r_{ls}^{bulk} + \left(r_{ls}^{surf} - r_{ls}^{bulk}\right)\frac{6d}{D}. \tag{4.3}$$

The result is the same if the cluster is considered a cubic shape. For large cluster diameters we recover the $r_{ls}^{bulk}$ value as expected.

In Fig. 4.5 (b) the data from previous reports has been combined with the data from the current study. Since we do not know the absolute size of the particles we have

measured, I have taken the minimum particle average on sample 1_020412 as 10 nm, and scaled the rest according to their measured average $r^*$. The 11 nm minimum was taken from measured sparse particle samples deposited in the same conditions and should give a systematic error of less than 1 nm. The data here measured agrees with the general trend of decreasing $r_{ls}$, particularly with the larger particles. It provides a study on a size range of particles larger than have been done before and the final ones are getting close to the bulk value of $r_{ls}$. A fit of the data using eq. 4.2 is shown. The trend of decreasing $r_{ls}$ is correct but the data does not fit well to the $1/D$ rule, in particular the gradient of our samples with larger radius is too steep. The model must neglect some of the physics involved, perhaps for the larger particles the core wavefunctions spread further into the surface atoms making them more bulk-like. The TEY signal can saturate in bigger particles due to the diameter exceeding the electron escape depth; this is thought to increase measured $r_{ls}$ by approximately 10-15% [187], it should not significantly affect the relative trend in $D$ however. Kleibert et al. [215] suggest another cause may be size dependent surface strain. Edmonds et al. [216] measured densely deposited nanoparticles and see $m_l$ dropping to bulk Fe values as particle density increases, this is attributed to touching particles having higher than average atomic coordination at their surface. We will consider this further after seeing the magnetometry data.

## 4.5 SQUID-VSM magnetometry

The same set of samples all subsequently underwent SQUID-VSM magnetometry studies. The samples were all cut to the size required for this instrument of 3×3 mm$^2$ (1_020412 was damaged in this process and was not measured). The same area of sample that had been measured in XMCD and AFM was saved for magnetometry. Except where stated the samples were measured with applied field $H$ in the plane of the film.

### 4.5.1 Anisotropy direction

Magnetisation vs. applied field measurements were made in the in-plane (IP) $x - y$ directions and out-of-plane (OOP) $z$. The results are shown in Fig. 4.7 (a). The IP orthogonal directions give the same result and show that the easy axis of the particles

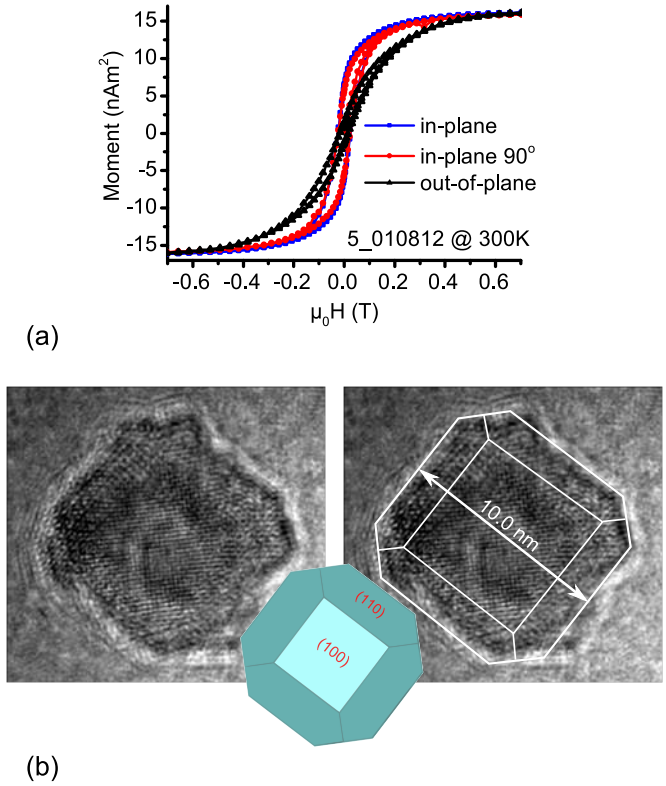


**Figure 4.7:** (a) hysteresis loops for nanoparticles taken at 300K. Applied field is in three perpendicular directions as indicated. The easy axes are randomly oriented in-plane. (b) high resolution TEM of a $Co_{30}Fe_{70}$ nanoparticle. The same image is shown on the right with guidelines indicating the Wulff reconstruction. >95% of the particles measured had the (100) face up.

must be in-plane, but randomly oriented within that plane. The OOP loop is the hard axis of the particle film, though there is a small hysteresis remaining, probably due to a few misoriented particles.

Fig. 4.7 (b) shows a TEM image of a nanoparticle grown in similar conditions. The particles are clearly seen to be bcc crystalline with energetically favourable surfaces (100) and (110) forming the Wulff reconstructed shape drawn. The measured lattice parameter $0.29 \pm 0.01$ nm matches with the 0.289 nm expected for bcc Fe. On the same sample >95% of the NPs had the same orientation, with the (100) plane sitting on the substrate (one particle was found in the (111) orientation). It is likely that the easy direction is along the (100) vectors due to magneto-crystalline anisotropy and in-plane due to the dipole-dipole interactions between the particles, this will be discussed further

later. Shape anisotropy could also play a part, if the particles are squashed slightly in the $z$ direction, a height to width ratio of 0.9 can induce an extra 3 μeV/atom anisotropy energy [161], adding to the bulk Fe magneto-crystalline anisotropy of 3.3 μeV/atom [217] in the (100) directions.

### 4.5.2 ZFC-FC

Zero field cooled - field cooled (ZFC-FC) measurements were done, up to the maximum temperature of the normal SQUID-VSM operating mode of 395 K. These are shown for a representative four samples in Fig. 4.8. The protocol is the same in each case (and described more generally in section 2.4.2):

1. The sample is heated to 395 K and a saturating negative field of -1 T is applied then released. It was hoped this would be above the blocking temperature so that particles would be randomly oriented. Any blocked particles are negatively saturated by the field.

2. The NPs are then cooled in zero magnetic field to 10 K, in theory this would create a randomly oriented distribution with zero average magnetisation. In these samples any particles still blocked at 395K will remain magnetised, giving a negative contribution to the sample moment.

3. A field of 10 mT is applied and the sample is warmed again to 395 K. As particles unblock the small field orients them, generating an average magnetic signal. The magnetization measured is shown in the blue ZFC curve.

4. In the same field the sample is cooled, the signal diverges from the ZFC as the particles freeze into a state oriented with the magnetic field. The magnetic signal measured is the red FC curve.

5. The applied field is dropped to zero. The sample is then warmed again, this is the green field warming (FW) curve. As the particles unblock they randomise in the field, lowering the signal.

Looking at the ZFC-FC measurements it is clear that the NPs have not fully unblocked by 395 K. The ZFC does not peak and immediately diverges from FC on cooling, this effect is particularly strong for 1_050712. In the fully SP state the FC

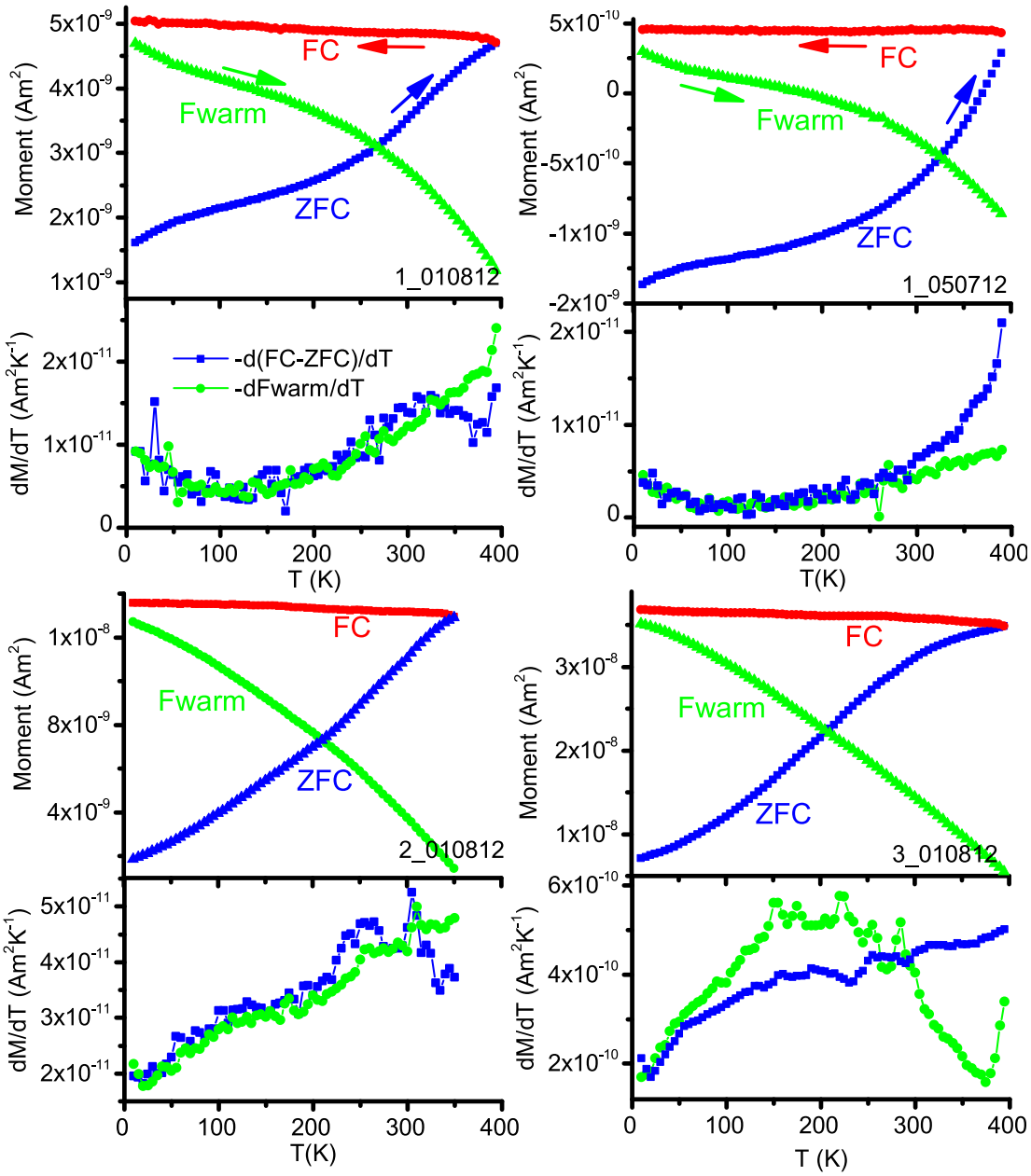


**Figure 4.8:** ZFC-FC measurements taken for four samples labled in each panel. These show that the particles have an unusually high blocking temperature ($T_B$). In each case the differential of the field warming (FW) curve is plotted in the lower panel, this gives the distribution of the particle $T_B$s. The distribution is very broad considering the size range of the particles.

and ZFC would align and fall as $1/T$. This is a surprising result, the blocking temperature $T_B$ is expected to be much lower than room temperature. Using a crude estimate of $T_B \approx KV/25k_B$ with bulk magneto-crystalline anisotropy for bcc Fe of $K_{bulk} = 4$ μeV/atom [157], gives $T_B \approx 120$ K for a 12 nm diameter particle. Previous experiments on similar particles [218] have given blocking temperatures in the range 50-150 K. We will discuss this anomaly further in section 4.5.4.

By differentiating the $m_{\mathrm{FW}}(T)$ curve we may get an idea of the distribution of NP blocking temperatures on a sample [219]. At each temperature the moment drops by an amount proportional to the number of particles that transition to the SP state at that temperature, therefore $-\mathrm{d}(m_{\mathrm{FW}})/\mathrm{d}T$ should be proportional to the number of particles with $T_B = T$. By similar arguments $-\mathrm{d}(m_{\mathrm{FC}} - m_{\mathrm{ZFC}})/\mathrm{d}T$ should be a similar measure. The differentials are plotted below the respective $m$-$T$ curves in Fig. 4.8. These two quantities agree for the most part and indicate a very broad distribution of blocking temperatures, starting from 10-100 K and increasing up to the 395 K limit. Again this is not what we expect. The particle volumes range from roughly 1300-2700 nm$^3$ so if bulk MC anisotropy is dominant then we might expect the largest blocking temperature to be a factor of $\approx 2$ greater than the smallest.

Since we cannot reach even the average blocking temperature of these particles using this instrument, we might find out the fraction that are SP at 395K. Assuming all of the particles are blocked at 10 K we may take the difference ZFC(395K)-ZFC(10K) as the sum magnetic moment of those particles with blocking temperatures below 395 K. Dividing this by the saturated moment for the sample (measured at 0.9 T) we may find the fraction $f_{<395}$ of SP particles at 395 K as $f_{<395} = (\mathrm{ZFC(395K)} - \mathrm{ZFC(10K)})/m_s$. These values are given in table 4.1 and range from 17-34%, this again indicates most of the particles are still to transition.

Further measurements on sample 3_010812 using the 'oven' mode on the SQUID-VSM extend the temperature range of the ZFC to 650 K but show qualitatively similar results. This is shown in Fig. 4.9.

### 4.5.3 $m$-$H$ hysteresis

Hysteresis loops were measured on all samples at a range of temperatures. This technique is more consistent than ZFC-FC measurements. Since the sample starts at a 0.9 T saturation field, hysteresis loops are not magnetic history dependent. Fig. 4.10

| Sample | $f_{<395}$ |
|---|---|
| 1_010812 | 0.24 |
| 2_010812 | 0.26 |
| 3_010812 | 0.26 |
| 4_010812 | 0.21 |
| 5_010812 | 0.17 |
| 1_050712 | 0.21 |
| 2_050712 | 0.34 |

**Table 4.1:** Fraction of particles with blocking temperatures below 395 K for each sample, as found from $f_{<395} = (\mathrm{ZFC(395K)} - \mathrm{ZFC(10K)})/m_s$

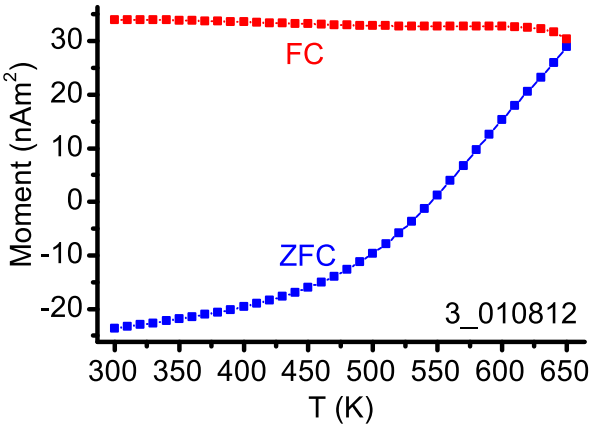


**Figure 4.9:** ZFC-FC measurements at elevated temperatures on sample 3_010812. Again the blocking temperature is not reached up to 650 K.

(a) shows hysteresis loops for sample 1_010812 from 50 to 395 K. The 50 K $m$-$H$ loop has opened out, consistent with blocked ferromagnetic particles arranged with easy axes randomly oriented in the plane. As the temperature increases the coercive field $H_c$ decreases, eventually with all of the particles in the SP state, we would expect the paramagnetic behaviour $H_c = 0$, we do not quite reach this state with this sample.

Fig. 4.10 (b) shows a one parameter fit of the 395 K hystersis loop to the Langevin function

$$m = m_s(\coth(x) - 1/x) \tag{4.4}$$

where $x = \mu_0 H m_{clust}/k_B T$ and $m_{clust}$ is the individual moment of a cluster. This fit gives $m_{clust} = 3.5 \times 10^4 \mu_B$, roughly equivalent to a particle diameter of 7.2 nm assuming

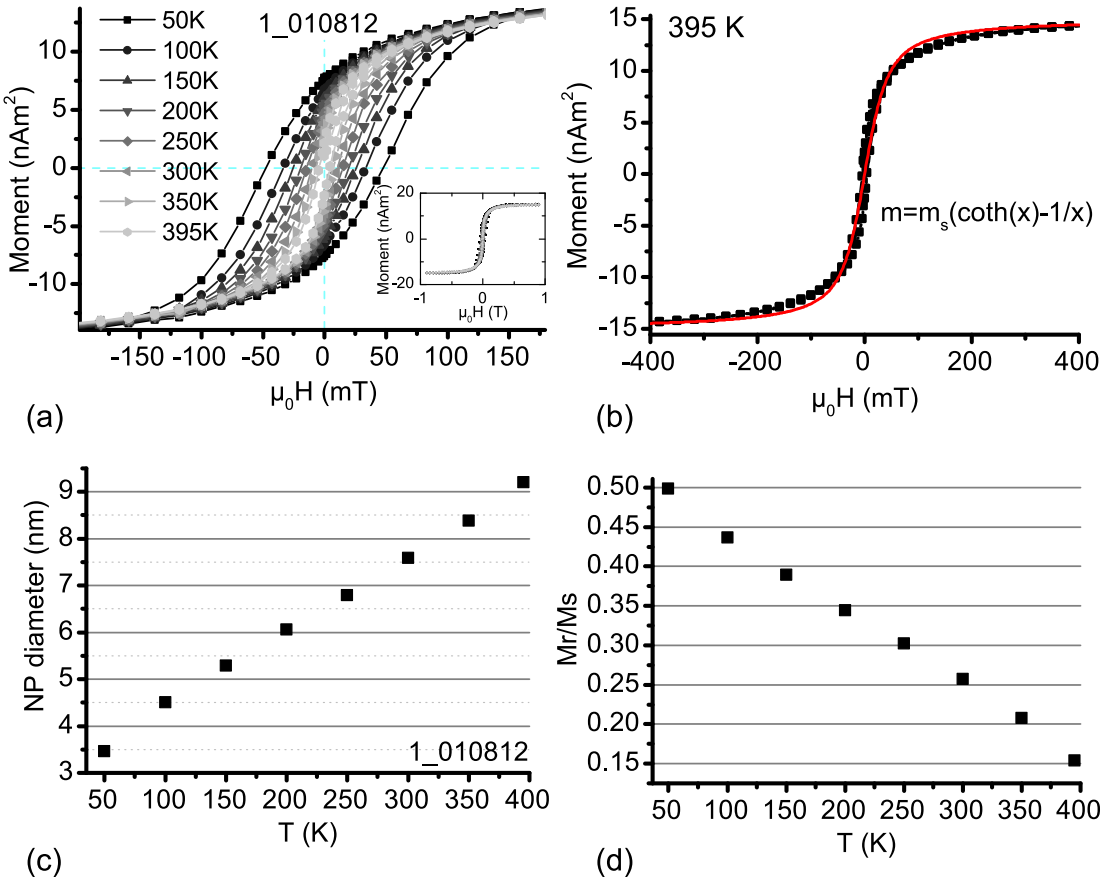


**Figure 4.10:** Magnetic hysteresis data for sample 1_010812. (a) shows $m$-$H$ for temperatures ranging from 50-395 K, the inset shows the complete loops, saturating fully at 0.9 T. In (b) the 395 K loop is fitted with a Langevin function, this predicts a particle size of $\approx 7$ nm. (c) plots the determined NP diameter for each temperature, it has clearly not saturated at 9.2 nm. This is again seen in $M_r/M_s$ calculated in plot (d). The sample has not yet reached the SP state at 395 K.

a moment per atom of $2.4\mu_B$ [220]. The function does not fit perfectly, the gradient at $H = 0$ is too small, this is to compensate the medium field fit where the Langevin function is too large. The poor fit is probably due to a combination of the particles not all being in the SP state, and the fact that we have not used a distribution of particle volumes in $x$.

$m_{clust}$ can be found more simply by using the small field approximation to (4.4):

$$\frac{\mu_0 \left(\frac{\mathrm{d}m}{\mathrm{d}H}\right)_{H=0}}{m_s} = \frac{m_{clust}}{3k_B T}. \tag{4.5}$$

The resulting $m_{clust}$ and equivalent particle diameter is calculated for each temperature and plotted in Fig. 4.10 (c). The calculated particle diameter increases linearly with temperature. Above the SP transition temperature we would expect the diameter to flatten out to a constant value. If the linear trend continued we would expect the diameter to reach the expected value of approximately 12 nm at T=580 K, again evincing a surprisingly high blocking temperature. Remenance moment normalised to the saturated moment plotted in Fig. 4.10 (d) shows the same picture, decreasing linearly with temperature but not flattening out.

The coercive field as a function of temperature for blocked particles can be modelled, in a one particle approximation, as [168]:

$$\mu_0 H_c = \frac{2KV}{m_{clust}} \left[1 - \left(\frac{T}{T_B}\right)^{1/2}\right] \tag{4.6}$$

In Fig. 4.11 $H_c$ vs. $T^{0.5}$ is plotted for all seven samples. A linear fit is a reasonable approximation in most cases. For samples 2_050712 and 3_010812, $H_c$ tails off to zero indicating they have passed their average blocking temperature, the point is marked with a dashed line and only points before that temperature are used for fitting. The fitting parameters are given in table 4.2 (a moment of 2.4 $\mu_B$/atom is assumed). The blocking temperatures range from 320-500 K, lower than the ZFC-FC data shows but still much higher than expected for this type of particle. The $KV$/atom values on the other hand are similar to the few μeV/atom measured in other studies [187; 217].

On some of the samples, for example 2_010812, the $H_c$ vs. $T$ data appears to drop non-linearly. The model used does not take into account a distribution of particle sizes and therefore blocking temperatures, this is known to cause significant non-linear deviations from the model [221]. This could also be the reason the anisotropy fields do not correlate well with the blocking temperatures.

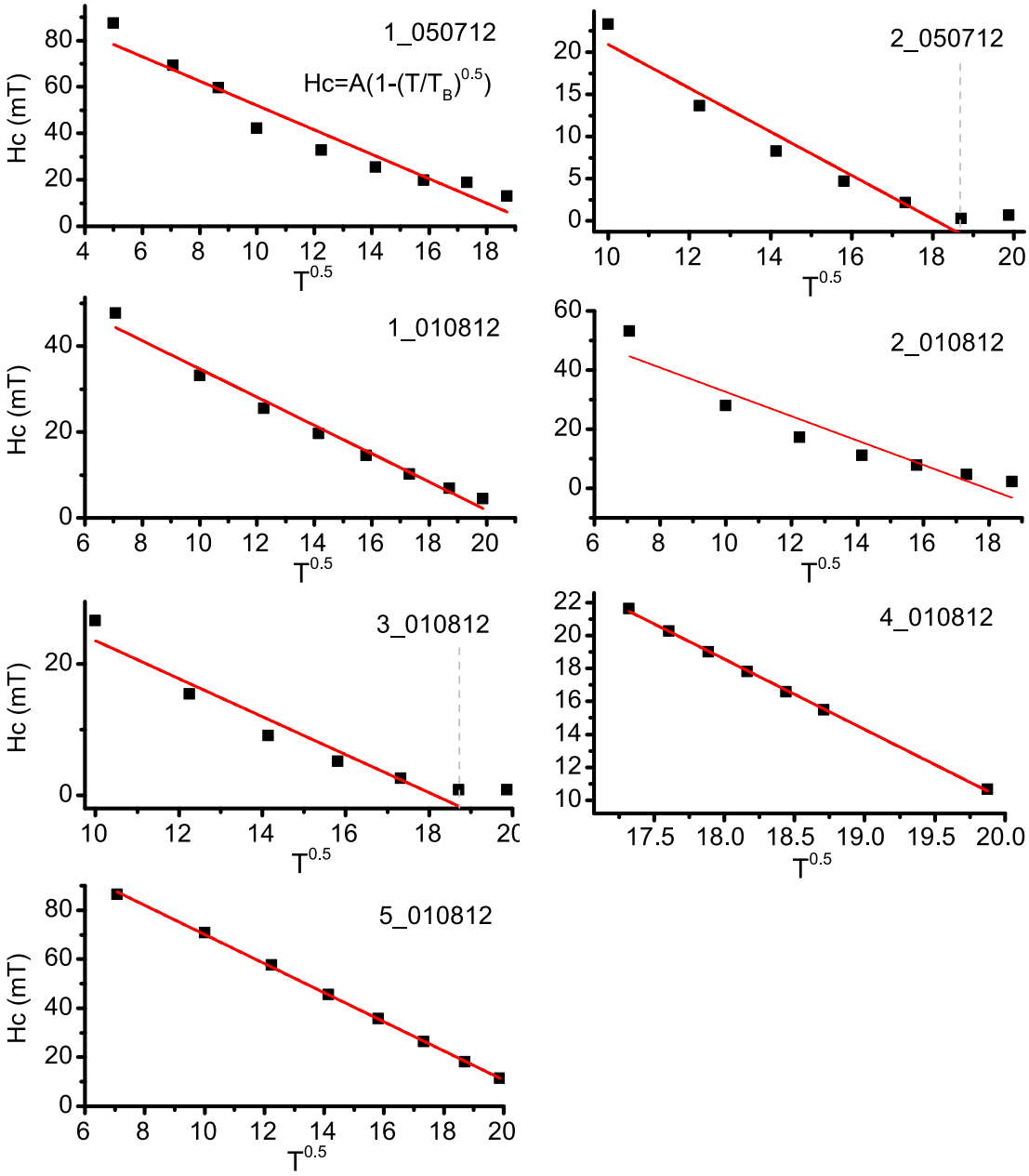


**Figure 4.11:** $H_c$ plotted against $T^{1/2}$ for each sample. The linear fits are modelled after the standard Stoner-Wohlfarth energy diagram. Two of the samples appear to have unblocked by the last point, these are indicated with dashed grey lines.

| Sample | $T_B$ (K) | $K$ (μeV/atom) |
|---|---|---|
| 1_010812 | $420 \pm 20$ | $2.8 \pm 0.1$ |
| 2_010812 | $320 \pm 30$ | $2.9 \pm 0.4$ |
| 3_010812 | $330 \pm 30$ | $1.3 \pm 0.1$ |
| 4_010812 | $499 \pm 2$ | $1.3 \pm 0.1$ |
| 5_010812 | $475 \pm 4$ | $5.6 \pm 0.04$ |
| 1_050712 | $400 \pm 40$ | $5.0 \pm 0.3$ |
| 2_050712 | $330 \pm 40$ | $1.4 \pm 0.1$ |

**Table 4.2:** Extracted fitting parameters from the $H_c$-$T^{0.5}$ data. Blocking temperatures and anisotropies do not correlate.

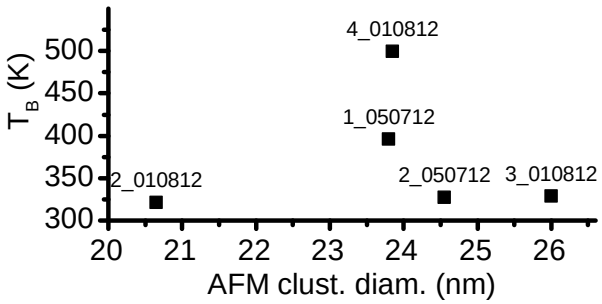


**Figure 4.12:** Blocking temperature plotted as a function of diameter as found from AFM. If the particles experience only volume anisotropy these would be expected to correlate. They do not.

We may expect for these large particles that the total anisotropy, and therefore blocking temperature, should be correlated to the particle volume. Plotting $T_B$ vs. average particle diameter from AFM in Fig. 4.12 however, shows that there is no correlation between these measured quantities within the limited data available.

### 4.5.4 Origin of high $T_B$

In summary, for these magnetometry measurements we have found from ZFC-FC protocols that the particle blocking temperatures appear to exceed 650 K, far higher than expected from both theoretical considerations and previous experiments. They are also shown to have a very broad distribution of $T_B$ values, far higher than expected for the given diameter distribution. They suggest a wide distribution of particle anisotropy en-

ergies ranging from $< 1$ μeV/atom to more than 10 μeV/atom (bulk $\alpha$-Fe cubic MC is 3.3μeV/atom [217]). $H_c$ vs. $T$ measurements show the samples fitting reasonably well to a $T^{1/2}$ law. Contrary to the ZFC measurements, some of the samples have already dropped to $H_c = 0$, indicating that their average $T_B$ is below 400 K. The extracted $T_B$ values do not correlate with the size of the particle as measured by AFM. The extracted anisotropy of the particles tallies well with the order of magnitude expected from the literature, but does not tally well with the extracted blocking temperatures. Samples with the extracted $KV$ values would be expected to have $T_B \approx 120K$ (as shown in section 4.5.2).

The answer may lie in the magnetic interactions between particles. Fig. 4.13 (a) plots the areal cluster density vs. the blocking temperature extracted from the $H_c$ vs. $T$ fits. While there was no correlation between $T_B$ and average particle size, here we see a weak negative correlation (of $r = -0.72$) between $T_B$ and the density of particles on the sample. Plotting $M_r/M_s$ at 395 K as a function of cluster density in (b) also yields a negative correlation, again indicating the particle anisotropy is tied up with the density of particles on the sample. Cluster density in these cases is determined by using the total magnetic moment of the sample divided by its area and dividing that by the calculated magnetic moment of a 12 nm particle. We can do the same using the particle diameters determined by Langevin fits: the correlation is the same but the cluster density is high because the fits gave small diameters.

Fig. 4.13 (c) shows a representation of 12 nm particles randomly dispersed over a surface at a density of 3000 μm$^{-2}$, it is clear the particles are relatively close and touch in some places. The probability distribution of the nearest neighbour radius $r$ for a given particle, follows Poisson's distribution as [222]

$$P(r) = 2\pi r N_A \exp(-\pi r^2 N_A) \tag{4.7}$$

where $N_A$ is the areal particle density. This function is plotted in 4.13 (d) for $N_A =$ 3000 μm$^{-2}$. Integrating, approximately 75% of the particles are overlapping, assuming a diameter of 12 nm.

Long range dipole interaction forces between particles are likely to be significant due to the particles being at percolation. Naively one would guess that the dipole interactions would create a glass-like structure, with randomly oriented moments fixed in place by the dipole fields from the nearest neighbours. The mutual magnetic dipole potential energy between two particles is proportional to $\mu_0 m_{\text{clust}}^2/r^3$ where $r$ is the

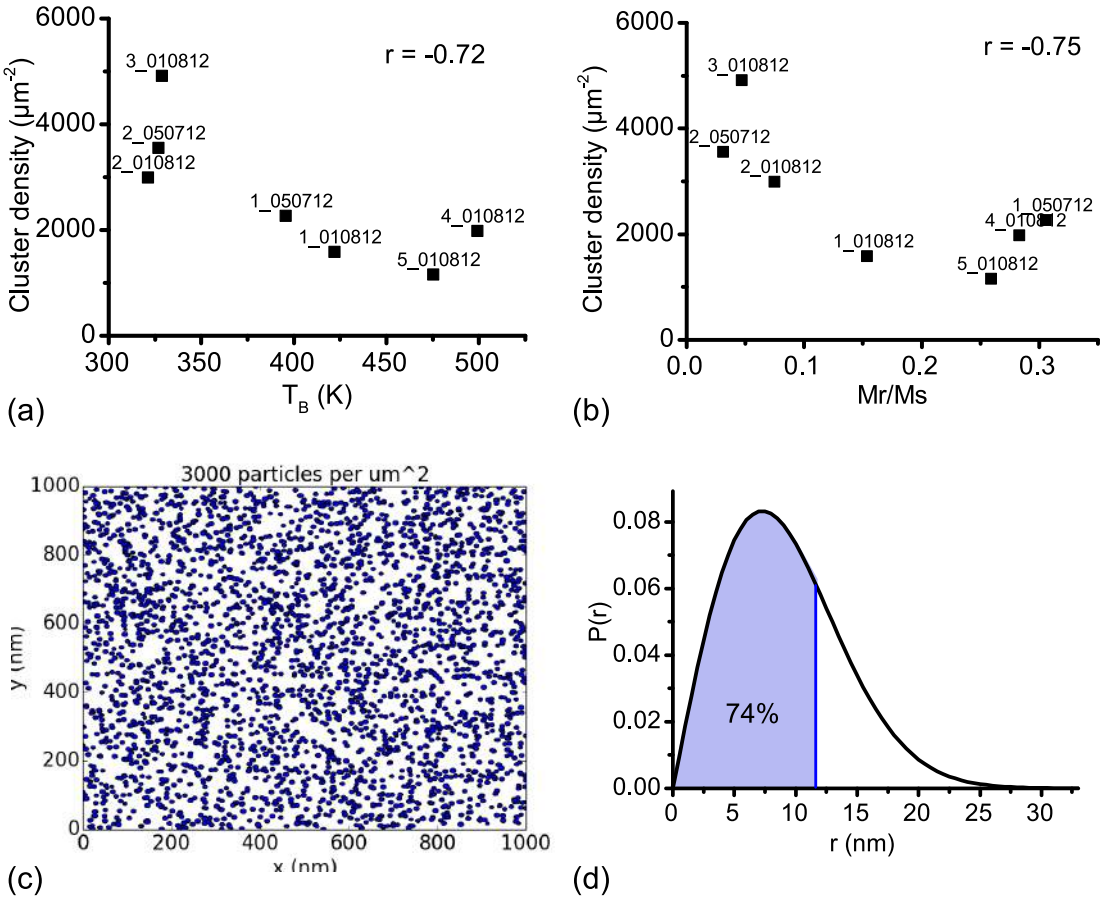


**Figure 4.13:** (a) and (b) show NP density plotted against $T_B$ and $M_r/M_s$ ratio respectively. Both are a measure of the effective anisotropy of the sample and show a negative correlation with particle density. This indicates that dipole-dipole interactions are causing the unusual blocking temperature ranges. (c) shows a simulated random deposition of particles onto a surface at a density of 3000 $\mu m^{-2}$. Nearest neighbour calculations shown in (d) indicate approximately three quarters of the particles are touching their neighbour.

centre-to-centre distance. This energy equates to a temperature of between 300-3000 K for adjacent 12 nm particles (the high sensitivity of the calculation to $r$ and $m_{\text{clust}}$ gives a high variation in the approximate calculation). This energy scale is much greater than the anisotropy energy scale at $\sim 120$ K and is likely to be the origin of the large mean and standard deviation of blocking temperatures observed. This effect has been seen in high density samples before by Fauth et al. [223], in this case the particles were deposited on a Cu(111) surface. In the paper the broad anisotropy range was attributed both to agglomerated interacting particles and substrate mediated interactions. In our case with an insulating substrate we rule out this latter effect. Ebbing et al. [224] also see blocking temperatures enhanced by a factor of 5 fold, in their case due to induced magnetisation of a Pt cap. In our samples with an Al cap of low spin-orbit coupling this is unlikely to be the case.

This interaction picture fits the large blocking temperatures but does not however agree with the relative densities between samples. These were seen to be *negatively* correlated with the blocking temperatures. This is an interesting effect and difficult to explain, it requires further theoretical investigation. The complex network of interactions could be highly dependent on the particle density.

## 4.6 Conclusions

In conclusion we have studied the magnetic properties of densely packed $Co_{30}Fe_{70}$ nanoparticles in the size regime 11-14 nm. XMCD spectroscopy combined with AFM size determination reveal the Fe orbital to spin moment ratio $m_l/m_s$ is correlated with particle size. This is an established phenomenon but has not been carried out with such large particles before. At this large size it is found the $m_l$ values decrease very rapidly compared to the trend expected from a simple two species model. This could be attributed to problems with the current theory for large radius particles, or could be caused by size dependent strain effects.

While the particles are not exchange coupled (else the orbital moments would be quenched), magnetometry studies indicate that they are interacting through the magnetic dipole force. The sensitivity of the dipole interaction to the moment and nearest neighbour distance, gives extremely wide distributions of effective particle anisotropies and therefore blocking temperatures. From a physics point of view, interactions between particles is a very interesting effect that yields unpredictable results. Contrary

to expectations, we find the average blocking temperatures to be negatively correlated with the particle density.

# Chapter 5

Theoretical solutions of spin accumulation in DMTJs

## 5.1 Introduction

In section 2.3.1 I introduced the so-called orthodox theory, used to calculate the electronic behaviour of single electron transistors and double tunnel junctions. This chapter will focus on incorporating spin effects into the orthodox theory, especially focussing on spin accumulation in the nanoisland. Our contribution to this theory has been to find an analytical solution (under an asymmetric junction approximation) to the existing theory which is currently solved with numerical methods; this gives us insight into the complex solutions of these equations, necessary for fitting to measurements from real systems. We show that the magnetic properties of the junction can be determined simply from studying the I-V profiles of the junction and therefore that a single magnetic electrode could be used for simultaneously injecting and detecting spin polarised current in a individual nano device. This body of work has been published in the journal Physical Review B [225].

Introducing magnetic components into a double tunnel junction means that tunnelling rates onto the island will differ for up and down spin species. Unequal spin tunnelling rates can cause a spin accumulation on the island, this modifies (by $\Delta E$) the chemical potential, which then affects the overall state current contribution. Barnaś and Fert (1998) [3; 226] were the first to adapt the orthodox theory to account for spin accumulation. Using a simple two channel model the orthodox equations were changed, the tunnel rates are made spin dependent by simply using spin dependent tunnelling resistances $R_i^{\downarrow}$ and $R_i^{\uparrow}$. The total current is found from summing the current from both spin channels. The difficulty is to find the appropriate spin accumulation for a given configuration, this must be done in a self-consistent calculation explained in more detail below.

The solutions to the theory of Barnas and Fert showed that spin accumulation modified the Coulomb staircase in a periodic fashion. Going further and predicting TMR-V curves, the solutions predicted oscillating MR with bias. This prediction has been verified experimentally by independent groups [109; 123; 227], an example fit to experimental data is shown in Fig. 5.1. The theory solutions have since been developed [4] and used to study frequency dependent effects [228; 229], gate polarisation effects [230], strong coupling and co-tunnelling regimes [92; 231] and island arrays [232]. For a review of theoretical developments see Barnaś and Weymann (2008) [5].

To summarise the orthodox theory described in section 2.3.1: we treated the excess

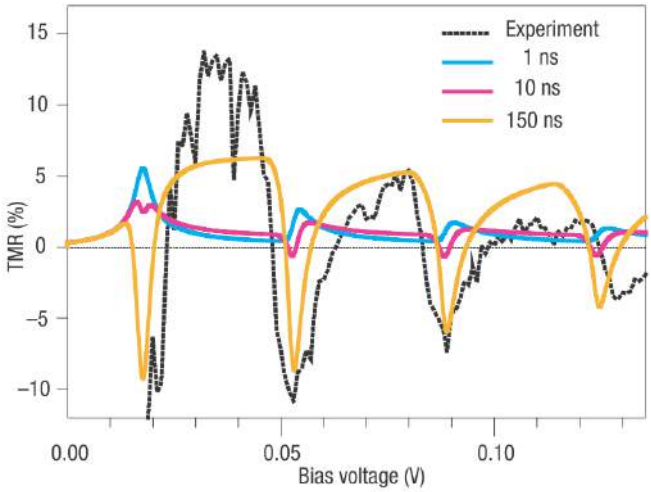


**Figure 5.1:** Theoretical fit of the TMR to experimental data in a Co-Co-Al DMTJ structure. Figure adapted from [109].

electron number $N$ on the island as a good quantum number. This allowed us to incoherently sum the current contributions from each state $N$ to obtain the total current $I$ at a given bias $V$ (eq. 2.22). The state probabilities $\sigma(N)$ were found from detailed balancing of the rates for each state (eq. 2.23). The tunnelling rates $\Gamma_i^{\pm}$ were found from Fermi's golden rule (eq. 2.19), if the free energy change is favorable the rate is proportional to the energy difference $\Delta U_i^{\pm}/e^2 R_i$ (at T=0 K). $R_i$ is an effective junction resistance proportional to the joint density of states and the transfer matrix (assumed bias independent).

## 5.2 Model

The model is set up as a double tunnel junction shown in Fig. 5.2(a), with $N$ excess electrons on the central island and $\Gamma_{i\sigma}^{\pm}$ the spin-dependent electron tunnelling rates onto (+) and off (-) the island (the electrode label $i \in 1, 2$ and the spin label $\sigma \in \uparrow, \downarrow$). A Fermi golden rule type calculation is used to find the tunnelling rates which are given as

$$\Gamma_{i\sigma}^{\pm} = \frac{1}{e^2 R_{i\sigma}} \frac{-\Delta U_{i\sigma}^{\pm}(N,V)}{1-\exp(\frac{\Delta U_{i\sigma}^{\pm}(N,V)}{kT})} \approx \begin{cases} \frac{\Delta U_{i\sigma}^{\pm}}{e^2 R_{i\sigma}}, & \Delta U_{i\sigma}^{\pm} < 0 \\ 0, & \Delta U_{i\sigma}^{\pm} > 0 \end{cases} \tag{5.1}$$

where the approximation on the right, which we make for our analytical solution, is that the temperature energy scale is much smaller than the charging energy scale

($kT \ll E_{\mathrm{C}}$). Finite temperature leads to a broadening of the step 'riser' of width $kT/e$. Effective resistance $R_{i\sigma}$ is dependent on the junction's mutual density of states and tunnelling matrix, which in general are spin dependent but over a range of energy small compared to the bandstructure variations will be approximately independent of applied bias [3].

For convenience we also define each barrier's total conductance as the sum of the two parallel spin channels $1/R_{i\mathrm{T}} = 1/R_{i\downarrow} + 1/R_{i\uparrow}$ and the spin dependent tunnelling rate ratio as $P_i = R_{i\uparrow}/R_{i\downarrow}$. $\Delta U^{\pm}_{i\sigma}(N,V)$ is the electrostatic energy change on transferring an electron through a tunnel barrier onto or off the island on the relevant side, enacting the change $N \to N \pm 1$. Using electrostatic considerations it is calculated as

$$\begin{aligned} \Delta U^{\pm}_{1} &= \frac{e^2}{C}\left(\frac{1}{2} \pm \left(-\frac{C_2 V}{e} + N - Q_0\right)\right) \pm \Delta E_\sigma \\ \Delta U^{\pm}_{2} &= \frac{e^2}{C}\left(\frac{1}{2} \pm \left(\frac{C_1 V}{e} + N - Q_0\right)\right) \pm \Delta E_\sigma, \end{aligned} \tag{5.2}$$

with $C = C_1 + C_2$, $Q_0 e$ the constant offset charge on the island caused by stray capacitances in the environment, and $\Delta E_\sigma$ the additional spin dependent chemical potential on the island which adjusts as spin builds up on the island.

The total current through the device, the sum of the two spin channels $I(V) = I_\downarrow(V) + I_\uparrow(V)$, is given by coherently summing the appropriate rates for the ensemble of possible island states:

$$I_\sigma(V) = e \sum_{N=-\infty}^{\infty} \sigma(N)(\Gamma^{-}_{2\sigma}(N) - \Gamma^{+}_{2\sigma}(N)) \tag{5.3}$$

where $\sigma(N)$ is the probability of finding the island in state $N$. The probabilities $\sigma(N)$ can be calculated by using the fact that in the steady state the net probability of making a transition between adjacent states is zero

$$\begin{aligned} &\sigma(N)(\Gamma^{+}_{1}(N) + \Gamma^{+}_{2}(N)) \\ &\qquad = \sigma(N+1)(\Gamma^{-}_{1}(N+1) + \Gamma^{-}_{2}(N+1) \end{aligned} \tag{5.4}$$

and that the ensemble probabilities must sum to unity

$$\sum_{N=-\infty}^{\infty} \sigma(N) = 1, \tag{5.5}$$

where $\Gamma^{\pm}_{i}(N) = \Gamma^{\pm}_{i\downarrow}(N) + \Gamma^{\pm}_{i\uparrow}(N)$.

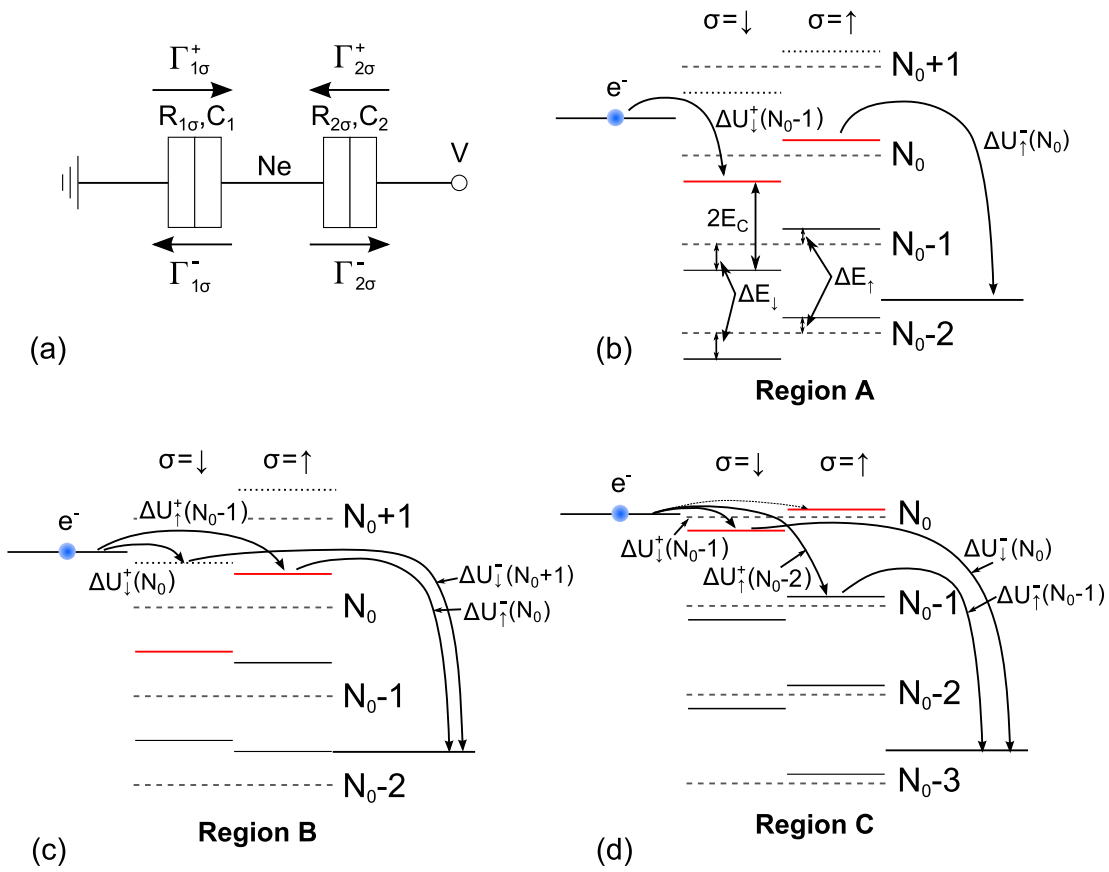


**Figure 5.2:** Schematics of the model. (a) A circuit diagram indicating rates and parameters for Coulomb staircase theory. (b) An energy profile of the system for positive applied bias. On the left is the Fermi energy in electrode 1 and right is the Fermi energy for electrode 2, in the centre the island energy levels are split by the spin accumulation chemical potential. Level $N_0$ is shown for the given applied bias. The system is in region A with increasing spin accumulation. (c) shows the system in region B with an extra $\downarrow$ channel acting to decrease the spin accumulation. (d) the system is in region C with the smallest spin accumulation, note that $N_0$ has jumped to the new level.

Finally the spin accumulation $\Delta E_\uparrow$ is determined by the spin conservation equation

$$I_{1\uparrow} - I_{2\uparrow} = \frac{eD_\uparrow \Omega}{\tau_r} \Delta E_\uparrow, \tag{5.6}$$

where $\Omega$ is the particle volume, $D_\sigma$ is the island density of states at the Fermi energy for electrons of spin $\sigma$ and $\tau_r^{-1}$ the spin relaxation rate on the island. We also impose the charge conserving restriction $D_\uparrow \Delta E_\uparrow = -D_\downarrow \Delta E_\downarrow$.

Equations (5.1-5.6) together give a complete solution to $I(V)$ when solved self-consistently for $\Delta E_\uparrow$[4; 226]. The solution, however, is numerical and it is therefore difficult to interpret the relationship between the resulting predictions and the barrier parameters. To proceed with our analytical solution we make the asymmetric junction approximation $R_{2T} \gg R_{1T}$. Because of this imbalance in rates, the island will preferentially sit in the state $N_0$, just below the left electrode Fermi energy and we may make the approximation $\sigma(N_0) \approx 1 \gg \sigma(N_0 - 1)$. State $N_0$ is highlighted in red in Fig. 5.2(b). Mathematically $N_0$ is the lowest integer that satisfies $\Delta U_{1\uparrow}^-(N_0 + 1) < 0$ (i.e. the level below that which will reverse the current direction), which solves to give

$$N_0 = \frac{1}{2} + \frac{C_2 V}{e} + Q_0 - \delta \tag{5.7}$$

where $\delta$ varies over the Coulomb step between 0 and 1 maintaining $N_0$ as an integer as $V$ varies. $\delta$ will serve as a useful parameter to define the position within any step of the Coulomb staircase, independent of the step number, later on.

Solving (5.3) using these approximations gives a Coulomb blockade $I = 0$ region when $N_0 = 0$ and $\Delta U_i^\pm(0, V) > 0$ are all satisfied, and an $I(V)$ function

$$\begin{aligned} I(V) \quad = \quad & \frac{1}{R_{2T}C}\left(C_2 V_0 + C_1 V + \frac{e}{2}[1 - \mathrm{sgn}(V)]\right) + \\ & \frac{\Delta E_\uparrow}{eR_{2T}} \frac{1 - P_2 D_r}{1 + P_2}. \end{aligned} \tag{5.8}$$

$V_0 = \frac{e}{C_2}(N_0 - Q_0 - \frac{1}{2})$ is the bias at the start of the $N_0{}^{\text{th}}$ step, $D_r = D_\uparrow / D_\downarrow$ and $\mathrm{sgn}(V)$ is a function that returns 1 for $V > 0$ and -1 for $V < 0$. The first term in this expression for $I(V)$ is simply the orthodox expression [61] with $R_{2T}$ taking the place of the conventional tunnel resistance, it describes a discontinuous staircase with step width $\Delta V = e/C_2$, offset $Q_0 \Delta V$ and step gradient $(\mathrm{d}I/\mathrm{d}V)_o = C_1/R_{2T}C$. The second term is the additional effect that is encountered when a spin accumulation is allowed to occur and is central to interpreting the effects of spin asymmetry in this structure.

## 5.3 Spin accumulation

To understand the spin accumulation term in (5.8) we use the spin conservation equation (5.6) to calculate $\Delta E_\uparrow$. In fact in each step there are three sections to solve for, they are defined by the position of the left electrode Fermi level relative to the $\uparrow$ / $\downarrow$ Fermi levels of the island electrons. In Fig. 5.2(b) they are highlighted and labelled as regions A, B, and C. For simplicity we will here follow the solution through for positive applied bias, a similar solution exists for negative bias and can be found by the same methods.

Starting in region A, of the terms in the spin conservation equation (5.6) $I_{2\uparrow}$ is immediately available from a calculation similar to that used to find $I(V)$ (5.8). $I_{1\uparrow}$ presents more problems since at $N_0$ for $kT = 0$ there is zero current to first order. To solve we go to the second order term in the current sum and find $\sigma(N_0 - 1) \approx \Gamma_2^-(N_0)/\Gamma_1^+(N_0 - 1)$. This leads to the following expression for spin conservation:

$$\Gamma_{1\uparrow}^+(N_0 - 1)\frac{\Gamma_2^-(N_0)}{\Gamma_1^+(N_0 - 1)} - \Gamma_{2\uparrow}^-(N_0) = \frac{D_\uparrow \Omega \Delta E_\uparrow}{\tau_\mathrm{r}}. \tag{5.9}$$

The tunnelling rates $\Gamma$ all depend linearly on $\Delta E_\uparrow$ and therefore (5.9) represents a quadratic in $\Delta E_\uparrow$. When fully expanded this quadratic can be written

$$a\Delta E_\uparrow^2 + b\Delta E_\uparrow + c = 0 \tag{5.10}$$

where

$$\begin{aligned} a &= (1 - Q)D_\mathrm{r} + \frac{e^2 R_{1\uparrow} R_{2\downarrow}}{R_{1\mathrm{T}}} \times \frac{1 - P_1 D_\mathrm{r}}{1 + P_1} \times \frac{D_\uparrow \Omega}{\tau_\mathrm{r}}, \\ b &= -2E_\mathrm{C}\left[(D_\mathrm{r} + Q)\delta + (1 + QD_\mathrm{r})(CV/e - \delta)\right] - \\ &\qquad \frac{2e^2 R_{1\uparrow} R_{2\downarrow} E_\mathrm{C}\delta}{R_{1\mathrm{T}}} \times \frac{D_\uparrow \Omega}{\tau_\mathrm{r}}, \text{ and} \\ c &= 4E_\mathrm{C}^2(1 - Q)\delta(CV/e - \delta). \end{aligned}$$

This quadratic can be solved with the quadratic formula to give a complex expression for $\Delta E_\uparrow$, from which the non-divergent solution is chosen.

More informatively, we can examine the steps further up the staircase where $\Delta E_\uparrow / eV_0 \ll 1$ (achieved on the 2$^{\mathrm{nd}}$ or 3$^{\mathrm{rd}}$ step for typical junction parameters). If we also approximate that the spin relaxation time is long then in this case we find the useful result

$$\Delta E_\uparrow \approx 2E_\mathrm{C}\delta\frac{1 - Q}{1 + QD_\mathrm{r}}, \tag{5.11}$$

with $Q = P_1/P_2$ the spin resistance asymmetry ($P_i = R_{i\uparrow}/R_{i\downarrow}$). In this solution, the spin accumulation begins a new step at zero and linearly increases or decreases with increasing $V$.

Regions B and C start at the point at which the left electrode Fermi level moves above the island $N_0 + 1 \downarrow$ (or $\uparrow$ if $Q > 1$) level. The potential at this transition point can be calculated as a fraction of the step width as

$$v_{\mathrm{m}} = \frac{V_{\max} - V_0}{\Delta V} = \begin{cases} \frac{1+QD_{\mathrm{r}}}{Q(1+D_{\mathrm{r}})}, & Q > 1 \\ \frac{1+QD_{\mathrm{r}}}{1+D_{\mathrm{r}}}, & Q < 1\,. \end{cases} \tag{5.12}$$

In B and C, where a new channel has opened up exclusive to $\downarrow$ electrons, the spin accumulation is expected to decrease as the $\downarrow$ spins drain from the island. In fact, owing to the extra tunnelling channel available to the electrons, the solution is a cubic with complex dependence on the parameters. The behaviour turns out to be as expected, but the complexity of the analytical form adds little insight to our understanding. To briefly outline the current calculation in regions B and C: we choose for specificity $Q < 1$ so that $\uparrow$ spins have accumulated, a similar solution can be found for $Q > 1$. The method proceeds similarly to the solution given for region A except that here we must allow for both second order terms $\sigma(N_0 - 1)$ and $\sigma(N_0 + 1)$. Using equations (5.3) and (5.4) we find

$$\begin{aligned} &\Gamma^+_{1\uparrow}(N_0 - 1)\frac{\Gamma^-_2(N_0)}{\Gamma^+_1(N_0 - 1)} - \Gamma^-_{2\uparrow}(N_0) \\ &\quad + \frac{\Gamma^+_{1\downarrow}(N_0)\Gamma^-_{2\uparrow}(N_0 + 1)}{\Gamma^-_2(N_0 + 1) + \Gamma^-_{1\uparrow}(N_0 + 1)} = \frac{D_\uparrow \Omega \Delta E_\uparrow}{\tau_{\mathrm{r}}}\,. \end{aligned} \tag{5.13}$$

Again the tunnelling rates $\Gamma$ are linear in $\Delta E_\uparrow$ and so in this case the result expands to a cubic in $\Delta E_\uparrow$. The full expansion is over fifty terms. This can be solved either numerically or analytically and the non-divergent solution taken to complete the expression for $\Delta E_\uparrow$ in B. C has the same $\Delta E_\uparrow$ solution but in this case $N_0$ has changed so we must use the transformation $N_0 \to N_0 - 1$ in (5.13) and (5.8).

## 5.4 Results

The results of these calculations are shown in Fig. 5.3(a) and compared to the full numerical solution for two cases $R_{2\mathrm{T}}/R_{1\mathrm{T}} = 500$ and 50. The analytical solution to

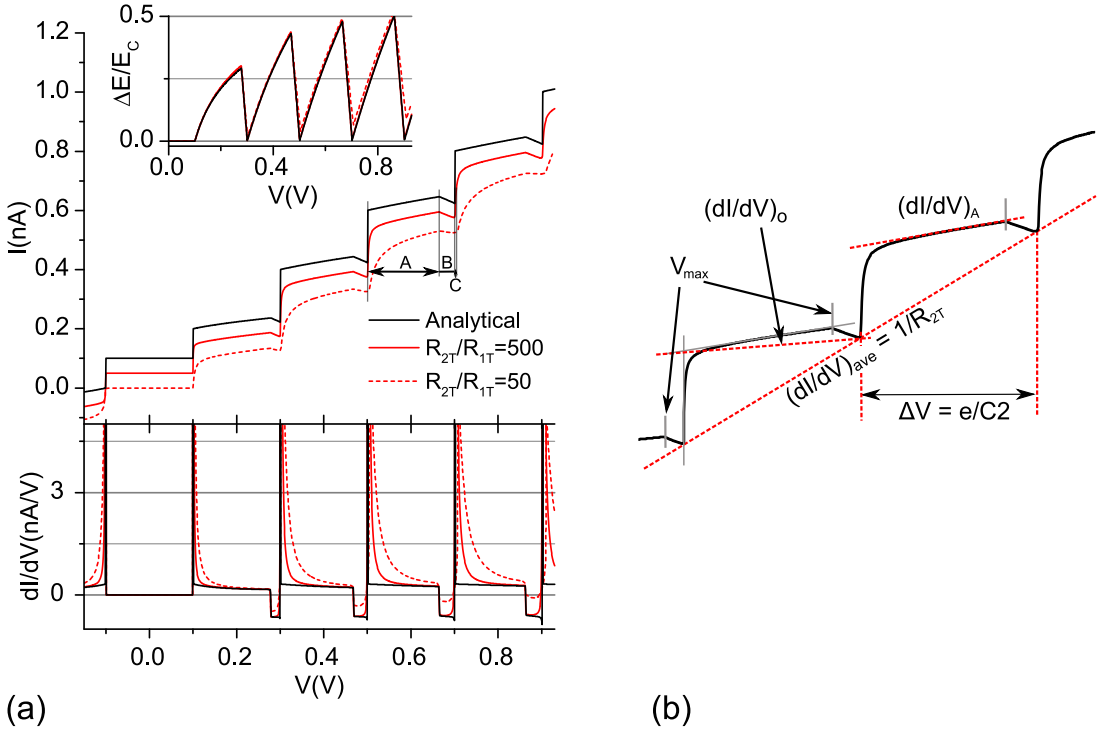


**Figure 5.3:** Results of the model. (a) A comparison of the analytical solution to numerical simulation for two different ratios of $R_{2\mathrm{T}}/R_{1\mathrm{T}}$. Current (curves offset for clarity) above and differential resistance below, the inset shows the spin accumulation varying as a function of bias. (b) An expanded view is given, with $I(V)$ features used for parameter determination labelled. The parameters used were $R_{2\mathrm{T}} = 1$ GΩ, $P_1 = 1/8$, $P_2 = 1/4$, $C_1 = 0.1$ aF, $C_2 = 0.8$ aF, $Q_0 = 0$, $D_\mathrm{r} = 3/4$, $\tau_\mathrm{r}/\tau_\mathrm{s} = 10^3$.

$I(V)$ shows excellent agreement with the numerical calculation for 500, but starts to deviate for 50 as the $R_{2\mathrm{T}} \gg R_{1\mathrm{T}}$ assumption begins to break down and levels below $N_0$ start to populate. The differential conductance shown below the $I(V)$ demonstrates the expected sign change within the step as the system passes from region A to B, and the gradient is positive in A as expected for our parameter choice. The spin accumulation on the island shown in the inset of Fig. 5.3(a) oscillates, increasing in A and decreasing in B/C.

There are two major deviations to the analytical solution that increase as $R_{2\mathrm{T}}/R_{1\mathrm{T}}$ decreases. The first is a lower than expected current near the beginning of the step, this tends to smear out the Coulomb staircase and reduce the $\mathrm{d}I/\mathrm{d}V$ signal. It occurs at the beginning of the step where the tunnelling rate into the new $N_0$ level is relatively

slow and the $N_0 - 1$ level can still hold a significant population. The second effect is that the island spin accumulation is not completely eliminated before the start of the next step, the system is therefore in region C for a small period after the orthodox step start point and a slight expansion of the step is seen, becoming more pronounced at higher bias. While the first effect is generally undesirable, the latter shift, if different for anti-parallel and parallel magnetic configurations, can give rise to the TMR sign change switching seen in previous work [3]. In general however, the cleanest and most detailed results will come from devices that satisfy the $R_{2\mathrm{T}} \gg R_{1\mathrm{T}}$ criterion whilst still maintaining $C_1 < C_2$.

Looking again at the final solution for $I(V)$ in region A given by (5.8) and (5.11) combined, we find that the modification due to spin accumulation is an additional maximum or minimum in each step in the Coulomb staircase. The position of the stationary point is given by (5.12) and the gradient of the step in region A is given by

$$\left(\frac{\mathrm{d}I}{\mathrm{d}V}\right)_{\mathrm{A}} = \frac{C_1}{R_{2\mathrm{T}}C} + \frac{C_2}{R_{2\mathrm{T}}C}\frac{(1-Q)(1-D_{\mathrm{r}}P_2)}{(1+QD_{\mathrm{r}})(1+P_2)}. \tag{5.14}$$

From this we see that inner step maxima indicates that $(1-Q)(1-D_{\mathrm{r}}P_2) > 1$ and vice versa for step minima. This dependence on $Q$ is physically reasonable as $P_1$ essentially determines the rate that spin accumulation builds through the left junction and $P_2$ the rate that the spin accumulation drains through the right. Importantly we see an imbalance in $P_1/P_2$ is required, a symmetric ferromagnetic junction will not accumulate spin. The spin effects on the $I(V)$ curve are of greatest magnitude for $Q, P_2 \ll 1$ or $Q, P_2 \gg 1$, and are suppressed as $Q$ or $P_2 \to 1$.

The relative complexity of the $I(V)$ shape means that many parameters can be fitted independently, the different features are highlighted in Fig. 5.3(b). From step width $\Delta V$, bias offset, $\mathrm{d}I/\mathrm{d}V_{\mathrm{o}}$ and $\mathrm{d}I/\mathrm{d}V_{\mathrm{ave}}$ we find $R_{2\mathrm{T}}$, $Q_0$, $C_2$ and $C_1$. $V_{\mathrm{max}}$ and $\mathrm{d}I/\mathrm{d}V_{\mathrm{A}}$ given in (5.12) and (5.14) combine to give any two of the three spin parameters $P_1$, $P_2$ and $D_{\mathrm{r}}$, the third must be determined by bandstructure calculations or alternative experimentation. The assumption that $R_{2\mathrm{T}} \gg R_{1\mathrm{T}}$ means that our model can give no information about $R_{1\mathrm{T}}$, it must be a free parameter in the final numerical fit but is guided by the step curvature at the beginning of the step as discussed previously.

The final parameter to determine is the spin relaxation time on the island. Comparing the spin relaxation rate in (5.9) to the island throughput rate $\Gamma^{-}_{2\uparrow}(N_0)$, we see that the system time scale $\tau_{\mathrm{s}} = e^2 R_{2\uparrow} D_{\uparrow} \Omega$ defines whether the spin lifetime is long or short. This is similar to expressions surmised in earlier works through physical considerations

[228]. For $\tau_r \ll \tau_s$ there is no spin accumulation, for $\tau_r \gg \tau_s$ the spin accumulation saturates. If a system is designed to find $\tau_r$, the parameters must be setup such that $\tau_r \sim \tau_s$. In the majority of the cases, measurements like these will simply indicate whether $\tau_r$ is shorter or longer than $\tau_s$.

## 5.5 Gate effects

For the experiments in this thesis, which are in the double tunnel junction geometry, varying the junction bias is more convenient. For a set-up in the single electron transistor configuration often varying the gate bias can be easier. The theory developed above readily translates to the single electron transistor case. Rewriting the energies to take into account a back-gate induced charge $C_g V_g$, we find [156]:

$$\begin{aligned} \Delta U_1^{\pm} &= \frac{e^2}{C}\left(\frac{1}{2} \pm \left(-\frac{(C_2+C_g)V}{e} - \frac{C_g V_g}{e} + N - Q_0\right)\right) \pm \Delta E_\sigma \\ \Delta U_2^{\pm} &= \frac{e^2}{C}\left(\frac{1}{2} \pm \left(\frac{C_1 V}{e} + \frac{C_g V_g}{e} + N - Q_0\right)\right) \pm \Delta E_\sigma. \end{aligned} \tag{5.15}$$

Since $R_{2T} \gg R_{1T}$ junction 2 is the current limiting rate. For this energy change we see that changing $C_g V_g$ is equivalent to changing the background charge $Q_0$ of the double tunnel junction formula. Outside of the Coulomb blockade regime this is simply a translation of the steps. A full numerical simulation in the $V$-$V_g$ plane is shown in Fig. 5.4 (a), this has no spin polarisation ($P_2 = 1$). Conductance is given a colourmap in units of $\Omega^{-1}$, the white diamonds indicate the Coulomb blockade where conductance is zero. Comparing this to Fig. 5.4 (b), with the same parameters but a high spin polarisation ($P_2 = 0.1$) the difference is clear. The blue and red areas come from the A and B regions respectively. The position of the minimum in each bias step is linearly translated by the gate voltage.

## 5.6 Tunnel magnetoresistance and spin polarization

In the model given, we considered a double tunnel barrier structure with an arbitrary magnetic configuration. If two or three of the conducting components are ferromagnetic then a magnetoresistance signal will be measured as each component passes through its coercive field. The oscillating TMR($V$) has been examined in previous papers by numerical and experimental study, in general the TMR was found to have a constant

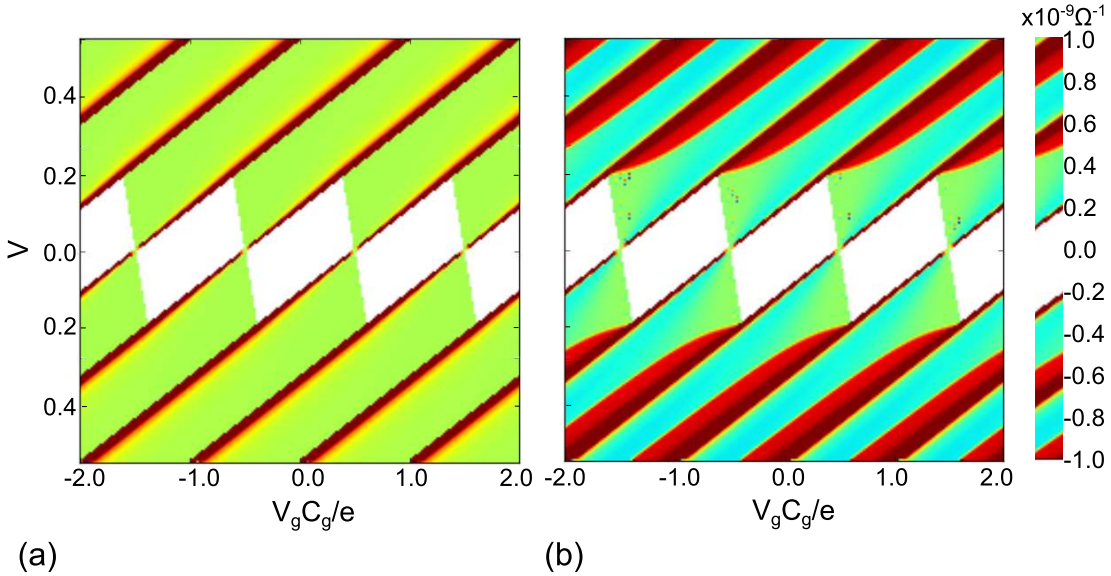


**Figure 5.4:** Numerical simulation of conductance in the SET geometry. (a) has no spin accumulation with $P_2 = 1$, the Coulomb blockade diamonds are highlighted in white. (b) has $P_2 = 0.1$, the spin accumulation is clear, red and turquoise regions highlighting the system in A and B/C regions respectively. All parameters other than $P_2$ are held, these were $R_{2\mathrm{T}} = 1$ GΩ, $R_{2\mathrm{T}}/R_{1\mathrm{T}} = 500$, $C_1 = 0.1$ aF, $C_2 = 0.8$ aF, $P_1 = 1$, $T = 0$, $\tau_\mathrm{r} \gg \tau_\mathrm{s}$

offset and an oscillating component [123; 226]. Using the model developed in this chapter we can now derive the shape and origin these two components.

The constant offset part ($\mathrm{TMR_c}$) is caused by a difference in the average gradient of the Coulomb staircase for the parallel and antiparallel state, the average gradient was shown earlier to be $\mathrm{d}I/\mathrm{d}V_\mathrm{ave} = (R_{2\mathrm{T}})^{-1}$ (see Fig. 5.3(b)). This offset TMR will be reached at step edges when spin modifications to the Coulomb staircase are at a minimum, it can be calculated as $\mathrm{TMR_c} = (R^\mathrm{AP}_{2\mathrm{T}} - R^\mathrm{P}_{2\mathrm{T}})/R^\mathrm{P}_{2\mathrm{T}}$. Thus the baseline TMR is governed by the TMR of the most resistive junction. If the spin dependence in the tunnel matrix element comes purely from the spin dependence of the densities of states, this can be derived in terms of $D_\mathrm{r}$ and $D_E$, the ratios of densities of states in nanoparticle and electrode 2 respectively, as

$$\mathrm{TMR_c} = \frac{D_E D_\mathrm{r} + 1}{D_E + D_\mathrm{r}} - 1. \tag{5.16}$$

This equation is essentially the well-known Julliere formula expressed in a different form [30].

The oscillating component $\mathrm{TMR_o}$ is caused by the different spin accumulation induced changes to the steps in the parallel and anti-parallel states. We found earlier the steps were approximately triangular in shape with the peak at position $v_\mathrm{m}$ and initial gradient $\mathrm{d}I/\mathrm{d}V_\mathrm{A}$. The TMR correspondingly will have the approximate function of the subtraction of two triangles, see Fig 5.5. The two abrupt changes in gradients will be at $v_\mathrm{m}^\mathrm{P}$ and $v_\mathrm{m}^\mathrm{AP}$. Using these values and rearranging (5.12) the $Q^\alpha$ ($\alpha = \mathrm{P}, \mathrm{AP}$) can be calculated in terms of $D_\mathrm{r}$ as

$$Q^\alpha = \begin{cases} \left(v_\mathrm{m}^\alpha(1+D_\mathrm{r}) - D_\mathrm{r}\right)^{-1}, & Q > 1 \\ \left(v_\mathrm{m}^\alpha(1+D_\mathrm{r}) - 1\right)/D_\mathrm{r}, & Q < 1 \end{cases} \tag{5.17}$$

giving quick experimental access to the spin asymmetries in the two states. Fig. 5.5 gives an example showing the calculation of these various factors using data simulated by a full numerical calculation.

Previous literature has focussed on TMR measurements in junction configurations containing more than one magnetic element. Nevertheless, it has been long known that spin accumulation effects can take place when only one magnetic element is present [233]. We will now concentrate on spin-injection through a non-magnetic nanoparticle, in a system with a single ferromagnetic electrode (electrode 2). This automatically simplifies the measurement in two ways. First, since the only FM in the system is electrode 2 we already have that $P_1 = D_\mathrm{r} = 1$, so that $P_2 = 1/Q$ is the only spin parameter to determine. The second advantage of non-magnetic particles is the naturally long spin lifetime they possess and the flexibility for material choice for production of the particles. Making the arbitrary axis choice $P_2 < 1$ and rearranging (5.12) gives $P_2$ in terms of the measurable quantity $v_\mathrm{m}$ as

$$P_2 = 2v_\mathrm{m} - 1. \tag{5.18}$$

This is true for all steps so an average of the $v_\mathrm{m}$'s measured would be used to calculate $P_2$ in practise. All of the quantities in $\mathrm{d}I/\mathrm{d}V_\mathrm{A}$ (5.14) are now known, so this quantity can serve as a check or accuracy improvement on any of the barrier parameters. Using equations (5.1-5.7) combined with the spin accumulation in region A (5.11), the spin polarization injected into electrode 1 in region A is calculated as

$$\begin{aligned} \mathrm{SP} &= \frac{I_\uparrow - I_\downarrow}{I_\uparrow + I_\downarrow} \\ &= \frac{1-P_2}{1+P_2} \times \frac{A-B}{A - B((1-P_2)/(1+P_2))^2} \end{aligned} \tag{5.19}$$

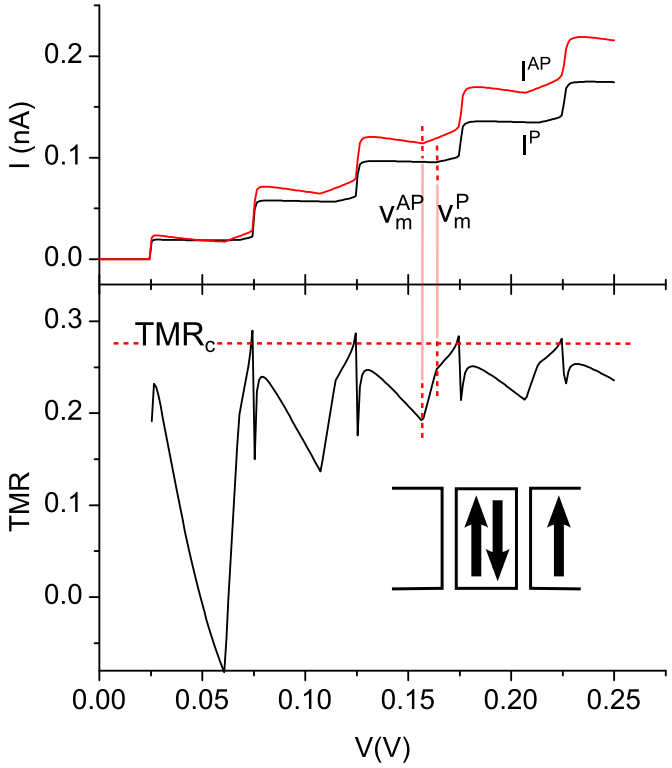


**Figure 5.5:** Voltage bias dependence of current $I(V)$ (top) and TMR($V$) (bottom) for a NM/FM/FM junction. The TMR oscillates within the step returning to the $\mathrm{TMR_c}$ value given by $R_{2\mathrm{T}}^{\mathrm{AP}}/R_{2\mathrm{T}}^{\mathrm{P}} - 1 = 0.27$. TMR gradient changes are observed at the marked $v_{\mathrm{m}}^{\alpha}$ positions. Parameters used $R_{2\mathrm{T}}^{\mathrm{P}} = 1$ GΩ, $P_2^{\mathrm{AP}} = 4$, $P_2^{\mathrm{P}} = 8$, $D_{\mathrm{r}}$=0.7, $P_1^{\mathrm{P}} = 1/P_1^{\mathrm{AP}} = D_{\mathrm{r}}$, $R_{2\mathrm{T}}^{\mathrm{P}}/R_{1\mathrm{T}} = 500$, $C_1 = 0.2$ aF, $C_2 = 3.2$ aF. The inset in the TMR data shows the magnetic configuration of the system.

where

$$A = (R_{2\mathrm{T}}C)^{-1}\left(C_2V_0 + C_1V + \frac{e}{2}(1-\mathrm{sgn}(V))\right), \text{ and}$$
$$B = \frac{2E_{\mathrm{C}}\delta}{eR_{2\mathrm{T}}}.$$

At the beginning of the step when $\delta$ is small the spin polarization simplifies to $\mathrm{SP} = (1-P_2)/(1+P_2)$, which is dependent on just one well-known parameter and equal to the spin polarization of the most resistive junction. At other points in the step the spin polarization oscillates away from this quantity towards zero, though less so for $P_2 \ll 1$. A numerical calculation of the spin polarization is shown in Fig. 5.6 along with a dashed line indicating the predicted maximum spin polarization. This result

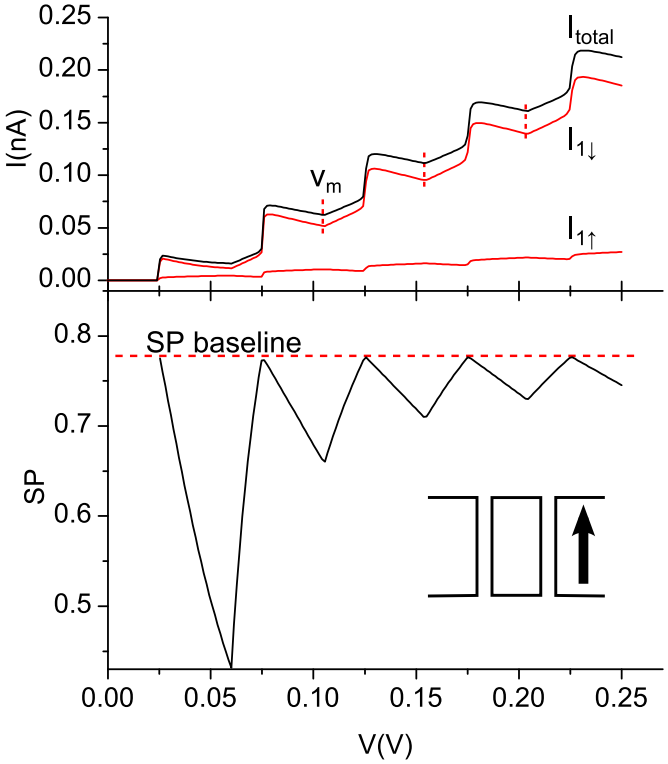


**Figure 5.6:** Voltage bias dependence of current (top) and spin polarization (bottom) for a NM/NM/FM junction with a single ferromagnetic electrode. The spin polarization oscillates, returning to the predicted baseline $(1 - P_2)/(1 + P_2) = 0.78$ at the beginning of each step. The $v_{\mathrm{m}}$ positions as predicted by $v_{\mathrm{m}} = 1/2(1 + P_2)$ are marked and agree with the actual positions of the inner step peaks. Parameters used $R_{2\mathrm{T}} = 1$ GΩ, $R_{2\mathrm{T}}/R_{1\mathrm{T}} = 500$, $C_1 = 0.2$ aF, $C_2 = 3.2$ aF, $P_2 = 1/8$.

suggests that a non-magnetic island and electrode can be used as a method to measure the tunnel spin polarization of a ferromagnetic material by contacting a specimen of that material through a high resistance tunnel barrier and analyzing the measured $I(V)$ curve. This relaxes the low temperature constraint of the well-known Meservey-Tedrow method [234], which has to be carried out well below the critical temperature of an Al superconducting counter-electrode, *i.e.* at temperatures no greater then a few hundred mK. Here the measurement can be performed up to any temperature where the features of the spin-modified Coulomb blockade staircase can still be discerned. Coulomb blockade phenomena can be observed up to room temperature [235].

The spin polarization and the TMR share similarities, both consist of a constant

offset level determined by the most resistive junction, along with oscillations caused by the spin accumulation step modification.

## 5.7 Conclusion

We have found an approximate analytical solution to the magnetic single-electron double tunnel junction. Using this we showed that the system parameters $Q_0$, $R_{i\mathrm{T}}$, $C_{\mathrm{i}}$ and that two of the three polarisation parameters $P_{\mathrm{i}}$ and $D_{\mathrm{r}}$ could be determined from a single $I(V)$ sweep with no applied magnetic field. This was shown for the case of bias modulation and also gate modulation in the case of a single electron transistor geometry.

The solution was further used to predict and interpret the TMR and spin polarization curves as $V$ varies, in systems with multiple magnetic elements and with just a single magnetic electrode. It was found that they follow a baseline, governed by the most resistive junction, with oscillations within the step caused by the build up of spin accumulation in the nanoparticle. It is also clear from the analysis that the parameters of the barriers, including spin polarizations, are in general better modelled through $I(V)$ than TMR($V$) type measurements.

# Chapter 6

STM investigation of DMTJs

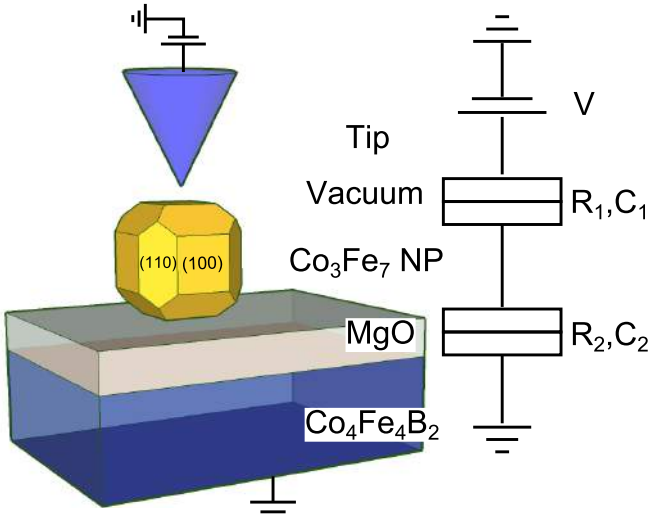


**Figure 6.1:** Diagram of the STM setup with the probe able to make topographical and electrical characterisation. Equivalent circuit diagram shown on right.

One of the ultimate aims of this research was that we would be able to create and study a double tunnel junction structure incorporating just a single nanoparticle. This chapter will describe the progress we have made in this aim using scanning tunnelling microscopy (STM) and spectroscopy (STS).

Fig. 6.1 shows the basic set up of the DMTJ measurement structure, including the equivalent circuit diagram. The magnetic nanoparticle is initially separated from a bottom magnetic electrode by an MgO tunnel barrier. The STM tip plays an integral part in the structure, acting as a second (non-magnetic) electrode. In STS the tip is held still, the tip bias varied and the transport current through to the bottom electrode recorded. The tip/particle barrier width can be adjusted by manipulating the scanning feedback settings.

The system is quite complex with a number of physical components to take account of. This chapter will describe the samples and basic characterisation; it will then build up from STS results obtained with just a vacuum barrier between tip and CoFeB, then a double barrier and finally the full system including a nanoparticle.

## 6.1 Sample and measurement set up

Similarly to the samples fabricated in chapter 4, the bottom electrode was grown as a standard half tunnel junction stack: $SiO_2$(substrate)/Ta(7nm)/Ru(28nm)/ Ta(7nm)/ $Co_{40}Fe_{40}B_{20}$(4nm)/MgO(1.1nm). $Co_{30}Fe_{70}$ nanoparticles were then deposited onto this stack using the gas aggregation source in the sputter chamber (base pressure of $10^{-5}$ Pa). A nominal particle density of ≈100 $\mu m^{-2}$ was grown, allowing for clear individual particle imaging. The distribution of particle diameters was extended to maximum using the quadrupole, this was to maximise the variety of particles available for study by STM on a single sample. AFM scans showed the particle diameters to range over 2-11 nm.

The transfer process to the STM was enacted by a small portable vacuum chamber with a pressure ≈$10^{-6}$ Pa. The substrates were initially cut to a 2×8 mm size and screwed firmly into a standard Omicron STM cooling plate, this was then attached to an adaptor making it compatible with the sputterer substrate holders. The greatest base pressure that the particles are subjected to throughout the transfer process is that of the growth chamber (≈1 hr exposure). XAS measurements shown in chapter 4 demonstrated that particles exposed to this vacuum pressure were not oxidised, the chemical purity is further confirmed by STS measurements.

### 6.1.1 TEM characterisation

Transmission electron microscopy was performed in relief and in cross-section. For plan view the nanoparticles were grown on an amorphous holey carbon membrane, a 2 nm Ta cap was necessary in order to prevent particle oxidation during the atmospheric transfer.

Fig. 6.2 (a) shows a plan view image of a nanoparticle in such a stack. The particles have undergone Wulff reconstruction during the deposition process, leaving twelve hexagonal (110) and four square (100) type faces. This is a typical shape for this type and size of particle [215; 236]. The (110) face sizes vary, the width can be up to 20% of the full particle diameter, the example shown is a particularly cubic particle with mainly (100) faces. The FFT image inset confirms the particle is bcc crystalline, as expected for CoFe with a Co atomic fraction below 70% [220]. The particle has a lattice parameter of $2.9 \pm 0.1$ Å, which agrees with the accepted value of 2.87 Å.

Cross-section imaging was performed on a full stack that had been ion milled as

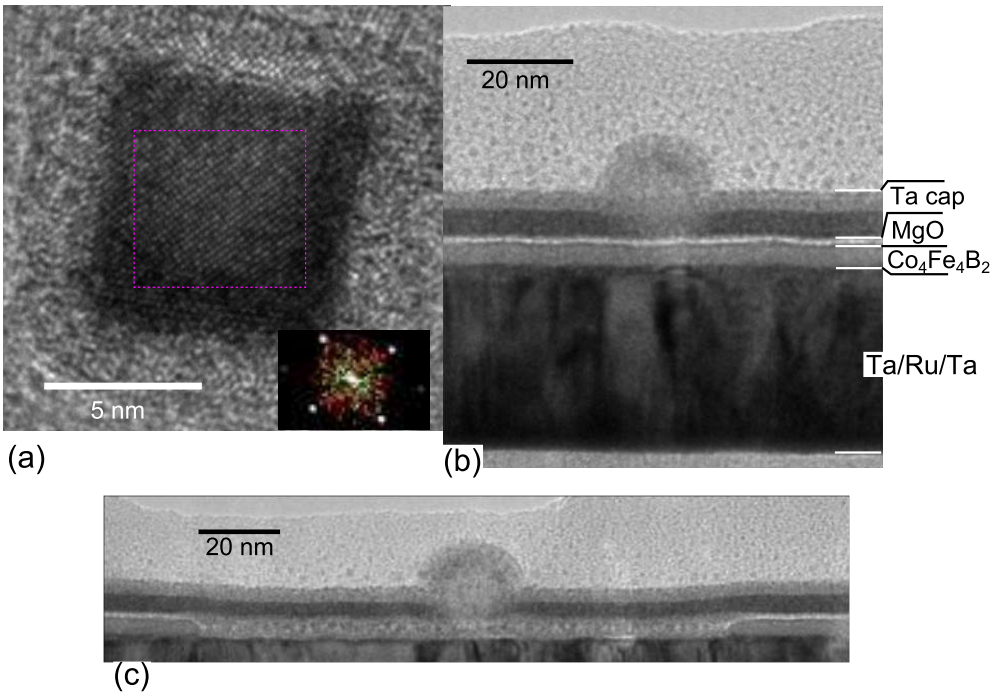


**Figure 6.2:** Plan view (a) and cross-section (b),(c) TEM micrographs of nanoparticles. Insert on (a) shows FFT of region highlighted in pink.

described in section 3.3.2. An example resulting image is shown in Fig. 6.2 (b), the stack layers are labelled on the right. The Ta cap oxidation has passivated, protecting the sample. The nanoparticle is clearly visible though appears larger than it actually is due to the Ta cap. The ruthenium is seen to have columnar growth, with approximately 10 nm diameter grains. High resolution images of the Ru show the expected hexagonal lattice structure with lattice parameter within 0.5% of accepted values. Within the limits of the technique the particle is not seen to have flattened or distorted on deposition.

Initially there was a worry that the particles might destroy the thin MgO barrier as they are deposited. Molecular-dynamics simulations have shown that particles with kinetic energy greater than 1 eV per atom are likely to undergo significant distortion on impact and to damage the surface [186]. Our particles are expected to thermally equalise with the approximately room temperature inert gas mix before deposition. The dynamics are complex but the nanoparticles are expected to have kinetic energies less than $k_BT = 26$ meV [237], well below the limit for damage. The cross-section shown in Fig. 6.2 (b) shows the MgO barrier as complete and with uniform thickness below the particle. This was variable, Fig. 6.2 (c) shows an example where the barrier has completely erupted below the particle. Of a sampling of twenty deposited particles, 60% had a complete undamaged MgO barrier below. Within the statistics available this was not correlated to the size of the particle. This is not thought to be a problem for transport measurements, only the complete structures should show single electron effects. The MgO barrier thickness confirmed expectations from x-ray reflectivity calibrations.

It is perhaps worth noting that a crystalline CoFe/MgO/CoFe tunnel junction is expected to show the large spin polarisation and TMR that has previously been famously predicted [35]. This is expected to be weak in our structures because the amorphous CoFeB electrode has not been annealed, any MgO texture within the nanoparticle region will make a difference however [238].

### 6.1.2 SPM characterisation of CoFeB electrode

A topographic STM scan taken on $Co_{40}Fe_{40}B_{20}$ (CFB) is shown in Fig. 6.3(a). The sample is produced and transferred in the same manner as the other samples in this chapter, the nanoparticles and MgO layer are left out. The image shows a granular

structure with an average grain size of 8.6 nm and an average rms roughness of 0.5±0.1 nm. Atomic force microscopy images of the same structure are shown in Fig. 6.3(b), the grains cannot be seen and the surface is much smoother with an rms roughness of 0.12 nm. The origin of the grain structure in the STM topography is unknown but since it is not seen in AFM is likely to be as a result of changes in the electronic structure rather than topography. This particular alloy of CoFeB should be amorphous and smooth due to the addition of the boron, the grain structure is likely to be caused by the underlying layers, this accords with the average Ru grain size seen in the cross-sectional TEM images of the layers. The CFB is of a similar quality to that used in STM studies from other groups producing high quality MgO tunnel junctions [238]. The spectroscopy scan shown in Fig. 6.3(c) is typical for metal: linear and featureless [239]. The MOKE loop data in (d) shows a very square loop with a coercive field of 0.35 mT.

## 6.2 Scanning tunnelling spectroscopy on MgO

STM on oxides is much more difficult, electrons have to tunnel further and the tip is much more sensitive to defects in the oxide. Topographic and spectroscopic scans over the MgO are shown in Fig. 6.4. The topographic scan in (a), taken at feedback settings of 4 V and 0.1 nA, shows an rms roughness of 0.7 nm, a little rougher than the CFB below as expected. The images show what look like grains with a diameter of 2.6 nm and a standard deviation of 0.4 nm. Fig. 6.4 (b) shows a TEM micrograph of a similar sample grown onto an amorphous carbon window, the MgO is polycrystalline: pink circles highlight areas of continuous crystal and these are seen to be a similar size to the grain feature seen in STM. The defects at crystal boundaries are likely to be the cause of grains seen in STM.

The feedback settings here have been kept at a high voltage and low current because the electrons must tunnel further through the barrier. The voltage in particular is important for oxides, whether it is set above or below the band gap of MgO should make an important difference. Fig. 6.4(c) and (d) show an energy diagram of the situation. The red arrow indicates the tunnelling path of electrons from the tip Fermi energy, the conduction band (CB) and valence band (VB) in the MgO are indicated. The barrier heights of the vacuum and MgO are labelled as $\phi_{\mathrm{vac}}$ and $\phi_{\mathrm{MgO}}$ respectively. Good quality images cannot be easily obtained for $eV < \phi_{\mathrm{MgO}}$. The resistance is so

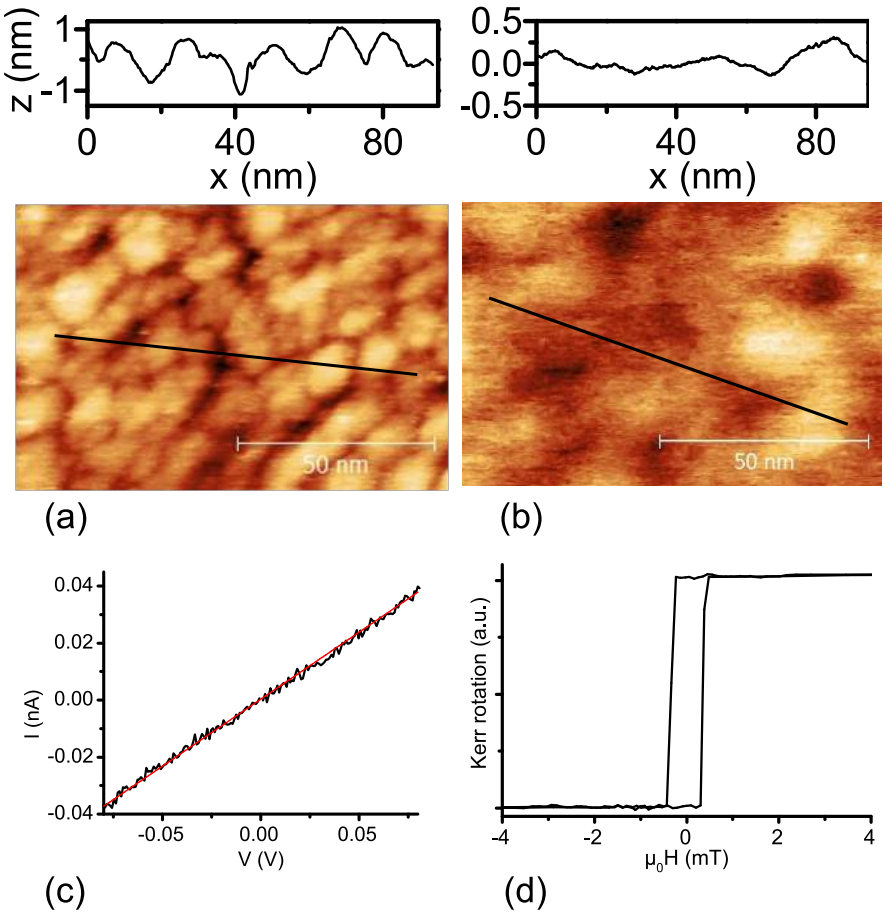


**Figure 6.3:** (a) and (b) show STM and AFM topography scans respectively on CoFeB. Cross-sections along the lines marked are given above. Feedback settings for the STM were 1.2V 0.5nA. (c) an STS spectra on the metal surface, showing the expected linear I-V. (d) a MOKE loop on the CFB showing a square hysteresis with a coercive field of 0.35 mT

high that the tip has a tendency to move into the physical oxide layer itself to obtain the required tunnelling current. This destroys the tip and produces poor images. Above this value we see a triangular barrier and the tunnelling is in the Fowler-Nordheim (FN) regime.

The bandgap of MgO then is important, but the question is where does it occur when doing STM measurements? The width will in general be lower than the bulk value of 7.8 eV for a thin film [240], and will also tend to be smeared out due to band bending effects at the edge of the oxide [241]. The inset graph of Fig. 6.4(e) shows 20 averaged spectroscopy scans taken successively at the same point, the main figure left axis shows the same plot but with absolute values taken of current. The data is fitted with the high $V$ Simmon's model (i.e. Fowler-Nordheim type tunnelling), the fit overlaid in red. The fitting parameters used were barrier width $d = 1.4$ nm, $\phi_{\mathrm{MgO}} = 1.1$ eV. These fit well on both negative and positive bias regions, indicating the bandgap to be reasonably symmetric about the MgO Fermi energy. Pink dashed lines indicate where this barrier position would be. For applied bias less than this value, the current is below the noise level of the measurement.

As explained in section 2.1.4, the Fowler-Nordheim theory assumes a square barrier with an average height distorted to a trapezium by the applied bias. As the barrier width varies the current $I$ follows the exponential relationship $I \propto V^2 \exp(A/V)$, with $A$ a constant dependent on barrier height and width. In the case of the double barrier the situation is more complicated. The relative dielectric constant for bulk MgO is 9.8, so that the majority of the potential is dropped across the vacuum portion of the barrier. The reduced electric field in the dielectric material means that the fitted barrier parameter could be up to a factor of ten too small. The actual value is difficult to determine because the dielectric constant in such a thin film of MgO is likely to be reduced compared to bulk [242]. Also these barriers will not be square as pictured, they will be lowered and rounded by image charge effects [138; 243]. A value intermediate between 1 and 10 eV is expected and this roughly concurs with z-V spectroscopy scans shown in Fig. 6.4(f). These are taken with the feedback on and a constant current maintained. An average of 20 scans is shown, a distinct change in gradient is observed at approximately 3 V. The discontinuous change in the second differential indicates a distinct change in the bandstructure, like a bandgap. The bandwidths observed concur with values seen in similar studies using STM [243], though in the case of very high

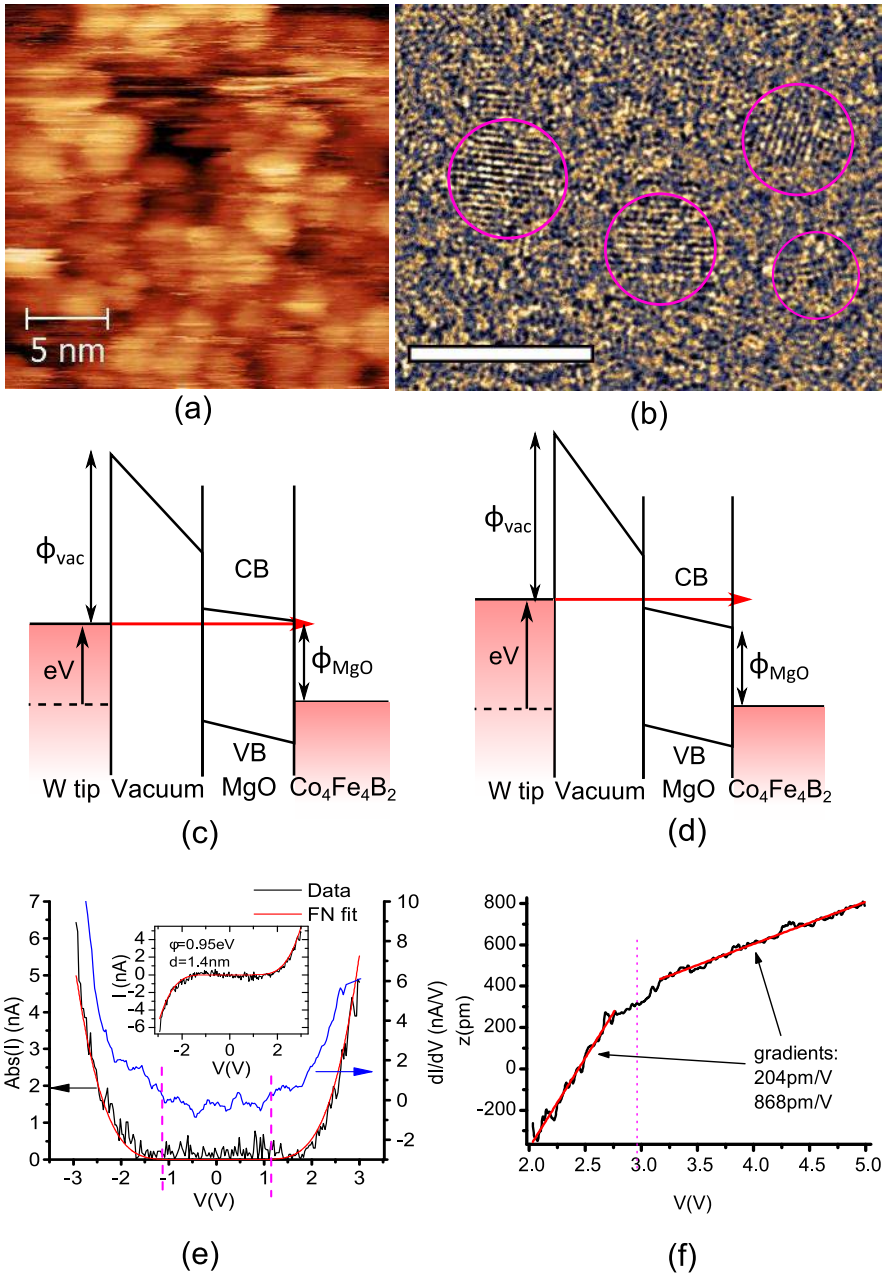


**Figure 6.4:** Results from scans on a 1.4 nm MgO barrier. (a) shows a topography scan, the rms roughness is 0.7 nm and the grain size is 2.6 nm. (b) is a TEM micrograph of a similar structure, the inset scale bar is 5nm and the pink circles outline areas of continuous crystal, these are the same size as the STM grains indicating a defect origin. (c) and (d) are energy diagrams of the situation, abrupt change in conductivity should be seen at the band edge. (e) is an I-V spectroscopic scan on MgO. The Simmons fit in red indicates a barrier height of 1.1 eV. (f) showing z-V spectroscopy, indicates a band edge at 3 V.

quality monolayer MgO, much higher bandgaps can be observed [125; 244; 245].

In general the best images of clusters on MgO were taken with high feedback settings greater than 2.5 V. In order to do spectroscopic measurements however, the tip has to be close to the cluster for reasons that will be described further in later sections, therefore a balance is required.

## 6.3 STM and STS characterisation of nanoparticles: single electron characteristics

### 6.3.1 Particle imaging

In the following sections we will discuss scans and spectroscopy taken over the full half tunnel junction stack with deposited nanoparticles. An image of particles is shown in Fig. 6.5 taken at 4 V, 1 nA feedback. As explained in the previous section, the high voltage is above the MgO bandgap, which prevents the tip from interacting with the surface when scanning around nanoparticles. While imaging over the nanoparticles, this barrier is not such an issue. The island provides a hopping point for the electrons, splitting the vacuum and MgO barriers into two smaller barriers in series. Images can be taken at lower feedback settings but tend to be noisier and damage the tip relatively quickly.

The cross-section shown in the lower portion of Fig. 6.5 (a) shows particle heights 6-7 nm as expected from growth conditions and AFM calibration. The width of the nanoparticles is approximately 20 nm, this lateral size extension is due to convolution with the tip end shape. The relatively large particles (for STM) mean that a large part of the tip is imaged. The tip size concurs with the approximate values found from fitting field emission curves during tip etching ($\sim$20 nm radius, see section 3.5.3). This is the reason a low density of particles is grown, for higher densities the tip may interact with several particles at once, though the particles remain electrically separated. It is also the reason that a tip tool was built to anneal W tips in vacuum. The reliable conical end shape of the etched W tip was necessary in order to be sure of imaging a single particle at a time. The multiple shards at the end of a mechanically cut Pt tip (any within 5 nm of the surface) are all imaged by the same particle confusing the image.

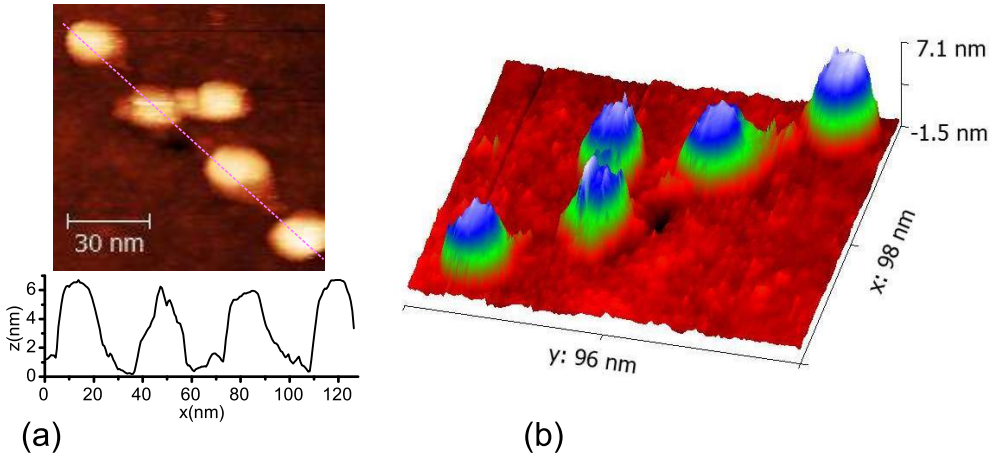


**Figure 6.5:** STM topography of nanoparticles shown mapped in (a) and as a contour plot in (b). The cross-section in (a) is marked in pink. Tip convolution effects mean the particles appear larger than would be expected given their heights.

### 6.3.2 Single electron effects

Fig. 6.6 (a) shows a STS scan taken over a nanoparticle. The I-V is clearly nonlinear, it is in the field emission regime for any appreciable current. Though subtle a periodically stepped gradient is convoluted with the field emission shape, this is seen more clearly in the differential plotted in blue. This is attributed to a Coulomb staircase since it is only seen when scanning over particles. Taking advantage of the STM's ability to scan several different particles on the same sample, Fig. 6.6 (b) shows a plot of the staircase reciprocal step widths $1/\Delta V$ against cluster diameter determined by an STM topographic scan. On the right side of the graph the step width scale is translated into a capacitance for the MgO barrier as $C_2 = e/\Delta V$ (the choice of MgO barrier over vacuum barrier capacitance will be discussed later). There is a clear positive correlation between diameter and capacitance. Roughly speaking this is to be expected if we model the junction as a parallel plate capacitor with area $D^2$ ($D = 7$ nm the particle diameter) and width $d_{\mathrm{MgO}} = 1.4$ nm. Using $\epsilon_{\mathrm{r}}$=5, the capacitance $C_2 = \epsilon_0 \epsilon_{\mathrm{r}} D^2 / d_{\mathrm{MgO}} \approx 1.5$ aF. This shows good agreement to the measured values, given the approximate nature of the calculation. The change in capacitance is not as high as would be expected using this model however, the capacitance does not quite double for the range of sizes examined. This could be due to a combination of the simplicity of the model and inaccuracies in measuring the size of the smallest particles relative to the STM noise base.

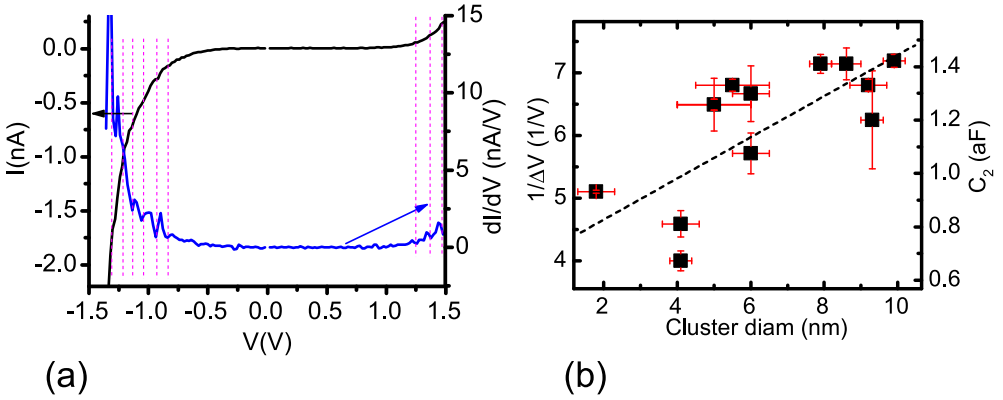


**Figure 6.6:** (a) a I-V spectrum measured over a nanoparticle showing weak Coulomb staircase. The differential is plotted in blue and shows clearer periodicity. The positions of step tops are marked in pink. (b) STS step widths correlated to particle size. The reciprocal step width is converted to capacitance on the right hand axis.

## 6.4 Spin accumulation and field emission modelling of nanoparticle spectroscopy

### 6.4.1 Field emission modelling

In order to characterise the junction beyond the capacitance $C_2$, a full fit to the orthodox single electron theory is required (see section 2.3.1 and chapter 5 for full theoretical details. Notation and symbols in this section follow those defined in previous chapters). A basic Coulomb staircase with no spin accumulation and with $R_2 \gg R_1$ follows the form [61]:

$$I(V) = \frac{1}{R_2 C}\left(C_2 V_0 + C_1 V + \frac{e}{2}(1 - \mathrm{sgn}(V)\right) \tag{6.1}$$

This staircase function is washed out for the case of $C_1 > C_2$. The MgO dielectric means that in our system $C_2 > C_1$. Since the staircase is observed we must have that $R_2 > R_1$. The MgO barrier is therefore the rate controller in this setup, the step width is given by $e/C_2$.

An example staircase with $C_2 = 1$ aF is shown plotted in black in Fig. 6.7 (a). The staircase overlies a linearly increasing background and clearly will not fit the type of non-linear I-V curve measured, an example of which is shown in Fig. 6.7 (b). The error in the assumption we have made in the orthodox theory is that the resistance $R_2$ is constant with applied bias. In fact, due to the field emission effect at these relatively

high voltages, the resistance is changing exponentially with $V$.

The naive way to fix this problem would be to simply replace $R_2 \rightarrow R_2(V) = R_0 \left[V \exp(-0.68\kappa\bar{\varphi} d_{\mathrm{MgO}}/V)\right]^{-1}$ according to the Fowler-Nordheim (FN) equation (2.9), with $R_0$ an arbitrary constant to be fixed by fitting. The background current would then be given by $I(V) = V/R_2(V) \propto V^2 \exp(A/V)$ as required. This model is shown in blue in Fig. 6.7 (a). The non-linear background is now clearly fitting far better to what the data displays. However because of the rapidly increasing gradient, the steps have been washed out nearly completely. This is not consistent with the data in (b) which displays relatively flat step tops.

To understand this problem in more detail we must consider the energy diagram shown in Fig. 6.7 (c). Here the bottleneck of resistance is the MgO barrier ($R_2$). Electrons therefore build up on the nanoparticle, until the chemical potential on the island is just below the tip Fermi energy, at this point there are $N$ excess electron charges on the island. Current proceeds to flow when electrons tunnel out of the island into the CFB (right) electrode, leaving the island in state $N-1$. The island is then quickly topped up by the tip (left) electrode to state $N$ again. Examining this diagram we see now that the largest electric field is across the MgO barrier, contrary to the double barrier situation depicted in Fig. 6.4 (b), where the dielectric forced a large electric field in the vacuum barrier. We see further that the electric field will not be continuous with increasing $V$ but in fact increase stepwise according to the state of the island $N$. We therefore replace $R_2 \rightarrow R_2(N) = R_2(V_2)$ in our model equations. The simulation using this final model is plotted in red in Fig. 6.7 (a). The step tops are now flattened, since while the island is in state $N$, the electric field across the barrier does not change as a function of $V$. This approach broadly follows the theory of Raichev [246]. The theory has been experimentally confirmed by a few groups [247–249], however the data presented here is probably the clearest example of this type of tunnelling in a single metallic particle to date. More complicated effects predicted due to electric charge distribution in the nanoparticle are not observed here.

Finally Fig. 6.7 (d) shows a fit to the data following the $R(V)$ and $R(N)$ models. The $R(N)$ clearly fits the shape of the steps better. In the differential it matches the dips in gradient because of the flatter step tops. The width of the riser is also better fitted though still narrower than the data peak widths, this will be discussed later.

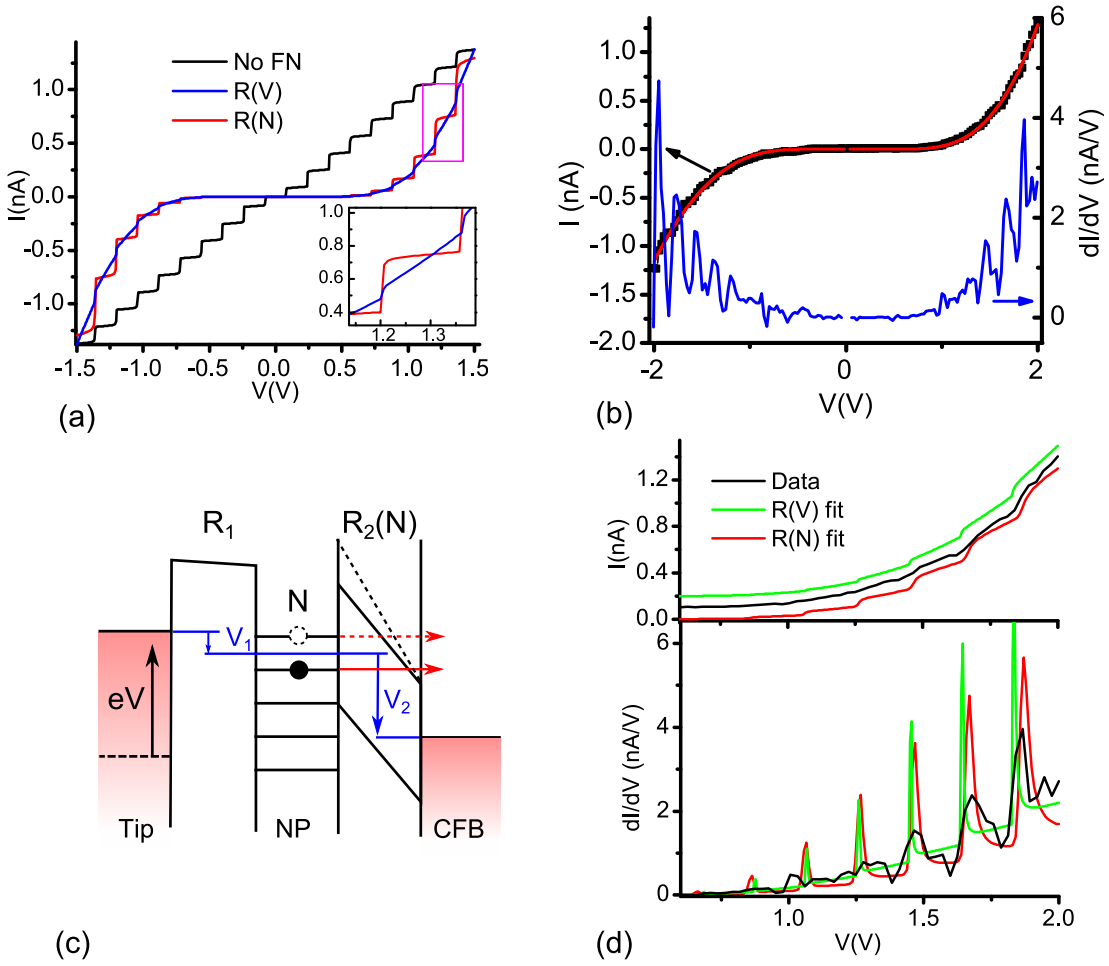


**Figure 6.7:** (a) various simulations according to models described in text. (b) I-V data showing both field emission and Coulomb blockade effects, a Simmons fit is overlaid in red. (c) energy diagram of the DMTJ junction, the majority of the potential is dropped across the MgO barrier. (d) simulations of the data in (b) using the models shown in (a).

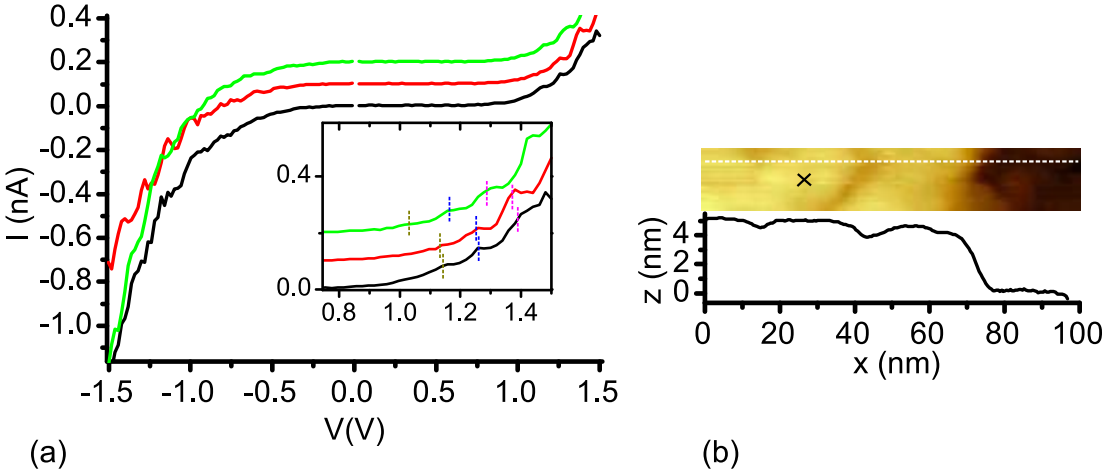


**Figure 6.8:** (a) I-V scans repeated over the same point marked with an × topography scan (b). Inset in (a) is a detailed portion of the same plot with step top variations indicated. The z-profile in (b) is along the dashed line drawn on the topography image.

### 6.4.2 Spin accumulation and barrier polarisations

First we start with a note about the reliability of the spectroscopy on these particles. Because of the mobility of the STM tip and the sensitivity of the tunnelling to the barrier width, the I-V spectra can vary from scan to scan, even when they are taken nominally in the same place. Fig. 6.8 (a) shows three spectra taken sequentially in the same place marked by an × in the image in (b) ($\sim$ 3 s between spectra). There are variations in the tunnelling background profile, the step shape and the phase (offset) of the scans. The period remains constant. This means that the capacitance $C_2$ was relatively stable from scan to scan ($C_2$ is not tip dependent so that makes sense), but that the background charge $Q_0$ is varying by up to $0.2e$. The random variations in $Q_0$ are very commonly seen in single electron experiments [62; 64; 68] and remain one of the major engineering challenges to adopting them for computer logic architectures [52]. Possible sources of variation are local charging, tip reformation or mobile defects such as oxygen vacancies in the MgO [68].

This unrepeatability makes STM unsuitable for TMR type measurements on these particles. Changes in the spectra are not necessarily going to be due to the magnetic field change; subtraction of the spectra will introduce many artefacts. This is probably the reason why no experiment done so far has fully demonstrated single electron effects and spin accumulation using STM. Part of the reason for developing the model

and theory, presented in the previous chapter, was to circumvent this problem. The theory shows that the important factor that indicates the spin accumulation is the step shape on a single Coulomb staircase. Spin accumulation induced either a dip or peak shape into the step tread. TMR style subtraction of staircases actually loses information. Proceeding with this idea we will now demonstrate fitting of spectra to a theory including spin accumulation effects.

While the $R(N)$ field emission model was able to fit spectra with at most a flat step top, it was observed that many of the spectra recorded on the full DMTJ structure showed further reduced or negative gradient within the steps. Furthermore increasing the ratio of $R_2/R_1$ to greater than $10^3$ necessary to cause a flat step makes an extremely vertical step 'riser'. Coulomb staircase spectra displayed a relatively broad transition indicating multiple occupied island levels and a reduced $R_2/R_1$ ratio. Negative gradient and peak step structures can be modelled by a spin accumulation model. Figure 6.9 (a) and (b) show two such example fits, I-V above, differential below. The overall spectrum shape is seen to be replicated well and the dip (or peak on the negative $V$ side) within each step is comparable. The differentials show the specific shape of the gradient changes in the step and the magnitudes and widths are particularly well replicated in the region indicated by purple arrows.

The fit depends on a number of free parameters. The period and offset of the steps are governed by $C_2$ and $Q_0$. These are determined the most accurately and take the values $C_2 = (1.09 \pm 0.01)$ aF, (1.18±0.01) aF and $Q_0 = (0.1 \pm 0.05)e$, $(0.0 \pm 0.05)e$ for (a) and (b) respectively.

$R_2(V_2)$ is a FN profile governed by the barrier height $\phi_{\mathrm{MgO}}$ and width $d_{\mathrm{MgO}}$. $d_{\mathrm{MgO}}$ was fixed at the nominal MgO thickness of 1.4 nm, $\phi_{\mathrm{MgO}}$ was slightly different for positive and negative bias (asymmetric barrier). It was taken at 2.0/3.6 eV for the negative/positive side of (a) and 0.67/2.1 eV for the negative/positive side of (b).

$R_1$ and $C_1$ contain some level of mutual dependence. $C_1$ governs the internal gradient of the step (along with the spin params). $R_1$ governs the initial step gradient and the steepness of the step riser. For (a) the cases could be distinguished and $C_1$ was pinned to $(0.3 \pm 0.1)$ aF ($C_2/C_1 = 3.6$). For (b) the step was found to be flat within the measured gradient so that we can say that $C_2/C_1 > 10$. For both cases $R_1$ was taken as bias independent. It proved the most difficult parameter to fit. As can be seen, peaks in the gradient of the simulation are narrower than the peaks in the data, this is

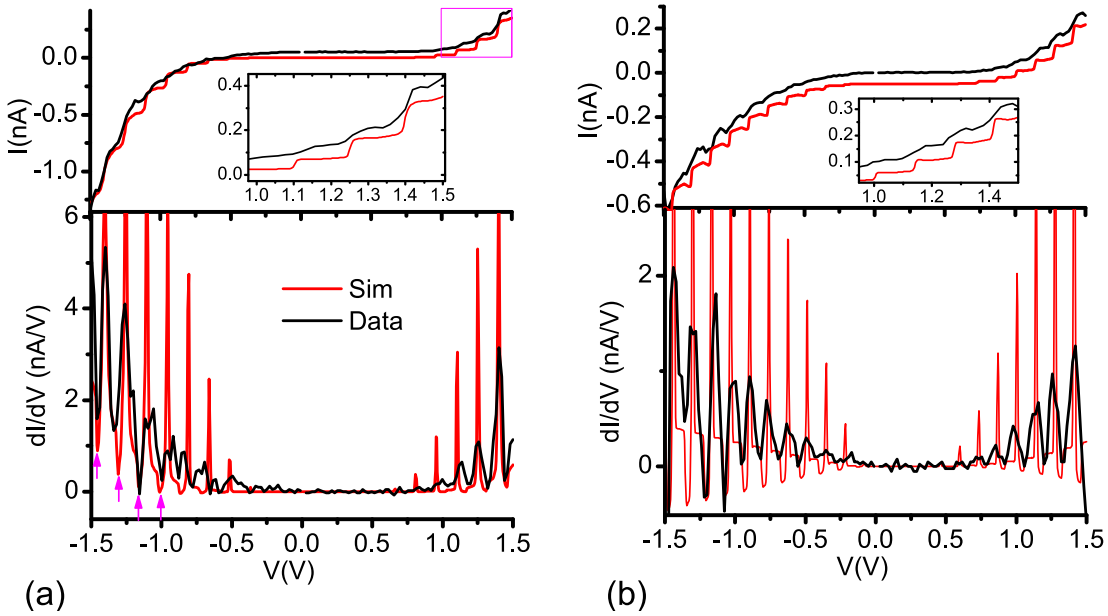


**Figure 6.9:** (a) and (b) show two example fits to STS spectra using a spin accumulation model. See text for details of simulation. The simulation in red is offset from the I-V profile by -50 pA. Insets on the I-V data show detailed portions of the same curves. Numerically differentiated data is plotted in the bottom panel. The experimental conditions for each curve were nominally the same (1.5 V and 0.5 nA feedback).

particularly noticeable in (b). However to increase $R_1$ in the simulation broadens these peaks but also washes out the dips in gradient on the step tops. A balance was struck but there is some mechanism of broadening here that is not taken into account.

The temperature $T$ was fixed at the experimentally measured value of 25 K. Though the step broadening of 2 meV expected for this temperature, is unlikely to make a significant difference to the fit. There are further temperatures in the system that may account for the broadening however, the STM tip is not cooled and likely to be close to 300 K.

The spin parameters $P_\mathrm{i} = R_{\mathrm{i}\uparrow}/R_{\mathrm{i}\downarrow}$ (barrier polarisation ratio) and $D_\uparrow/D_\downarrow = D_r$ (island density of states ratio) are fixed purely by the internal step gradient and peak/trough position. Since the tip is non-magnetic, $P_1$ is driven purely by the density of states ratio on the island and is held at $P_1 = 1/D_r$. This leaves two free spin parameters. The initial staircase gradient is governed by equation (5.14):

$$\left(\frac{\mathrm{d}I}{\mathrm{d}V}\right)_\mathrm{A} = \frac{C_1}{R_{2\mathrm{T}}C} + \frac{C_2}{R_{2\mathrm{T}}C}\frac{(1-Q)(1-D_\mathrm{r}P_2)}{(1+QD_\mathrm{r})(1+P_2)}. \tag{6.2}$$

Within the constraint given, this has significant negative solutions only for $P_2 > 10$ and $P_1 \leq 1$. In fact the staircase troughs are significant enough that in both cases (a) and (b) $P_2 > 10$ but due to the insensitivity of the shape beyond this point, further accuracy cannot be given. For (a) $P_1$ was found to lie between $0.5 < P_1 < 0.8$, and for (b) $0.5 < P_1 < 1$. $P_2 > 10$ can be roughly translated into the traditional magnetic tunnel junction (MTJ) electrode spin polarisation: assuming symmetric spin polarisation on either side of the MgO barrier, $P_2 = R_{2\uparrow}/R_{2\downarrow} \approx (D_\uparrow/D_\downarrow)^2$. This implies a material spin polarisation of $(D_\uparrow - D_\downarrow)/(D_\uparrow + D_\downarrow) = (\sqrt{P_2} - 1)/(\sqrt{P_2} + 1) > 0.5$. This spin polarisation fits well with previous studies on unannealed MgO MTJs [39; 42].

It is perhaps surprising that $P_1$ and $P_2$ are aligned in opposing directions. The vacuum barrier is the simpler of the two junctions, and probably follows the Julliere type model most closely. The MgO junction is more complicated due to the materials present, the polarisation is much more heavily dependent on the barrier and interface electronic states. The polarisation aligned in the opposite direction to the density of states is likely to be caused by the particular arrangement of interface states [250].

Finally we come to the spin relaxation time on the island. Since significant spin accumulation effects have been seen in the DMTJ, the spin relaxation time on the island $\tau_\mathrm{r}$ must far exceed the system timescale $\tau_\mathrm{s} = e^2 R_{2\uparrow} D_\uparrow \Omega$ ($\Omega$ is particle volume) [225]. Using a particle radius of 7 nm, a density of states of $D_\uparrow \approx 0.25$ eV$^{-1}$atom$^{-1}$

[157] and the resistance at the larger applied biases $R_{2\uparrow} = 10$ GΩ, we find $\tau_s \approx 2$ μs. This compares with a bulk spin relaxation time of ≈ 30 fs [251] and previous studies on metallic nanoparticles of 150 ns in Co particles [109] and 1 μs at low voltages in Al particles [33]. This massively extended spin lifetime is due to reduced spin-flip scattering. Mechanisms suggested previously for this have included quantised energy levels suppressing spin-orbit induced spin-flip scattering rates, and reduced magnon scattering due to quantised magnon energy [105; 109; 227]. Both of these effects have comparable energy scales in these particles [105] and are likely to contribute to the lifetime enhancement.

Interestingly we see the spin accumulation effects on the Coulomb staircase are reduced below a bias of 1 V. At this point, due to the increased barrier resistance, the system timescale is $\tau_s \approx 20$ μs. This then is potentially the point at which the system transitions from $\tau_r > \tau_s$ to $\tau_r < \tau_s$. Previous studies have been unable to pin down the spin lifetime accurately due to saturation effects when the system relaxation time is far from the spin lifetime. Here, by dint of the large resistance variation due to field emission effects, we have varied $\tau_s$ over several orders of magnitude and found the spin lifetime to be within an order of magnitude of 10 μs.

## 6.5 Discussion and summary

In this chapter we have built up a full picture of a DMTJ structure as characterised by scanning tunnelling microscopy. Starting from the bottom electrode $Co_{40}Fe_{40}B_{20}$ was shown to have metallic linear spectroscopy and to have a granular topography. TEM indicated that the grains were due to the underlying ruthenium conducting layer.

STM studies on MgO explored the possibilities and difficulties of performing STM on oxide layers. Scanning with feedback settings above the bandgap, granular topography was found, with polycrystalline grains of 2.6 nm average diameter. STS spectra fitted a Simmon's field emission model. It was demonstrated that the fitted barrier height of 1.1 eV was not a good measure of the MgO bandgap due to the electric field structure in the double barrier. Further z-V spectroscopy hinted at a bandgap of 6 eV, closer to the bulk value of 7.8 eV.

Finally STM and STS data were presented on a full stack with deposited $Co_{30}Fe_{70}$ nanoparticles. Cross-sectional TEM confirmed the integrity of the MgO barrier under the majority of deposited particles. STS spectra were found to exhibit Coulomb

staircase like effects. The step widths were correlated with the measured size of the nanoparticle and agreed with a reasonable capacitance predictions.

To simulate the Coulomb staircase STS data, the field emission theory of Raichev [246] was employed, carefully noting that the junction potential was mainly dropped over the MgO barrier. This fit of the data was much improved and is one of the first experimental confirmations of the theory in metallic nanoparticles.

It was found that while reliability of spectra in STM is an issue, it is possible to detect spin effects in a single spectrum. To fully fit the Coulomb staircase a spin accumulation model was employed. This was seen to give a far better fit of the internal step structure. Using results found from the analytical model developed in chapter 5 it was possible to determine or bound many of the barrier parameters including capacitances, resistances and spin polarisations. As predicted, the most detailed information was available for the most resistive barrier (the MgO). The spin polarisation through the vacuum barrier was found to be aligned anti-parallel to that through the MgO barrier, this was attributed to interface effects.

Finally the spin lifetime was discussed and found to be of the order of 10 μs. The field emission profile of the junction uniquely meant that the system spin life time could be varied over several orders of magnitude, pinning down the spin relaxation time in a way that has not been possible in previous studies. Further investigation in this line theoretically and experimentally could prove fruitful.

# Chapter 7

Conclusions

This thesis has described a series of wide ranging experiments characterising magnetic nanoparticles in the 4-14 nm diameter range. These particles are in the fascinating size regime between the quantum and macroscopic world. We have seen that they exhibit novel physical phenomena such as superparamagnetism, partially quenched orbital moments, spin glass like textures, Coulomb blockade, spin accumulation and long spin lifetimes.

Nanospintronics examines the transport and manipulation of spins at the nanoscale, it is a fast growing field of interest [7]. Ever improving nanofabrication technology is opening new doors into contacting isolated nanostructures. Emerging techniques have allowed experiments that have shown unexpected physics, and have often gone hand-in-hand with new theoretical developments. A major theme of this thesis has been to realise the possibility of using scanning tunnelling microscopy to address individual magnetic nanoparticles for electrical transport investigation. Both experimental and theoretical development have been used to address well known problems in spectroscopy of nanoparticles, and have led to discoveries regarding the spin characterisation of barriers and spin relaxation properties of these magnetic particles.

## 7.1 Summary

Magnetic $Co_{30}Fe_{70}$ nanoparticles were grown in vacuum using a gas-aggregation cluster source. They were deposited onto sputtered thin films and thoroughly characterised for their structural, magnetic and electronic transport properties.

The particles were deposited as a bcc crystal with a truncated rhombic dodecahedron shape given by Wulff reconstruction, with the (001) axis oriented out-of-plane. They are ferromagnetic showing both magnetocrystalline and shape anisotropy; the easy axis orients randomly in plane along a (100) axis. Orbital to spin moment ratio was measured for particles 11-14 nm in diameter. For larger particles the orbital moment was found to be close to the quenched bulk value, though the moment quickly increased with decreasing diameter. This NP size range is larger than used in the literature before. Combining all previous data together, the general trend of decreasing orbital moment with size was obeyed, but detailed fitting to a simple two species moment was in bad agreement. For my data this was attributed to the simplicity of the low coordination shell model. Complementary magnetometry studies on these densely packed nanopaticles showed a very wide distribution of anisotropies and a superpara-

magnetic blocking temperature unexpectedly extended well above room temperature. Complex magnetic dipole interactions between the percolated nanoparticles was shown to be the cause, though further study is required to understand the negative correlation between blocking temperature and packing density.

To make use of transport data through double magnetic tunnel junction (DMTJ) stacks, the I-V curve must be simulated using orthodox single electron theory combined with spin accumulation effects. A new analytical solution to existing numerical theory was derived [225]. This was valid under the approximation of highly asymmetric barrier resistance, exactly that which gives the largest single electron effects and also is the most common experimentally. Using this theory, barrier resistances, capacitances and spin polarisations were shown to be independently obtainable by fitting to a single detailed I-V sweep. Further, it was shown that spin accumulation occurred, and could be measured, on the nanoparticle with a single ferromagnetic electrode. Oscillatory TMR type measurements were seen to be unnecessary for measuring spin effects; by subtracting parallel and anti-parallel I-V curves information is lost. This is an important development for the use of STM based nanospintronics, where repeatability can be an issue due to local charging effects varying over time.

Finally STM results were presented on a full DMTJ structure, with asymmetric MgO and vacuum tunnel barriers. Scanning tunnelling spectroscopy showed Coulomb staircase effects, with step widths that scaled with the size of the particle. To fully simulate the data it was necessary to take into account the resistance variation due to field emission effects. Discrete changes in effective barrier width at integral multiples of charging energy, gave a more pronounced Coulomb staircase and were necessary to fit to the spectra. Finally spin accumulation effects were included to fully simulate the data. The fits were found to match well, though certain broadening effects of the experiment have not yet been taken into account. Analytical theory developed earlier allowed all of the barrier parameters to be determined or bounded. Unexpectedly the spin polarisations were found to be oriented anti-parallel. This was attributed to complex interface effects over the MgO barrier. As an added bonus, due to resistance variation caused by field emission effects, the spin relaxation time on the island could be recorded more accurately than previously possible in such a structure. The spin lifetime was found to be greater than 1 μs and within an order of magnitude of 10 μs, far longer than determined previously [109].

## 7.2 Outlook

The most important work here has been the establishment of the STM as a tool for study of DMTJs. The theory that has been developed, showing that the spin accumulation parameters can be determined simply by simulating the I-V spectra with no external magnetic fields present, is very important. This allows focus on the basic transport data provided by the STM which is the STS spectra. It also negates one of the most difficult barriers to nanospintronic investigation using STM, which is the reliability of comparing spectra over time or while varying applied external fields.

Moving forward the priority will be to increase the quality and quantity of data taken on the STM. There are practical barriers still to be overcome, related to the stability and reliability of the STS spectra. The resistance mismatch between tunnelling directly through MgO and through particles means that images tend to be relatively noisy. STM probes can be rapidly damaged by collisions with particles or the insulating barrier. Growing a thinner MgO barrier may be one way to overcome this. Another solution may be to only take images with feedback above the bandgap, well clear of both particle and MgO. For STS in this case, the tip would need to be dropped a finite distance to decrease the vacuum resistance relative to the insulating barrier.

Perhaps some of the most interesting questions still open in nanospintronics are related to the mechanisms of spin relaxation on these nanoislands. In fact, spin lifetime measurements on quantum dots are well established [33; 252; 253], but are more challenging in these larger particles. I think the idea of quantifying the lifetime by studying the Coulomb blockade over a range of resistances, generated by field emission, is very promising for future studies. Being able to accurately determine the spin lifetime in particles of a variety of sizes, materials and at a range of temperatures would provide vital information towards solving these questions.

So far there have been few real world practical applications suggested for these DMTJ devices. Current applications for non-magnetic single electron devices focus on metrology techniques, taking advantage of the sensitive dependence of the Coulomb staircase shape on environmental background charge. In chapter five, I proposed a further metrology method to determine spin polarisation from an FM/tunnel barrier combination. This was experimentally demonstrated in chapter six but could be taken much further using non-magnetic particles. In order for this to be a standard method it cannot rely on a gas-aggregation nanoparticle source being available. A discontinuous

layer of metal grown on oxide is potential route; STM measurements of CB on these types of systems have been particularly reliable in the past [63]. The ability to use non-magnetic, inert materials would also conveniently negate the need for a vacuum transfer system. If this experiment were realised it could prove a valuable new route into the measurement of one of the most fundamental quantities in spintronics.

# References


[1] B. Wakeham, Review of UK Physics, Technical report, Research councils UK (2008), (23% extrapolated from US and UK statistics.) 2

[2] P. J. Mulvey and S. Nicholson, Trends in physics PhDs, Technical report, American Institute of Physics (2014) 2

[3] J. Barnaś and A. Fert, Magnetoresistance oscillations due to charging effects in double ferromagnetic tunnel junctions, *Phys. Rev. Lett.* **80**, 1058 (1998) 2, 83, 85, 91

[4] I. Weymann and J. Barnaś, Transport characteristics of ferromagnetic single-electron transistors, *Phys. status solidi* **236**, 651 (2003) 83, 87

[5] J. Barnaś and I. Weymann, Spin effects in single-electron tunnelling, *J. Phys. Condens. Matter* **20**, 423202 (2008) 2, 83

[6] K. Yakushiji, S. Mitani, F. Ernult, K. Takanashi and H. Fujimori, Spin-dependent tunneling and Coulomb blockade in ferromagnetic nanoparticles, *Phys. Rep.* **451**, 1 (2007) 2, 9

[7] K. J. Dempsey, D. Ciudad and C. H. Marrows, Single electron spintronics., *Philos. Trans. A. Math. Phys. Eng. Sci.* **369**, 3150 (2011) 2, 8, 119

[8] M. Baibich, J. Broto, A. Fert and F. V. Dau, Giant magnetoresistance of (001) Fe/(001) Cr magnetic superlattices, *Phys. Rev. Lett.* **61**, 2472 (1988) 2

[9] G. Binasch, P. Grünberg, F. Saurenbach and W. Zinn, Enhanced magnetoresistance in layered magnetic structures with antiferromagnetic interlayer exchange, *Phys. Rev. B* **39**, 4828 (1989) 2, 3

[10] Z. Bandic and R. Victora, Advances in magnetic data storage technologies, *Proc. IEEE* **96**, 1749 (2008) 3

[11] B. Dieny, Giant magnetoresistance in spin-valve multilayers, *J. Magn. Magn. Mater.* **136**, 335 (1994) 3

[12] S. Parkin, C. Kaiser, A. Panchula, K. Roche and M. Samant, Magnetically engineered spintronic sensors and memory, *Proc. IEEE* **91**, 661 (2003) 3

[13] J. Slaughter, Materials for Magnetoresistive Random Access Memory, *Annu. Rev. Mater. Res.* **39**, 277 (2009) 3

[14] M. Stiles and A. Zangwill, Anatomy of spin-transfer torque, *Phys. Rev. B* **66**, 014407 (2002) 3

[15] L. San Emeterio Alvarez, K.-Y. Wang, S. Lepadatu, S. Landi, S. J. Bending et al., Spin-Transfer-Torque-Assisted Domain-Wall Creep in a Co/Pt Multilayer Wire, *Phys. Rev. Lett.* **104**, 137205 (2010) 3

[16] J. Hirsch, Spin Hall Effect, *Phys. Rev. Lett.* **83**, 1834 (1999) 3

[17] E. Saitoh, M. Ueda, H. Miyajima and G. Tatara, Conversion of spin current into charge current at room temperature: Inverse spin-Hall effect, *Appl. Phys. Lett.* **88**, 182509 (2006)

[18] S. O. Valenzuela and M. Tinkham, Direct electronic measurement of the spin Hall effect., *Nature* **442**, 176 (2006) 3

[19] Y. Bychkov and E. Rashba, Oscillatory effects and the magnetic susceptibility of carriers in inversion layers, *J. Phys. C Solid state phys.* **17**, 6039 (1984) 3

[20] A. Chernyshov, M. Overby, X. Liu, J. K. Furdyna, Y. Lyanda-Geller et al., Evidence for reversible control of magnetization in a ferromagnetic material by means of spin-orbit magnetic field, *Nat. Phys.* **5**, 656 (2009)

[21] I. M. Miron, T. Moore, H. Szambolics, L. D. Buda-Prejbeanu, S. Auffret et al., Fast current-induced domain-wall motion controlled by the Rashba effect., *Nat. Mater.* **10**, 419 (2011)

[22] C. Ciccarelli, K. M. D. Hals, A. Irvine, V. Novak, Y. Tserkovnyak et al., Magnonic charge pumping via spin-orbit coupling., *Nat. Nanotechnol.* pp. 1–5 (2014) 3

[23] G. E. W. Bauer, E. Saitoh and B. J. van Wees, Spin caloritronics., *Nat. Mater.* **11**, 391 (2012) 3

[24] H. Zhang, C.-X. Liu, X.-L. Qi, X. Dai, Z. Fang et al., Topological insulators in Bi2Se3, Bi2Te3 and Sb2Te3 with a single Dirac cone on the surface, *Nat. Phys.* **5**, 438 (2009) 3

[25] S. Heinze, K. von Bergmann, M. Menzel, J. Brede, A. Kubetzka et al., Spontaneous atomic-scale magnetic skyrmion lattice in two dimensions, *Nat. Phys.* **7**, 713 (2011)

[26] X. Z. Yu, Y. Onose, N. Kanazawa, J. H. Park, J. H. Han et al., Real-space observation of a two-dimensional skyrmion crystal., *Nature* **465**, 901 (2010)

[27] P. Sinha, N. A. Porter and C. H. Marrows, Strain-induced effects on the magnetic and electronic properties of epitaxial Fe1-xCoxSi thin films, *Phys. Rev. B* **89**, 134426 (2014) 3

[28] S. Bader and S. Parkin, Spintronics, *Annu. Rev. Condens. Matter Phys.* **1**, 71 (2010) 3

[29] J. Sinova and I. Žutić, New moves of the spintronics tango., *Nat. Mater.* **11**, 368 (2012) 3

[30] M. Julliere, Tunneling between ferromagnetic films, *Phys. Lett. A* **54A**, 225 (1975) 3, 18, 93

[31] T. Miyazaki and N. Tezuka, Giant magnetic tunneling effect in Fe/Al2O3/Fe junction, *J. Mag. Magn. Mater* **139**, L231 (1994) 4

[32] J. Moodera, L. Kinder, T. Wong and R. Meservey, Large magnetoresistance at room temperature in ferromagnetic thin film tunnel junctions, *Phys. Rev. Lett.* **74**, 3273 (1995) 4, 19

[33] Y. G. Wei, C. E. Malec and D. Davidović, Saturation of spin-polarized current in nanometer scale aluminum grains, *Phys. Rev. B* **76**, 195327 (2007) 4, 9, 116, 121

[34] O. Schebaum, V. Drewello, A. Auge, G. Reiss, M. Münzenberg et al., Tunnel magnetoresistance in alumina, magnesia and composite tunnel barrier magnetic tunnel junctions, *J. Magn. Magn. Mater.* **323**, 1525 (2011) 4

[35] W. Butler, X.-G. Zhang, T. Schulthess and J. MacLaren, Spin-dependent tunneling conductance of Fe—MgO—Fe sandwiches, *Phys. Rev. B* **63**, 1 (2001) 4, 19, 102

[36] J. Mathon and a. Umerski, Theory of tunneling magnetoresistance of an epitaxial Fe/MgO/Fe(001) junction, *Phys. Rev. B* **63**, 220403 (2001) 4, 19

[37] S. Yuasa, T. Nagahama, A. Fukushima, Y. Suzuki and K. Ando, Giant room-temperature magnetoresistance in single-crystal Fe/MgO/Fe magnetic tunnel junctions., *Nat. Mater.* **3**, 868 (2004) 4

[38] S. S. P. Parkin, C. Kaiser, A. Panchula, P. M. Rice, B. Hughes et al., Giant tunnelling magnetoresistance at room temperature with MgO (100) tunnel barriers., *Nat. Mater.* **3**, 862 (2004) 4

[39] D. D. Djayaprawira, K. Tsunekawa, M. Nagai, H. Maehara, S. Yamagata et al., 230% room-temperature magnetoresistance in CoFeB/MgO/CoFeB magnetic tunnel junctions, *Appl. Phys. Lett.* **86**, 092502 (2005) 4, 115

[40] S. Ikeda, J. Hayakawa, Y. Ashizawa, Y. M. Lee, K. Miura et al., Tunnel magnetoresistance of 604% at 300K by suppression of Ta diffusion in CoFeB/MgO/CoFeB pseudo-spin-valves annealed at high temperature, *Appl. Phys. Lett.* **93**, 082508 (2008) 4, 20

[41] S. Yuasa and D. D. Djayaprawira, Giant tunnel magnetoresistance in magnetic tunnel junctions with a crystalline MgO(001) barrier, *J. Phys. D. Appl. Phys.* **40**, R337 (2007) 4

[42] S. Ikeda, J. Hayakawa, Y. M. Lee, T. Tanikawa, F. Matsukura et al., Tunnel magnetoresistance in MgO-barrier magnetic tunnel junctions with bcc-CoFe(B) and fcc-CoFe free layers, *J. Appl. Phys.* **99**, 08A907 (2006) 4, 115

[43] I. Giaever and H. Zeller, Superconductivity of small tin particles measured by tunneling, *Phys. Rev. Lett.* **20**, 1504 (1968) 5

[44] H. Zeller and I. Giaever, Tunneling, zero-bias anomalies, and small superconductors, *Phys. Rev.* **181**, 789 (1969)

[45] J. Lambe and R. Jaklevic, Charge-quantization studies using a tunnel capacitor, *Phys. Rev. Lett.* **22**, 1371 (1969)

[46] J. Gittleman, Y. Goldstein and S. Bozowski, Magnetic properties of granular nickel films, *Phys. Rev. B* **5**, 3609 (1972)

[47] J. Helman and B. Abeles, Tunneling of spin-polarized electrons and magnetoresistance in granular Ni films, *Phys. Rev. Lett.* **37**, 1429 (1976) 5

[48] G. J. Dolan, Offset masks for lift-off photoprocessing, *Appl. Phys. Lett.* **31**, 337 (1977) 5

[49] T. Fulton and G. Dolan, Observation of single-electron charging effects in small tunnel junctions, *Phys. Rev. Lett.* **59**, 109 (1987) 5

[50] K. K. Likharev, Correlated discrete transfer of single electrons in ultrasmall tunnel junctions, *IBM J. Res. Dev.* **32**, 144 (1988) 5, 20

[51] D. V. Averin and K. K. Likharev, Coulomb blockade of single-electron tunneling, and coherent oscillations in small tunnel junctions, *J. Low Temp. Phys.* **62**, 345 (1986) 5, 20, 23

[52] K. Likharev, Single-electron devices and their applications, *Proc. IEEE* **87**, 606 (1999) 6, 112

[53] D. Ralph, C. Black and M. Tinkham, Spectroscopic measurements of discrete electronic states in single metal particles, *Phys. Rev. Lett.* **74**, 3241 (1995) 6, 8

[54] Y. Nakamura, C. Chen and J. Tsai, 100-K operation of Al-based single-electron transistors, *Jpn. J. Appl. Phys.* **35**, 1465 (1996) 9, 23

[55] S. Altmeyer, A. Hamidi, B. Spangenberg and H. Kurz, 77 K single electron transistors fabricated with 0.1 $\mu$m technology, *J. Appl. Phys.* **81**, 8118 (1997)

[56] D. Klein, R. Roth, A. Lim, A. Alivisatos and P. McEuen, A single-electron transistor made from a cadmium selenide nanocrystal, *Nature* **389**, 699 (1997) 6

[57] H. Ishikuro, T. Fujii, T. Saraya, G. Hashiguchi, T. Hiramoto et al., Coulomb blockade oscillations at room temperature in a Si quantum wire metal-oxide-semiconductor field-effect transistor fabricated by anisotropic etching on a silicon-on-insulator substrate, *Appl. Phys. Lett.* **68**, 3585 (1996) 6

[58] Y. Takahashi, H. Namatsu, K. Kurihara, K. Iwadate, M. Nagase et al., Size dependence of the characteristics of Si single-electron transistors on SIMOX substrates, *IEEE Trans. Electron Devices* **43**, 1213 (1996)

[59] E. S. Soldatov, V. V. Khanin, A. S. Trifonov, S. P. Gubin, V. V. Kolesov et al., Room Temperature Molecular Single-Electron Transistor, *Phys.-Usp.* **41**, 202 (2008) 6

[60] R. Wilkins, E. Ben-Jacob and R. Jaklevic, Scanning-tunneling-microscope observations of Coulomb blockade and oxide polarization in small metal droplets, *Phys. Rev. Lett.* **63**, 801 (1989) 6, 9

[61] A. Hanna and M. Tinkham, Variation of the Coulomb staircase in a two-junction system by fractional electron charge, *Phys. Rev. B* **44**, 5919 (1991) 21, 23, 87, 109

[62] C. Schönenberger, H. V. Houten, J. Kerkhof and H. Donkersloot, Single-electron tunneling in double-barrier junctions by scanning tunneling microscopy, *App. surf. sci.* **67**, 222 (1993) 112

[63] M. Amman, S. Field and R. Jaklevic, Coulomb-blockade spectroscopy of gold particles imaged with scanning tunneling microscopy, *Phys. Rev. B* **48**, 104 (1993) 122

[64] J. Dubois and E. Verheijen, Scanning-tunneling-microscopy observation of variations of the Coulomb staircase due to charge trapping, *Phys. Rev. B* **48**, 260 (1993) 112

[65] D. Anselmetti and T. Richmond, Single-electron tunnelling at room temperature with adjustable double-barrier junctions, *Europhys. Lett.* **25**, 297 (1994)

[66] J. E. Coury, Characterization of zinc sulfide nanoclusters via atomic force and scanning tunneling microscopy, *J. Vac. Sci. Technol. B Microelectron. Nanom. Struct.* **13**, 1167 (1995)

[67] M. Dorogi, J. Gomez and R. Osifchin, Room-temperature Coulomb blockade from a self-assembled molecular nanostructure, *Phys. Rev. B* **52**, 9071 (1995)

[68] H. van Kempen and J. Dubois, Small metallic particles studied by scanning tunneling microscopy, *Phys. B Condens. Matter* **204**, 51 (1995) 112

[69] R. P. Andres, Room temperature Coulomb blockade and Coulomb staircase from self-assembled nanostructures, *J. Vac. Sci. Technol. A Vacuum, Surfaces, Film.* **14**, 1178 (1996)

[70] C. Brun, K. H. Müller, I.-P. Hong, F. Patthey, C. Flindt et al., Dynamical Coulomb Blockade Observed in Nanosized Electrical Contacts, *Phys. Rev. Lett.* **108**, 126802 (2012) 6, 9

[71] K. Matsumoto, M. Ishii, K. Segawa, Y. Oka, B. J. Vartanian et al., Room temperature operation of a single electron transistor made by the scanning tunneling microscope nanooxidation process for the TiOx/Ti system, *Appl. Phys. Lett.* **68**, 34 (1996) 6

[72] M. Devoret and R. Schoelkopf, Amplifying quantum signals with the single-electron transistor, *Nature* **406**, 1039 (2000) 6

[73] Y. Ono, A. Fujiwara, K. Nishiguchi, H. Inokawa and Y. Takahashi, Manipulation and detection of single electrons for future information processing, *J. Appl. Phys.* **97**, 031101 (2005) 6

[74] S. Ilani, a. Yacoby, D. Mahalu and H. Shtrikman, Microscopic structure of the metal-insulator transition in two dimensions., *Science* **292**, 1354 (2001) 6

[75] J. Martin, N. Akerman, G. Ulbricht, T. Lohmann, J. H. Smet et al., Observation of electron-hole puddles in graphene using a scanning single-electron transistor, *Nat. Phys.* **4**, 144 (2007) 6

[76] J. P. Pekola, J. J. Vartiainen, M. Möttönen, O.-P. Saira, M. Meschke et al., Hybrid single-electron transistor as a source of quantized electric current, *Nat. Phys.* **4**, 120 (2008) 6

[77] R. G. Knobel and A. N. Cleland, Nanometre-scale displacement sensing using a single electron transistor., *Nature* **424**, 291 (2003) 6

[78] A. Cottet, T. Kontos, S. Sahoo, H. T. Man, M.-S. Choi et al., Nanospintronics with carbon nanotubes, *Semicond. Sci. Technol.* **21**, S78 (2006) 6

[79] D. Goldhaber-Gordon and H. Shtrikman, Kondo effect in a single-electron transistor, *Nature* **391**, 1996 (1998) 6

[80] S. J. Shin, J. J. Lee, H. J. Kang, J. B. Choi, S. E. Yang et al., Room-Temperature Charge Stability Modulated by Quantum Effects, *Nano Lett.* **11**, 1591 (2011) 6

[81] M. F. Gonzalez-Zalba, D. Heiss, G. Podd and A. J. Ferguson, Tunable aluminium-gated single electron transistor on a doped silicon-on-insulator etched nanowire, *Appl. Phys. Lett.* **101**, 103504 (2012) 6

[82] C. Black, D. Ralph and M. Tinkham, Spectroscopy of the superconducting gap in individual nanometer-scale aluminum particles., *Phys. Rev. Lett.* **76**, 688 (1996) 6

[83] V. F. Maisi, S. V. Lotkhov, A. Kemppinen, A. Heimes, J. T. Muhonen et al., Excitation of Single Quasiparticles in a Small Superconducting Al Island Connected to Normal-Metal Leads by Tunnel Junctions, *Phys. Rev. Lett.* **111**, 147001 (2013) 6

[84] J. P. Pekola, J. V. Koski and D. V. Averin, Refrigerator based on the Coulomb barrier for single-electron tunneling, *Phys. Rev. B* **89**, 081309 (2014) 6

[85] H. Fujimori, S. Mitani and S. Ohnuma, Tunnel-type GMR in metal-nonmetal granular alloy thin films, *Mater. Sci. Eng. B* **31**, 219 (1995) 7

[86] L. Schelp, a. Fert, F. Fettar, P. Holody, S. Lee et al., Spin-dependent tunneling with Coulomb blockade, *Phys. Rev. B* **56**, R5747 (1997) 7

[87] B. Dieny, S. Sankar, M. McCartney, D. Smith, P. Bayle-Guillemaud et al., Spin-dependent tunneling in discontinuous metal/insulator multilayers, *J. Magn. Magn. Mater.* **185**, 283 (1998) 7

[88] K. Ono, H. Shimada and Y. Ootuka, Enhanced magnetic valve effect and magneto-Coulomb oscillations in ferromagnetic single electron transistor, *J. Phys. Soc. Jpn.* **66**, 1261 (1997) 7

[89] K. Ono, H. Shimada and Y. Ootuka, Ferromagnetic single electron transistor, *Solid. State. Electron.* **42**, 1407 (1998) 7

[90] Y. Ootuka, K. Ono, H. Shimada, R. Matsuda and A. Kanda, Electron transport in ferromagnetic small tunnel junctions, *Mater. Sci. Eng. B* **84**, 114 (2001) 7, 9

[91] S. Iwabuchi, T. Tanamoto and R. Kitawaki, Coulomb blockade and enhancement of magnetoresistance change in ultrasmall ferromagnetic tunnel junctions, *Phys. B Condens. Matter* **249-251**, 276 (1998) 7

[92] S. Takahashi and S. Maekawa, Effect of Coulomb Blockade on Magnetoresistance in Ferromagnetic Tunnel Junctions, *Phys. Rev. Lett.* **80**, 1758 (1998) 7, 83

[93] H. Brückl, G. Reiss, H. Vinzelberg, M. Bertram, I. Mönch et al., Enhanced magnetoresistance of permalloy/Al-oxide/cobalt tunnel junctions in the Coulomb blockade regime, *Phys. Rev. B* **58**, R8893 (1998) 7

[94] H. Sukegawa, S. Nakamura and A. Hirohata, Significant magnetoresistance enhancement due to a cotunneling process in a double tunnel junction with single discontinuous ferromagnetic layer insertion, *Phys. Rev. Lett.* **94**, 068304 (2005)

[95] K. J. Dempsey, A. T. Hindmarch, H.-X. Wei, Q.-H. Qin, Z.-C. Wen et al., Cotunneling enhancement of magnetoresistance in double magnetic tunnel junctions with embedded superparamagnetic NiFe nanoparticles, *Phys. Rev. B* **82**, 214415 (2010)

[96] X.-G. Zhang, Z. C. Wen, H. X. Wei and X. F. Han, Giant Coulomb blockade magnetoresistance in magnetic tunnel junctions with a granular layer, *Phys. Rev. B* **81**, 1 (2010) 7

[97] P. Seneor, A. Bernand-Mantel and F. Petroff, Nanospintronics: when spintronics meets single electron physics, *J. Phys. Condens. Matter* **19**, 165222 (2007) 8

[98] A. N. Pasupathy, R. C. Bialczak, J. Martinek, J. E. Grose, L. a. K. Donev et al., The Kondo effect in the presence of ferromagnetism., *Science* **306**, 86 (2004) 8

[99] H. Yang, S.-H. Yang and S. S. P. Parkin, Crossover from Kondo-assisted suppression to co-tunneling enhancement of tunneling magnetoresistance via ferromagnetic nanodots in MgO tunnel barriers., *Nano Lett.* **8**, 340 (2008)

[100] D. Ciudad, Z.-C. Wen, A. T. Hindmarch, E. Negusse, D. A. Arena et al., Competition between cotunneling, Kondo effect, and direct tunneling in discontinuous high-anisotropy magnetic tunnel junctions, *Phys. Rev. B* **85**, 214408 (2012) 8

[101] P. N. Hai, S. Ohya, M. Tanaka, S. E. Barnes and S. Maekawa, Electromotive force and huge magnetoresistance in magnetic tunnel junctions., *Nature* **458**, 489 (2009) 8

[102] C. Chen, W. Kuo, D. Chung, J. Shyu and C. Wu, Evidence for Suppression of Superconductivity by Spin Imbalance in Co-Al-Co Single-Electron Transistors, *Phys. Rev. Lett.* **88**, 047004 (2002) 8

[103] K. S. Ralls, R. a. Buhrman and R. C. Tiberio, Fabrication of thin-film metal nanobridges, *Appl. Phys. Lett.* **55**, 2459 (1989) 8

[104] R. Desmicht, G. Faini, V. Cros, a. Fert, F. Petroff et al., Point-contact electrodes to probe charging effects in individual ultrasmall cobalt clusters, *Appl. Phys. Lett.* **72**, 386 (1998) 8

[105] S. Guéron, M. Deshmukh, E. Myers and D. Ralph, Tunneling via Individual Electronic States in Ferromagnetic Nanoparticles, *Phys. Rev. Lett.* **83**, 4148 (1999) 8, 116

[106] M. Deshmukh, S. Kleff, S. Guéron, E. Bonet, A. Pasupathy et al., Magnetic Anisotropy Variations and Nonequilibrium Tunneling in a Cobalt Nanoparticle, *Phys. Rev. Lett.* **87**, 226801 (2001) 9

[107] J. Petta and D. Ralph, Studies of Spin-Orbit Scattering in Noble-Metal Nanoparticles Using Energy-Level Tunneling Spectroscopy, *Phys. Rev. Lett.* **87**, 266801 (2001)

[108] M. M. Deshmukh and D. C. Ralph, Using Single Quantum States as Spin Filters to Study Spin Polarization in Ferromagnets, *Phys. Rev. Lett.* **89**, 266803 (2002) 9

[109] K. Yakushiji, F. Ernult, H. Imamura, K. Yamane, S. Mitani et al., Enhanced spin accumulation and novel magnetotransport in nanoparticles., *Nat. Mater.* **4**, 57 (2005) 9, 83, 84, 116, 120

[110] S. Mitani, S. Takahashi, K. Takanashi, K. Yakushiji, S. Maekawa et al., Enhanced Magnetoresistance in Insulating Granular Systems: Evidence for Higher-Order Tunneling, *Phys. Rev. Lett.* **81**, 2799 (1998) 9

[111] K. Yakushiji, S. Mitani, K. Takanashi and H. Fujimori, Tunnel magnetoresistance oscillations in current perpendicular to plane geometry of CoAlO granular thin films, *J. Appl. Phys.* **91**, 7038 (2002)

[112] F. Ernult, K. Yamane, S. Mitani, K. Yakushiji, K. Takanashi et al., Spin-dependent single-electron-tunneling effects in epitaxial Fe nanoparticles, *Appl. Phys. Lett.* **84**, 3106 (2004) 9

[113] A. Bernand-Mantel, P. Seneor, K. Bouzehouane, S. Fusil, C. Deranlot et al., Anisotropic magneto-Coulomb effects and magnetic single-electron-transistor action in a single nanoparticle, *Nat. Phys.* **5**, 920 (2009) 9

[114] A. Bernand-Mantel, P. Seneor, K. Bouzehouane, S. Fusil, C. Deranlot et al., Anisotropic magneto-Coulomb effect versus spin accumulation in a ferromagnetic single-electron device, *Phys. Rev. B* **84**, 180413 (2011) 9

[115] A. Bernand-Mantel and P. Seneor, Evidence for spin injection in a single metallic nanoparticle: A step towards nanospintronics, *Appl. Phys. Lett.* **89**, 062502 (2006) 9

[116] S. J. van der Molen, N. Tombros and B. J. van Wees, Magneto-Coulomb effect in spin-valve devices, *Phys. Rev. B* **73**, 220406 (2006) 9

[117] C. Ciccarelli, L. P. Zarbo, A. C. Irvine, R. P. Campion, B. L. Gallagher et al., Spin gating electrical current, *Appl. Phys. Lett.* **101**, 122411 (2012) 9

[118] D. Davidović and M. Tinkham, Spectroscopy, interactions, and level splittings in Au nanoparticles, *Phys. Rev. Lett.* **83**, 1644 (1999) 9

[119] W. Jiang, F. T. Birk and D. Davidović, Microwave coupled electron tunneling measurement of Co nanoparticles, *Appl. Phys. Lett.* **99**, 032510 (2011)

[120] W. Jiang, P. Gartland and D. Davidović, Size-dependence of magneto-electronic coupling in Co nanoparticles, *J. Appl. Phys.* **113**, 223703 (2013) 9

[121] F. T. Birk and D. Davidović, Magnetoresistance in an aluminum nanoparticle with a single ferromagnetic contact, *Phys. Rev. B* **81**, 241402 (2010) 9

[122] J. Rousseau, R. Morel, L. Vila, A. Brenac, A. Marty et al., Sub-10 nm nano-gap device for single-cluster transport measurements, *Appl. Phys. Lett.* **104**, 073103 (2014) 9, 23

[123] R. Liu, S.-H. Yang, X. Jiang, T. Topuria, P. M. Rice et al., Tunneling magnetoresistance oscillations due to charging effects in MgO double barrier magnetic tunnel junctions, *Appl. Phys. Lett.* **100**, 012401 (2012) 9, 83, 93

[124] B. Koslowski, C. Dietrich, F. Weigl and P. Ziemann, Dynamic charging at room temperature of Au nanoparticles prepared by a micellar technique, *Phys. Rev. B* **75**, 085407 (2007) 9

[125] C. Pauly, M. Grob, M. Pezzotta, M. Pratzer and M. Morgenstern, Gundlach oscillations and Coulomb blockade of Co nanoislands on MgO/Mo(100) investigated by scanning tunneling spectroscopy at 300 K, *Phys. Rev. B* **81**, 125446 (2010) 9, 107

[126] H. Imamura, J. Chiba, S. Mitani, K. Takanashi, S. Takahashi et al., Coulomb staircase in STM current through granular films, *Phys. Rev. B* **61**, 46 (2000) 9

[127] K. Takanashi, S. Mitani, J. Chiba and H. Fujimori, Scanning tunneling microscopy investigation of single electron tunneling in Co-Al-O and Cu-Al-O granular films, *J. Appl. Phys.* **87**, 6331 (2000)

[128] S. Mitani, K. Takanashi, K. Yakushiji, J. Chiba and H. Fujimori, Study on spin dependent tunneling and Coulomb blockade in granular systems with restricted tunneling paths, *Mater. Sci. Eng. B* **84**, 120 (2001) 9

[129] H. Graf, J. Vancea and H. Hoffmann, Single-electron tunneling at room temperature in cobalt nanoparticles, *Appl. Phys. Lett.* **80**, 1264 (2002) 9

[130] W. Wulfhekel, A. Ernst, J. Henk, P. Bruno, J. Kirschner et al., Large spin effects in Coulomb blockade of Fe/MgO/Fe tunnel junctions, *Phys. Rev. B* **72**, 1 (2005) 10

[131] E. Schrödinger, An undulatory theory of the mechanics of atoms and molecules, *Phys. Rev.* **28**, 1049 (1926) 12

[132] R. Fowler and L. Nordheim, Electron emission in intense electric fields, *Proc. R. Soc. London* **119A**, 173 (1928) 12, 16

[133] L. Esaki, New phenomenon in narrow Germanium p-n junctions, *Phys. Rev.* **109**, 603 (1958) 12

[134] I. Giaever, Electron tunneling and superconductivity, *Rev. Mod. Phys.* **46**, 245 (1974) 12

[135] B. Josephson, The discovery of tunnelling supercurrents, *Rev. Mod. Phys.* **46**, 251 (1974) 12

[136] G. Binnig and H. Rohrer, Scanning tunneling microscopy-from birth to adolescence, *Rev. Mod. Phys.* **59**, 615 (1987) 12, 51

[137] D. Bohm, *Quantum Theory*, Prentice-Hall (1951) 13

[138] J. Simmons, Generalized formula for the electric tunnel effect between similar electrodes separated by a thin insulating film, *J. Appl. Phys.* **34**, 1793 (1963) 13, 105

[139] J. G. Simmons, Generalized Thermal J-V Characteristic for the Electric Tunnel Effect, *J. Appl. Phys.* **35**, 2655 (1964) 13

[140] E. Lundgren, G. Kresse, C. Klein, M. Borg, J. Andersen et al., Two-Dimensional Oxide on Pd(111), *Phys. Rev. Lett.* **88**, 246103 (2002) 15, 17

[141] T. Hartman, Tunneling through asymmetric barriers, *J. Appl. Phys.* **35**, 3283 (1964) 14

[142] W. F. Brinkman, Tunneling Conductance of Asymmetrical Barriers, *J. Appl. Phys.* **41**, 1915 (1970) 16

[143] C. Miller, Z.-P. Li, I. Schuller, R. Dave, J. Slaughter et al., Origin of the breakdown of Wentzel-Kramers-Brillouin-based tunneling models, *Phys. Rev. B* **74**, 212404 (2006) 16

[144] T. E. Stern, B. S. Gossling and R. H. Fowler, Further Studies in the Emission of Electrons from Cold Metals, *Proc. R. Soc. A Math. Phys. Eng. Sci.* **124**, 699 (1929) 16

[145] N. J. DiNardo, *Nanoscale Characterization of Surfaces and Interfaces*, VCH Verlagsgesellschaft mbH (1994) 16

[146] B. Das and J. Mahanty, Spatial distribution of tunnel current and application to scanning-tunneling microscopy: A semiclassical treatment, *Phys. Rev. B* **36**, 898 (1987) 16

[147] J. Bardeen, Tunnelling from a many-particle point of view, *Phys. Rev. Lett.* **6**, 57 (1961) 16

[148] J. Tersoff and D. Hamann, Theory and application for the scanning tunneling microscope, *Phys. Rev. Lett.* **50**, 1998 (1983) 17

[149] G. Binnig, K. Frank, H. Fuchs and N. Garcia, Tunneling spectroscopy and inverse photoemission: image and field states, *Phys. Rev. Lett.* **55**, 991 (1985) 17

[150] H. Lin, J. M. C. Rauba, K. S. Thygesen, K. W. Jacobsen, M. Y. Simmons et al., First-principles modelling of scanning tunneling microscopy using non-equilibrium Green's functions, *Front. Phys. China* **5**, 369 (2010) 17

[151] G. Seine, R. Coratger, A. Carladous, F. Ajustron, R. Pechou et al., Tip-to-surface distance variations vs voltage in scanning tunneling microscopy, *Phys. Rev. B* **60**, 11045 (1999) 17

[152] S. Maekawa, Spin dependent transport in magnetic nanostructures, *J. Magn. Magn. Mater.* **272-276**, e1459 (2002) 18

[153] E. Y. Tsymbal, O. N. Mryasov and P. R. LeClair, Spin-dependent tunnelling in magnetic tunnel junctions, *J. Phys. Condens. Matter* **15**, R109 (2003) 19

[154] T. Nagahama and J. Moodera, Magnetic tunnel junctions with magnesium oxide barriers, *J. Magn.* **11**, 170 (2006) 20

[155] Y. V. Nazarov and Y. M. Blanter, *Quantum transport*, Cambridge University Press (2009) 20

[156] C. Wasshuber, *About Single-Electron Devices and Circuits*, Ph.D. thesis, Technischen Universität Wien (1997) 20, 92

[157] J. Stöhr and H. C. Siegmann, *Magnetism: from fundamentals to nanoscale dynamics*, Springer (2006) 24, 28, 72, 116

[158] G. W. Qin, Y. P. Ren, N. Xiao, B. Yang, L. Zuo et al., Development of high density magnetic recording media for hard disk drives: materials science issues and challenges, *Int. Mater. Rev.* **54**, 157 (2009) 24

[159] D. Garanin and H. Kachkachi, Surface Contribution to the Anisotropy of Magnetic Nanoparticles, *Phys. Rev. Lett.* **90**, 065504 (2003) 24

[160] F. Bodker, S. Morup and S. Linderoth, Surface effects in metallic iron nanoparticles, *Phys. Rev. Lett.* **72**, 8 (1994) 24

[161] A. Kleibert, F. Bulut, R. K. Gebhardt, W. Rosellen, D. Sudfeld et al., Correlation of shape and magnetic anisotropy of supported mass-filtered Fe and FeCo alloy nanoparticles on W(110), *J. Phys. Condens. Matter* **20**, 445005 (2008) 24, 70

[162] C. Kittel, Theory of the structure of ferromagnetic domains in films and small particles, *Phys. Rev.* **70**, 965 (1946) 25

[163] S. Bedanta and W. Kleemann, Supermagnetism, *J. Phys. D. Appl. Phys.* **42**, 013001 (2009) 25

[164] W. F. Brown, Thermal fluctuations of a single-domain particle, *Phys. Rev.* **130**, 1677 (1963) 26

[165] M. Hansen and S. Mø rup, Estimation of blocking temperatures from ZFC/FC curves, *J. Magn. Magn. Mater.* **203**, 214 (1999) 26

[166] D.-X. Chen, A. Sanchez, E. Taboada, A. Roig, N. Sun et al., Size determination of superparamagnetic nanoparticles from magnetization curve, *J. Appl. Phys.* **105**, 083924 (2009) 26

[167] E. C. Stoner and E. P. Wohlfarth, A Mechanism of Magnetic Hysteresis in Heterogeneous Alloys, *Philos. Trans. R. Soc. A Math. Phys. Eng. Sci.* **240**, 599 (1948) 26, 27

[168] C. P. Bean and J. D. Livingston, Superparamagnetism, *J. Appl. Phys.* **30**, S120 (1959) 26, 75

[169] E. F. Kneller and F. E. Luborsky, Particle Size Dependence of Coercivity and Remanence of Single-Domain Particles, *J. Appl. Phys.* **34**, 656 (1963) 26

[170] E. C. Mendonça, C. B. R. Jesus, W. S. D. Folly, C. T. Meneses, J. G. S. Duque et al., Temperature dependence of coercive field of ZnFe2O4 nanoparticles, *J. Appl. Phys.* **111**, 053917 (2012) 26

[171] A. Barra and P. Debrunner, Superparamagnetic-like behavior in an octanuclear iron cluster, *Europhys. Lett.* **35**, 133 (1996) 28

[172] R. Nakajima, J. Stöhr and Y. U. Idzerda, Electron-yield saturation effects in L -edge x-ray magnetic circular dichroism spectra of Fe , Co , and Ni, *Phys. Rev. B* **59**, 6421 (1999) 28, 29

[173] C. Chen, Y. Idzerda, H. Lin and N. Smith, Experimental confirmation of the X-ray magnetic circular dichroism sum rules for iron and cobalt, *Phys. Rev. Lett.* **75**, 152 (1995) 29, 32, 62, 65

[174] J. Stöhr, Exploring the microscopic origin of magnetic anisotropies with X-ray magnetic circular dichroism (XMCD) spectroscopy, *J. Magn. Magn. Mater.* **200**, 470 (1999) 31

[175] P. Carra, B. Thole, M. Altarelli and X. Wang, X-ray circular dichroism and local magnetic fields, *Phys. Rev. Lett.* **70**, 694 (1993) 30

[176] B. Thole, P. Carra, F. Sette and G. V. D. Laan, X-ray circular dichroism as a probe of orbital magnetization, *Phys. Rev. Lett.* **68**, 1943 (1992) 32

[177] F. Penning, Die glimmentladung bei niedrigem druck zwischen koaxialen zylindern in einem axialen magnetfeld, *Physica* **3**, 873 (1936) 35

[178] G. Bräuer, B. Szyszka, M. Vergöhl and R. Bandorf, Magnetron sputtering - Milestones of 30 years, *Vacuum* **84**, 1354 (2010) 35

[179] K. Ellmer, Magnetron sputtering of transparent conductive zinc oxide: relation between the sputtering parameters and the electronic properties, *J. Phys. D. Appl. Phys.* **33**, R17 (2000) 36

[180] A. T. Hindmarch, V. Harnchana, D. Ciudad, E. Negusse, D. A. Arena et al., Magnetostructural influences of thin Mg insert layers in crystalline CoFe(B)/MgO/CoFe(B) magnetic tunnel junctions, *Appl. Phys. Lett.* **97**, 252502 (2010) 37

[181] S. H. Baker, S. C. Thornton, A. M. Keen, T. I. Preston, C. Norris et al., The construction of a gas aggregation source for the preparation of mass-selected ultrasmall metal particles, *Rev. Sci. Instrum.* **68**, 1853 (1997) 38, 40

[182] E. Quesnel, E. Pauliac-Vaujour and V. Muffato, Modeling metallic nanoparticle synthesis in a magnetron-based nanocluster source by gas condensation of a sputtered vapor, *J. Appl. Phys.* **107**, 054309 (2010) 38

[183] J. Frenkel, *Kinetic theory of liquids*, Oxford University Press (1946) 38

[184] K. J. Dempsey, *Magnetic and Electronic Transport Properties of Magnetic Nanoparticles*, Ph.D. thesis, University of Leeds (2011) 39

[185] Quadrupole mass filter QMF200 reference manual, Technical report 40

[186] H. Haberland, Z. Insepov and M. Moseler, Molecular-dynamics simulation of thin-film growth by energetic cluster impact, *Phys. Rev. B* **51**, 61 (1995) 41, 102

[187] J. Bansmann, S. Baker, C. Binns, J. Blackman, J. Bucher et al., Magnetic and structural properties of isolated and assembled clusters, *Surf. Sci. Rep.* **56**, 189 (2005) 41, 58, 68, 75

[188] N. A. Porter, *Magnetoresistance in n-type Silicon*, Ph.D. thesis, University of Leeds (2010) 43

[189] J. Als-Nielsen and D. McMorrow, *Elements of modern x-ray physics*, Wiley (2001) 43

[190] P. Champness, *Electron diffraction in the transmission electron microscope*, Bios Scientific (2001) 43, 44

[191] S. Foner, Versatile and Sensitive Vibrating-Sample Magnetometer*, *Rev. Sci. Instrum.* **30**, 548 (1959) 48

[192] MPMS SQUID-VSM reference manual, Technical report 49

[193] J. Vickerman and I. Gilmore, *Surface analysis: the principal techniques*, Wiley, 2nd edition (2009) 49, 51, 54

[194] G. Binnig, C. Quate and C. Gerber, Atomic force microscope, *Phys. Rev. Lett.* **56**, 930 (1986) 49

[195] N. Jalili and K. Laxminarayana, A review of atomic force microscopy imaging systems: application to molecular metrology and biological sciences, *Mechatronics* **14**, 907 (2004) 49

[196] Y. Seo and W. Jhe, Atomic force microscopy and spectroscopy, *Reports Prog. Phys.* **71**, 016101 (2008) 49

[197] R. García and R. Pérez, Dynamic atomic force microscopy methods, *Surf. Sci. Rep.* **47**, 197 (2002) 50

[198] G. Binnig, H. Rohrer, C. Gerber and E. Weibel, Surface studies by scanning tunneling microscopy, *Phys. Rev. Lett.* **49**, 57 (1982) 51

[199] S. Ernst, S. Wirth, M. Rams, V. Dolocan and F. Steglich, Tip preparation for usage in an ultra-low temperature UHV scanning tunneling microscope, *Sci. Technol. Adv. Mater.* **8**, 347 (2007) 53, 54

[200] H. Jansen and A. Freeman, Total-energy full-potential linearized augmented-plane-wave method for bulk solids: Electronic and structural properties of tungsten, *Phys. Rev. B* **30**, 561 (1984) 54

[201] H. Ness and F. Gautier, The electronic structure and stability of transition metal nanotips. I, *J. Phys. Condens. Matter* **7**, 6625 (1995) 54

[202] S. Kerfriden, A. Nahlé, S. Campbell, F. Walsh and J. Smith, The electrochemical etching of tungsten STM tips, *Electrochim. Acta* **43**, 1939 (1998) 54

[203] C. S. Allen, *Structural characterisation, fabrication and electronic properties of carbon nanotube devices*, Ph.D. thesis, University of Leeds (2009) 54

[204] N. Cabrera and N. Mott, Theory of the oxidation of metals, *Reports Prog. Phys.* pp. 163–184 (1949) 58

[205] M. Seah and W. Dench, Quantitative electron spectroscopy of surfaces: a standard data base for electron inelastic mean free paths in solids, *Surf. interface Anal.* **1**, 2 (1979) 59

[206] A. Kleibert, J. Passig, K.-H. Meiwes-Broer, M. Getzlaff and J. Bansmann, Structure and magnetic moments of mass-filtered deposited nanoparticles, *J. Appl. Phys.* **101**, 114318 (2007) 59

[207] N. W. Ashcroft and N. D. Mermin, *Solid state physics*, Brooks/Cole (1976) 62

[208] D. Nečas and P. Klapetek, Gwyddion: an open-source software for SPM data analysis, *Cent. Eur. J. Phys.* **10**, 181 (2012) 63

[209] H. Ebert and M. Battocletti, Spin and orbital polarized relativistic multiple scattering theory-With applications to Fe, Co, Ni and FexCo1-x, *Solid State Commun.* **98**, 785 (1996) 65

[210] J. Lau, A. Föhlisch, M. Martins, R. Nietubyc, M. Reif et al., Spin and orbital magnetic moments of deposited small iron clusters studied by x-ray magnetic circular dichroism spectroscopy, *New J. Phys.* **4**, 98.1 (2002) 65, 67

[211] S. Baker, C. Binns, K. Edmonds, M. Maher, S. Thornton et al., Enhancements in magnetic moments of exposed and Co-coated Fe nanoclusters as a function of cluster size, *J. Magn. Magn. Mater.* **247**, 19 (2002)

[212] J. Bansmann, M. Getzlaff, A. Kleibert, F. Bulut, R. K. Gebhardt et al., Mass-filtered cobalt clusters in contact with epitaxially ordered metal surfaces, *Appl. Phys. A* **82**, 73 (2005)

[213] A. Kleibert, W. Rosellen, M. Getzlaff and J. Bansmann, Structure, morphology, and magnetic properties of Fe nanoparticles deposited onto single-crystalline surfaces., *Beilstein J. Nanotechnol.* **2**, 47 (2011) 65, 67

[214] R. Guirado-López, J. Dorantes-Dávila and G. Pastor, Orbital Magnetism in Transition-Metal Clusters: From Hundâ€™s Rules to Bulk Quenching, *Phys. Rev. Lett.* **90**, 226402 (2003) 67

[215] A. Kleibert, K.-H. Meiwes-Broer and J. Bansmann, Size-dependent magnetic spin and orbital moments of Fe nanoparticles deposited onto Co/W(110), *Phys. Rev. B* **79**, 125423 (2009) 68, 100

[216] K. Edmonds, C. Binns, S. Baker, S. Thornton, C. Norris et al., Doubling of the orbital magnetic moment in nanoscale Fe clusters, *Phys. Rev. B* **60**, 472 (1999) 68

[217] H. Klein and E. Kneller, Variation of magnetocrystalline anisotropy of iron with field and temperature, *Phys. Rev.* **144**, 372 (1966) 70, 75, 78

[218] C. Binns, M. Maher, Q. Pankhurst, D. Kechrakos and K. Trohidou, Magnetic behavior of nanostructured films assembled from preformed Fe clusters embedded in Ag, *Phys. Rev. B* **66**, 184413 (2002) 72

[219] A. Rondinone, Superparamagnetic relaxation and magnetic anisotropy energy distribution in CoFe2O4 spinel ferrite nanocrystallites, *J. Phys. Chem. B* **103**, 6876 (1999) 72

[220] M. Bhatia, Magnetic moments in the Fe-Co system, *Curr. Sci.* **99**, 785 (2010) 75, 100

[221] W. Nunes, W. Folly, J. Sinnecker and M. Novak, Temperature dependence of the coercive field in single-domain particle systems, *Phys. Rev. B* **70**, 014419 (2004) 75

[222] A. Tewari and A. Gokhale, Nearest-neighbor distributions in thin films, sheets, and plates, *Acta Mater.* **54**, 1957 (2006) 78

[223] K. Fauth, G. E. Ballentine, C. Praetorius, A. Kleibert, N. Wilken et al., Magnetic properties of Fe nanoclusters on Cu(111) studied with X-ray magnetic circular dichroism, *Phys. Status Solidi* **247**, 1170 (2010) 80

[224] A. Ebbing, O. Hellwig, L. Agudo, G. Eggeler and O. Petracic, Tuning the magnetic properties of Co nanoparticles by Pt capping, *Phys. Rev. B* **84**, 012405 (2011) 80

[225] R. C. Temple and C. H. Marrows, Single-electron spin interplay for characterization of magnetic double tunnel junctions, *Phys. Rev. B* **88**, 184415 (2013) 83, 115, 120

[226] J. Barnaś and A. Fert, Effects of spin accumulation on single-electron tunneling in a double ferromagnetic microjunction, *Europhys. Lett.* **44**, 85 (1998) 83, 87, 93

[227] P. N. Hai, S. Ohya and M. Tanaka, Long spin-relaxation time in a single metal nanoparticle., *Nat. Nanotechnol.* **5**, 593 (2010) 83, 116

[228] A. Brataas, Y. Nazarov, J. Inoue and G. Bauer, Spin accumulation in small ferromagnetic double-barrier junctions, *Phys. Rev. B* **59**, 93 (1999) 83, 92

[229] A. Brataas, Y. Nazarov, J. Inoue and G. Bauer, Non-equilibrium spin accumulation in ferromagnetic single-electron transistors, *Eur. Phys. J. B* **9**, 421 (1999) 83

[230] W. Kuo and C. Chen, Gate-controlled spin polarized current in ferromagnetic single electron transistors, *Phys. Rev. B* **65**, 104427 (2002) 83

[231] J. Martinek, J. Barnaś and A. Fert, Transport in magnetic nanostructures in the presence of Coulomb interaction, *J. Appl. Phys.* **93**, 8265 (2003) 83

[232] V. Estévez and E. Bascones, Robustness of the magnetoresistance of nanoparticle arrays, *Phys. Rev. B* **84**, 075441 (2011) 83

[233] P. van Son, H. van Kempen and P. Wyder, Boundary resistance of the ferromagnetic-nonferromagnetic metal interface, *Phys. Rev. Lett.* **58**, 2271 (1987) 94

[234] R. Meservey and P. Tedrow, Spin-polarized electron tunneling, *Phys. Rep.* **238**, 173 (1994) 96

[235] V. Ray, R. Subramanian, P. Bhadrachalam, L.-C. Ma, C.-U. Kim et al., CMOS-compatible fabrication of room-temperature single-electron devices., *Nat. Nanotechnol.* **3**, 603 (2008) 96

[236] T. Vystavel, G. Palasantzas, S. a. Koch and J. T. M. De Hosson, Nanosized iron clusters investigated with in situ transmission electron microscopy, *Appl. Phys. Lett.* **82**, 197 (2003) 100

[237] N. V. Brilliantov and T. Pöschel, *Kinetic theory of granular gases*, Oxford University Press (2010) 102

[238] M. Mizuguchi, Y. Suzuki, T. Nagahama and S. Yuasa, In situ scanning tunneling microscopy observations of polycrystalline MgO(001) tunneling barriers grown on amorphous CoFeB electrode, *Appl. Phys. Lett.* **91**, 012507 (2007) 102, 103

[239] Y. Kuk, Scanning tunneling spectroscopy of metal surfaces, *J. Vac. Sci. Technol. A Vacuum, Surfaces, Film.* **8**, 289 (1990) 103

[240] M. Tobita and S. Ho, Electronic Structure Calculation of MgO (001) Surface with Aggregated Oxygen Vacancies, *J. Chem. Theory Comput.* **4**, 1057 (2008) 105

[241] Y. Lu, J. C. Le Breton, P. Turban, B. Lépine, P. Schieffer et al., Band structure of the epitaxial Fe/MgO/GaAs(001) tunnel junction studied by x-ray and ultraviolet photoelectron spectroscopies, *Appl. Phys. Lett.* **89**, 152106 (2006) 105

[242] I.-C. Ho, Y. Xu and J. D. Mackenzie, Electrical and optical properties of MgO thin film prepared by sol-gel technique, *J. Sol-Gel Sci. Technol.* **9**, 295 (1997) 105

[243] W. Wulfhekel, M. Klaua, D. Ullmann, F. Zavaliche, J. Kirschner et al., Single-crystal magnetotunnel junctions, *Appl. Phys. Lett.* **78**, 509 (2001) 105

[244] S. Schintke, S. Messerli, M. Pivetta, F. Patthey, L. Libioulle et al., Insulator at the Ultrathin Limit: MgO on Ag(001), *Phys. Rev. Lett.* **87**, 276801 (2001) 107

[245] M. Klaua, D. Ullmann and J. Barthel, Growth, structure, electronic, and magnetic properties of MgO/Fe (001) bilayers and Fe/MgO/Fe (001) trilayers, *Phys. Rev. B* **64**, 134411 (2001) 107

[246] O. Raichev, Coulomb blockade of field emission from nanoscale conductors, *Phys. Rev. B* **73**, 195328 (2006) 110, 117

[247] W. M. Tsang, V. Stolojan, B. J. Sealy, S. P. Wong and S. R. P. Silva, Electron field emission properties of Co quantum dots in SiO2 matrix synthesised by ion implantation., *Ultramicroscopy* **107**, 819 (2007) 110

[248] C. Kim, H. S. Kim, H. Qin and R. H. Blick, Coulomb-controlled single electron field emission via a freely suspended metallic island., *Nano Lett.* **10**, 615 (2010)

[249] A. Pascale-Hamri, S. Perisanu, A. Derouet, C. Journet, P. Vincent et al., Ultrashort Single-Wall Carbon Nanotubes Reveal Field-Emission Coulomb Blockade and Highest Electron-Source Brightness, *Phys. Rev. Lett.* **112**, 126805 (2014) 110

[250] J. D. Teresa, A. Barthelemy and A. Fert, Role of metal-oxide interface in determining the spin polarization of magnetic tunnel junctions, *Science (80-. ).* **286**, 507 (1999) 115

[251] M. Aeschlimann, R. Burgermeister, S. Pawlik, M. Bauer, D. Oberli et al., Spin-dependent electron dynamics investigated by means of time- and spin-resolved photoemission, *J. Electron Spectros. Relat. Phenomena* **88-91**, 179 (1998) 116

[252] T. Fujisawa, D. Austing and Y. Tokura, Allowed and forbidden transitions in artificial hydrogen and helium atoms, *Nature* **419**, 278 (2002) 121

[253] J. Elzerman and R. Hanson, Single-shot read-out of an individual electron spin in a quantum dot, *Nature* **430**, 431 (2004) 121